HYDROGEN TRANSPORT IN THIN FILMS:

Mg-MgH$_2$ AND Ti-TiH$_2$ SYSTEMS

Von der Fakultät Chemie der Universität Stuttgart

zur Erlangung der Würde eines Doktors

der Naturwissenschaften (Dr. rer. nat.)

genehmigte Abhandlung

Vorgelegt von

Efi HADJIXENOPHONTOS

aus Zypern

Prüfungsvorsitzender: Prof. Dr. Thomas Schleid

Hauptberichter: Prof. Dr. Dr. Guido Schmitz

Mitberichter: Prof. Dr. Joachim Bill

Tag der mündlichen Prüfung: 23. Juli 2018

Institut für Materialwissenschaft (IMW) der Universität Stuttgart

2018
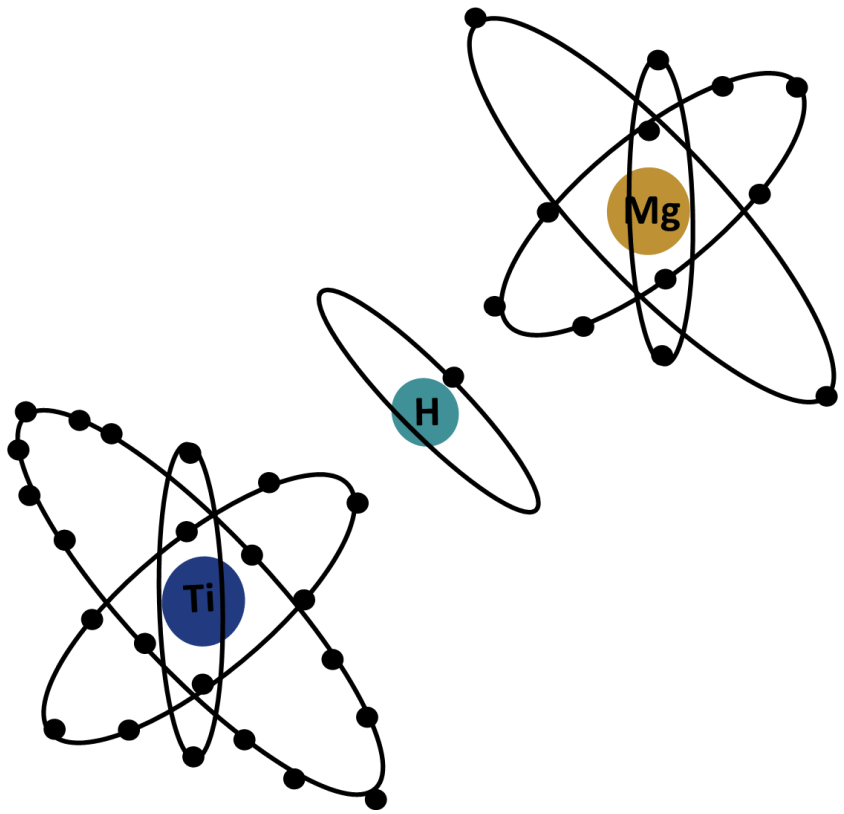
Abstract

Hydrogen storage has become progressively important due to increasing energy demand. Magnesium (Mg/MgH_2) is one of the most promising elements of hydrogen uptake, however, the slow kinetics and need for high temperatures during dehydrogenation make this material challenging for mobile applications. Meanwhile, Titanium ($Ti/TiH_2/TiO_2$) draws attention due to its catalytic effect in hydrogenation of other metals with higher capacities. A comprehensive way to quantitatively characterize the kinetics of hydride formation in both systems (Mg and Ti) is shown here. A technique allowing a large range of pressures and temperatures (room temperature to 300 °C and from 0.05 bar up to 100 bar) is developed successfully. Thin films (50-1000 nm), deposited by ion beam sputtering (PVD), are used because of their smooth surface and defined structure. In order to study hydrogen transport precisely, X-ray diffraction (XRD), electron microscopy (SEM/FIB/TEM) and electric resistance measurements are used. In the case of Mg, while a Pd coating is used as catalyst, the hydride is formed from the surface towards the substrate and transformation in the morphology is observed. Parabolic law is followed and the diffusion coefficient of hydrogen in MgH_2 is obtained at room temperature ($2.67 \cdot 10^{-17}$ cm^2/s). Additionally, a model is created to fit the experimental change in resistance during hydrogen loading and shows the changes in the behavior of thicker layers. The interface between Pd/Mg is discussed, since Mg_5Pd_2 and Mg_6Pd are formed at high temperatures and are most dominant over dehydrogenation. However, at room temperature, this interface appears to be more stable. The activation energy of hydrogenation is calculated experimentally from an Arrhenius plot to be equal to $E_a = 22.6 \pm 2.0$ kJ/mol and the pre-factor $D_0 = 3904$ cm^2/s. Additional attention is given to magnesium hydride as an anode electrode in Li-ion batteries. TEM investigations of thin film electrodes demonstrate the complete lithiation of the material however, with drastic volume changes, leading to bad reversibility. In Ti the thin oxide layer naturally formed on the surface, appears to play a dominant role in the kinetics of hydrogen transport leading to a linear kinetics. A pressure dependency is observed, while an experimental evaluation of the permeation coefficient in the oxide is also discussed. Important information on the hydrogen transport is obtained in both systems, giving an input for further improvements of such hydrides.

Kurzfassung

Die Wasserstoffspeicherung ist aufgrund des steigenden Energiebedarfs zunehmend wichtig geworden. Magnesium (Mg / MgH$_2$) ist eines der vielversprechendsten Elemente der Wasserstoffaufnahme, die langsame Kinetik und der Bedarf an hohen Temperaturen während der Dehydrierung machen dieses Material jedoch zu einer Herausforderung für mobile Anwendungen. Auch macht Titan (Ti / TiH$_2$ / TiO$_2$) aufgrund seiner katalytischen Wirkung bei der Hydrierung anderer Metalle mit höheren Kapazitäten auf sich aufmerksam. Ein umfassender Weg zur quantitativen Charakterisierung der Kinetik der Hydridbildung in beiden Systemen (Mg und Ti) wird hier gezeigt. Eine Technik, die einen großen Bereich von Drücken und Temperaturen (R.T. bis 300 ° C und von 0,05 bar bis 100 bar) ermöglicht, wurde erfolgreich entwickelt. Dünne Schichten (50-1000 nm), abgeschieden durch Ionenstrahl-Sputtern (PVD), werden wegen ihrer glatten Oberfläche und definierten Struktur verwendet. Um den Wasserstofftransport genau zu untersuchen, werden Röntgenbeugung (XRD), Elektronenmikroskopie (SEM / FIB / TEM) und elektrische Widerstandsmessungen verwendet. Im Fall von Mg wird, wenn Pd als Katalysator an der Oberfläche verwendet wird, das Hydrid von der Oberfläche in Richtung auf das Substrat gebildet. Gleichzeitig wird eine Veränderung der Morphologie beobachtet. Ein parabolisches Zeitgesetz wird befolgt und der Diffusionskoeffizient in MgH$_2$ wird experimentell bei R.T. (2.67 $\cdot$ 10^{-17} cm^2/s) bestimmt. Darüber hinaus wurde erfolgreich ein Modell erstellt, um die experimentelle Widerstandsänderung während der Wasserstoffbeladung zu berücksichtigen und die Veränderungen im Verhalten dickerer Schichten zu zeigen. Die Grenzfläche zwischen Pd / Mg wird diskutiert, da Mg$_5$Pd$_2$ und Mg$_6$Pd bei hohen Temperaturen gebildet werden und die Dehydrierung kontrollieren. Bei R.T. scheint diese Grenzfläche jedoch stabil zu sein. Die Aktivierungsenergie der Hydrierung wird experimentell aus einem Arrhenius-Diagramm berechnet, zu E$_a$ = 22 ± 2 kJ/mol bei einem Vorfaktor von D$_0$ = 3904 cm2/s. Zusätzliches Augenmerk wird auf Magnesiumhydrid als Anodenelektrode in Li-Ionen-Batterien gelegt. TEM-Untersuchungen von Dünnschichtelektroden zeigen die vollständige Lithiierung des Materials, jedoch mit drastischen Volumenänderungen, die im Laufe der Zeit zu einer schlechten Reversibilität führen. In Ti scheint die natürlich gebildete dünne Oberflächenoxidschicht eine dominante Rolle in der Kinetik des Wasserstofftransports zu spielen, was zu einer linearer Kinetik der Hydridbildung führt. Die Druckabhängigkeit wird beobachtet und der experimentelle Bewertung des Permeationskoeffizient im Oxid ebenfalls quantifiziert. Wichtige Information über den Wasserstofftransport in beiden Systemen wird so erhalten, was wesentlichen Input für weitere Verbesserungen solcher Hydride liefert.

TABLE OF CONTENTS

1 INTRODUCTION

Imagining a world without connection to energy seems impossible in our highly technological society. Switching on the light, opening our fridge, switching on our phones, driving to work, are actions taken for granted, but they represent a stage in the chain of a long technological process. Energy is the motor of our modern, industrial society and as such, a foundation for its progress. Since the industrial revolution, energy consumption has increased by a factor of 80, while the world population has grown only 6 times [Je03]. In today's world, renewable energies and replacement of fossil fuels are of great importance, not only to industry, but to human nature as well.

Hydrogen seems to play a big role in this evolution. As the lightest and most abundant element in the universe, it has been a great focus of research since its discovery. As an alternative fuel, standing in its ability to power fuel cells with zero-emission, industries and governments turn their focus to this important element. The dream of a clean environment, sustainable energy and greener transportation seems to burn brightly in the promise of hydrogen-based materials.

Fire was civilization's first great energy invention and wood was the main fuel for a long time, until the Chinese first burnt coal for heating and cooking. Later, Europeans built wheels in rivers and streams to harness water energy. Persians built the first windmills in 1000 A.D., which reached a more efficient form in the hands of Dutch engineers towards the 16th century. Using only green energy, water and wind, was for centuries a reality.

While Roman engineers used pumps in mines centuries ago, in the early 17th century, the progress of pumps made coal mining more intensive since water could be removed from the mines more easily. With Thomas Newcomen's invention of the steam engine in 1712, the British discovered how coal could be burned in order to power heat engines and has produced major fuel this way in their industry for the last centuries. It was clear that burning coal provided significantly larger amounts of power, than what muscle, water or wind could offer. Therefore, coal began to replace other fuels and became the main energy source of civilization, without considering at the time, the negative effects it might have on nature.

It was much later, in 1776 that hydrogen was first identified as a separate element by the British scientist Henry Cavendish. A few years later, in 1800, Alessandro Volta invented the first electrical battery and discovered methane. In the same year, another important invention, the process of electrolysis was discovered, when English scientists, William Nicholson and Sir Anthony Carlisle, applied an electric current to water and produced hydrogen and oxygen gases. This discovery was an important historical step in the development of hydrogen as an energy fuel. In 1838, William Robert Grove developed the first "gas battery", while using a platinum (Pt) electrode immersed in nitric acid and a zinc electrode in

zinc sulfate generated electricity in this way. Later in 1889, Charles Langer and Ludwig Mond developed Grove's invention and built the first fuel cell device using air and industrial coal gas, a device they named "fuel cell". At the same time, while hydrogen technologies were evolving, in 1850 the first oil well was drilled in Titusville in Florida and the industrial evolution had just started growing.

Hydrogen had become a fascinating element, promising only more to society. A big event however, gave a shock to the hydrogen world. In 1937 the Hindenburg Zeppelin, LZ 129, was destroyed by fire and crashed upon landing in New Jersey. This event alarmed the population about the use of hydrogen as gas. The unfortunate mystery crash was only solved in 1997, when studies showed that the explosion was not due to the hydrogen gas. The silver colored canvas of the exterior of the airship had been treated with solid rocket fuel, which was then ignited due to weather related static electric discharge. Meanwhile, the discovery of the Ghawar oil field in 1948, gave rise to the world's largest petroleum deposit in Saudi Arabia, producing 5 million barrels of oil daily. The same year, the first nuclear reactor generated electricity for the first time in Oak Ridge Tennessee (USA). Today, more than 160 nuclear reactors have a capacity of over 1.000 MW, and many other provide electricity worldwide. The fear of using hydrogen as a fuel source partially exists in our culture to this day.

In the competition of renewable energies versus oil discoveries over the years, NASA played an important role in the hydrogen world with the use in their space program, mostly for rocket propulsion and fuel cells. In 1959, engineer Francis T. Bacon was the most interesting figure to innovate fuel cell technology. While early designers were using expensive Pt electrodes and corrosive sulfuric acid as electrolytes, he improved the system with cheaper, Ni electrodes and less corrosive alkaline electrolytes. Hydrogen fuel cells, based upon his design (called "Bacon cells"), were developed by General Electric (GE) and were the first cells used to generate on-board electricity, heat and water for astronauts aboard the famous Apollo spacecrafts. Though his technology found no use outside of space applications, because of its requirement for pure hydrogen and oxygen, its success was a technological example and inspiration to research on many other fuel cell operating systems [Ei09].

Car manufacturers raced to manufacture products that took advantage of the technological advancements. General Motors was the first to release an Electric Car in 1966 available to public. Other major car manufacturers also started production of electric vehicles using hydrogen and today, more and more people accept the new technology as an alternative to current fuels. The first hydrogen fueling stations in Europe opened in Germany in 1999 and today many countries have hydrogen initiatives in place for a long-term vision of hydrogen fuel societies. Billions are devoted to hydrogen research and vehicle demonstration projects. By the end of 2017, there were 56 hydrogen refueling stations in Germany (45 for public access) [fu]. Hydrogen energy and fuel cell power promises a clean, abundant, reliable and affordable replacement for fossil fuels.

The fact that hydrogen can solute in metals has been well-studied over centuries. A first appearance occurred in 1808, when Gay-Lussac and Thenard obtained metal hydrides using purely chemical methods. As with many other inventions, metal hydrides first started as curiosity tests in a laboratory and took some time before becoming technically important. As one of the carbon-free renewable energy carriers, hydrogen can be fabricated (via electrolysis), stored and consumed in a recyclable process. Storing hydrogen however, is one of the challenges industry faces in our days, since demand and reliability is important, but safety is also a big issue.

Hydrides are compounds were hydrogen is bonded to another element. Having the entire periodic table of elements available, finding the best element combination remains a challenge. Some complex hydrides, such as potassium borohydride are better used as reducing agents. Other metals, such as Pd, Ni and other transition metals are mainly of interest due to their catalytic effect, since they have high affinity to hydrogen [Fa62]. Hydrides of alkali metals show no electric conductivity, whereas other borohydrides and closoboranes are considered good ionic conductors and suitable for solid-state electrolyte applications in Li and Na ion batteries.

A well-known and well-studied hydride, not only for hydrogen storage applications, but also for electrochemical storage, is Magnesium hydride (MgH_2). Mg is a remarkable material, essential for ocean life, terrestrial plants and humans. As the third most abundant ion in salt water, it's necessary for coral reef formation in the oceans. Without Mg, chlorophyll cannot capture the sun's energy for photosynthesis in plants. Animals, from humans to dogs need magnesium for healthy bones, muscles and livers. Today, Mg can also be an indispensable element for storing energy.

Magnesium hydride is a cost-efficient material, which has been studied intensively since 1959. Along with its low cost, the hydride has a high gravimetric and volumetric hydrogen density of 7.6 wt% (110 kg/m^3) and 110 g H/l respectively [Cr16a]. This, in principle, reversible storage system, MgH_2 – Mg, however, has some drawbacks. Hydrogen (H) acts as an ion (H-) in this so-called, ionic hydrides and this makes the stable compound able to release hydrogen at 1 bar of H_2 pressure at about 300 °C. This high stability of the hydride and the consequent necessity of high temperatures for releasing hydrogen, make it challenging for industrial large-scale applications, which is why research is still ongoing. Furthermore, despite the great range of available characterization tools in our days, broad scatter in diffusion coefficients appear, since studying bulk materials or thin films, different temperatures or different pressures appears to need a challenging adjustment.

Even though challenging and still under intense investigations, some companies believe in the material and have been supplying solutions of energy storage based on magnesium since 2008. Such companies are, for example, McPhy and Hydrexia. They do not use Mg in it's pure form, but in an alloy, mostly with transition metals (TM). This improves the material in an acceptable way for some applications, mostly stationary. In general, mechanical modifications by ball milling [Fl13], [Hu13] or severe plastic

deformation [Cr16a], alloying [ZFS15] and nanoconfinement [Zl13] are some of the techniques studied today in order to modify the sorption properties of Mg.

Likewise, research has shown that transition metals can improve the kinetics properties [Do06] as well as protect MgH_2 from surface oxidation. Relevant transition metals are titanium (Ti) [Ei11], [Ju14], [Ve08], [Zh15], [Sh00] and its oxide (TiO_2) [CGW10] and palladium (Pd) [GKC13], which are studied also during this work. Titanium is discussed intensively today as a catalyst to accelerate the hydrogenation kinetics of hydrogen storage materials. It is, however, known that H absorption in Ti decisively depends on the surface conditions (presence or absence of the natural surface oxide). Considerable scattering among the experimental data available in literature shows the uncertainty and lack of information in this field. Therefore, focus is given on understanding the hydrogenation of Ti and the impact of the oxide on hydrogen diffusion in Ti and TiH_2 in this work.

In order to improve these systems, it is important to understand the reason for the slow kinetics of hydride formation. Thin films provide a useful tool to analyze essential mechanisms. With a smooth surface and a well-defined geometry, one can quantify the atomic transport through the layers more easily than in powders. Thin films also enable us to monitor the growth process of the hydride inside the metal and to see how hydrogen affects the structure of the layer and the phase transformation.

1.1 Aim of this thesis

The goal of this work is to study the hydrogen transport and phase transformation in the two systems separately as demonstrated in Figure 1-1: $Mg - MgH_2$ and $Ti - TiH_2$ in thin films. For the first time, investigations over a wide range of temperatures (room temperature – 300 °C) and pressures (0.001 – 100 bar), should provide information for the kinetics of hydride formation in both systems.

By observing the formation process of the hydrides, with the help of X-ray diffraction (XRD), resistance measurements, cross sections by focused ion beam (FIB), scanning electron microscopy (SEM), transmission electron microscopy (TEM) as well as electron diffraction, it is possible to derive relevant quantitative transport coefficients for both systems. Due to the extensive temperature range, an Arrhenius plot could be obtained in the case of Mg and the activation energy for the MgH_2 is experimentally determined. These results are of importance, since this is the first time that experiments could be carried out in such a temperature precision and range using a single sample geometry. Quantified data will be presented revealing the diffusion coefficients of hydrogen into the hydrides at different temperatures. Furthermore, the permeation coefficient, in the case of TiO_2 will be measured, while the effect of increasing pressure in the system is also studied. Even though rutile-TiO_2 is a well-studied material, the hydrogen permeation coefficient has never been experimentally obtained.

Additional interest is given in magnesium hydride (MgH_2) as an anode electrode material in Li-ion batteries. Despite its high theoretical capacity, a drastic decrease of 70% capacity loss is observed over

the first cycle [Be17]. During this work, investigations of the microstructure during the first lithiation provide information on the stability and changes of the material over cycling.

Both systems are of considerable interest, contributing to the understanding of key issues and open questions related to the technological application of hydrogen storage materials.
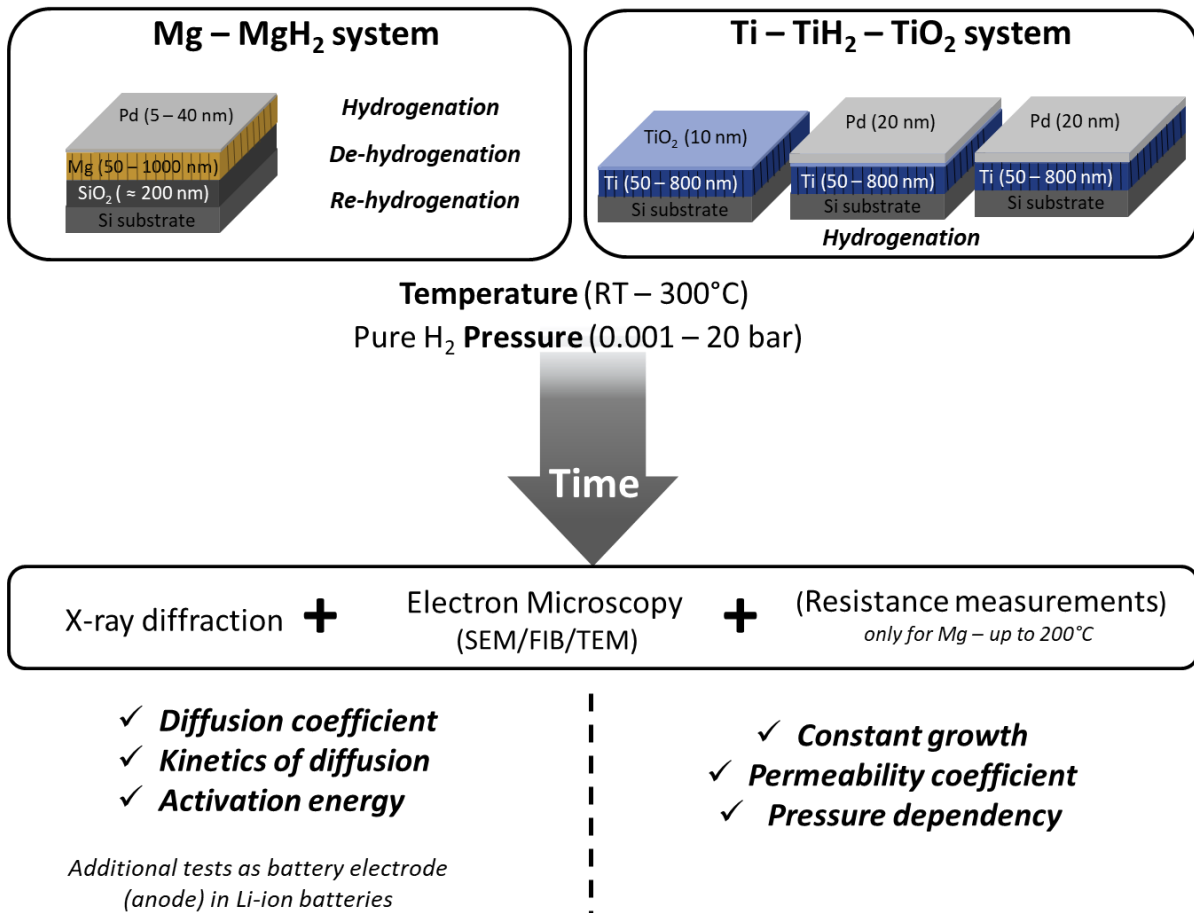

Figure 1-1: Overview of the samples investigated in this work. Both systems, Mg and Ti are studied in a large range of temperatures and pressures with X-ray diffraction and electron microscopy. Additional resistance measurements are carried out for the Mg system as well as electrochemical tests.

2 FUNDAMENTALS

This chapter focuses on the fundamental details of solid-state hydrogen storage. The thermodynamics of hydride formation and the different categories of hydrides will be discussed. Further attention is devoted to the kinetics of diffusion of hydrogen inside a metal (linear and parabolic regime), as it will be useful for the later calculations. A brief bibliography information on each system (Mg-MgH$_2$ and Ti-TiH$_2$-TiO$_2$) is also given, providing an overview of the already published diffusion coefficients of the two systems studied during this work.

2.1 Solid state hydrogen storage

Hydrogen is named after the Greek words: «ὕδωρ» and «γεννῶ», which means "water-born" by the French chemist Antoine Lavoisier in 1788, 10 years after its discovery as an element. After the Germans Kirchhoff and Bunsen demonstrated the presence of hydrogen in the spectra of the sun in 1861, it became evident that hydrogen was the most abundant element in our solar system. Hydrogen produced on Earth is, however, able to escape the gravitational field. This explains the very low concentration of hydrogen gas in our atmosphere. Most hydrogen is found, mainly chemically bonded in water, molecular forms and organic compounds.

Storing hydrogen is one of the challenges industries face today, since immediate demand, consistency and safety are important. Storing hydrogen in its molecular gas form, one would think is the easiest way. However, having a density of 90 g/m^3 at 1 bar, gives rise to big volumes of such hydrogen tanks [Zü03], which is a big issue for mobile application. Research managed to increase the density down to 35 kg/m^3 by multi-layered cylinders made from composite materials reinforced with carbon fibers. Such cylinders are used nowadays in the current fuel cell cars, and industry has currently agreed on using an on-board pressure of 700 bar. Many European projects, such as Hydrogen Mobility Europe [h2me.com], have received funding for technological advancements in grid balancing and optimization as well as on and off-site production. Currently, there are 44 Hydrogen stations operational in Germany and the number increases exponentially throughout the entire continent [Hy]. When hydrogen is stored in a tank, there is no danger of explosion, since as every fuel, it's only flammable in contact with oxygen. However, the energy content is typically much less in comparison to current liquid fossil fuels. Therefore, ongoing research tries finding a lighter way to store high amounts of hydrogen, thereby trying to reach a goal 70 kg of hydrogen per m^3 and a release of hydrogen at temperatures lower than 100 °C.

Liquefying hydrogen is a possibility, which provides a density of 71 kg/m^3 at a boiling point of -250 °C. However, the energy loss in the required process is very large [Zü03]. More than 30 % of the stored

energy is consumed for the liquefaction and this constant loss of hydrogen is unavoidable. This makes the system very inefficient and expensive.

Besides considering the gas and liquid form, storing hydrogen inside a solid is a concept that has been under investigation for the last few decades. Discovered already at the beginning of the 19th century, metal hydrides were considered worthy for systematic studies only towards the end of the century. Hydrogen can be absorbed inside a metal either as a molecule, or as an atom. Molecular hydrogen is bonded on the surface by Van der Waals interactions, which are considered weak, thus results in low temperature stability. New physisorbed hydrides, based on metal organic frameworks, such as MOF 177 can store up to 7.5 wt% hydrogen at 70 bar and -195 °C. In contrast, atomic hydrogen is bonded to the surface with a stronger bond and such hydrides have higher storage capacities. These chemisorption hydrides are divided into four categories [Zü03]:

1) **Covalent hydrides**: Hydrogen is chemically bonded with a non-metal by sharing of electron pairs. The most common example is methane (CH_4), with the highest gravimetric density (mean density of the total content) of all fuels. Its consideration as a combustion fuel, though, is negotiable, since carbon dioxide is produced (43 % less than in the case of coal).

2) **Metallic or interstitial hydrides**: Hydrogen is located in the interstitial sites of the lattice of metals or alloys. Characteristic of these hydrides, are the different stoichiometric compositions in which they can exist.

3) **Ionic hydrides**: An alkali or alkaline earth metal, with an extremely electropositive character, comes into contact with hydrogen. This causes hydrogen to act as a negatively charged ion and the bond is considered almost covalent. Such metal hydrides usually have an elevated gravimetric density.

4) **Complex hydrides**: Hydrogen is covalently bonded to either Al, B or N forming negatively charged complex anions this way. Such metal hydrides are characterized by much higher gravimetric densities of up to 24 wt%. Some examples of anions are: AlH_4, BH_4, NH_2, where the negative charge of these anions is compensated by a cation such as Li, Na or Mg.

Ionic and complex hydrides are in principle the best candidates for storing hydrogen, however, the main drawback of the chemisorbed hydrogen is usually the requirement of high temperatures for release of hydrogen due to strong boning high activation energies. Reversibility over many cycles of hydrogenation/dehydrogenation is also an important consideration [SZ01].

For most hydrides, the temperature and pressure of hydrogen control the reversible reaction of metal and hydrogen into a metal hydride. If the pressure is high and the temperature is low, absorption of hydrogen takes place and the hydride can be formed. However, if the pressure is low and the temperature is high, the reaction favors the separation of the metal and the hydrogen, for entropic reasons. In general, a chemical reaction of hydride formation is formally described for any Metal (Me):

$$\frac{2}{x}Me + H_2 \xleftrightarrow{\text{Pressure/Temperature}} \frac{2}{x}MeH_x \tag{1}$$
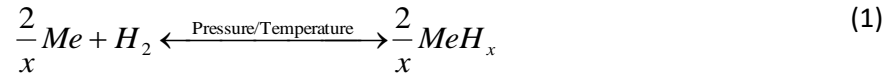
Whereas physisorbed hydrogen is usually bound too weakly, in chemisorption, high temperatures are required for hydrogen release, due to a high thermodynamic stability. The thermodynamic stability of a hydride depends on the sign of the Gibbs free energy (G) change for the decomposition reaction. From this, it is known that the formation or decomposition of the hydride only takes place spontaneously if ΔG is negative, when defined as:

$$\Delta G = \sum G_{products} - \sum G_{reactants} \tag{2}$$

If ΔG is positive, the reaction is not favored and if ΔG is zero, thermodynamic equilibrium has been reached.

As a consequence, the amount of hydrogen stored in a metal, depends on the temperature and pressure. In hydrides, the composition of the hydride under variations of pressure and temperature is given by pcT diagrams and they are of particular importance. As shown in the example of Figure 2-1, the relation of the hydrogen pressure to the hydrogen equilibrium concentration in the metal hydride is given for defined temperatures. Such pcT curves have been determined for many hydride materials. At different temperatures, the curves show different plateau pressures. Using these equilibrium pressures, a linear relation can also be drawn between the inverse temperature and the logarithm of the plateau pressure and this way create a Van 't Hoff plot from which the enthalpy of formation can be extracted.
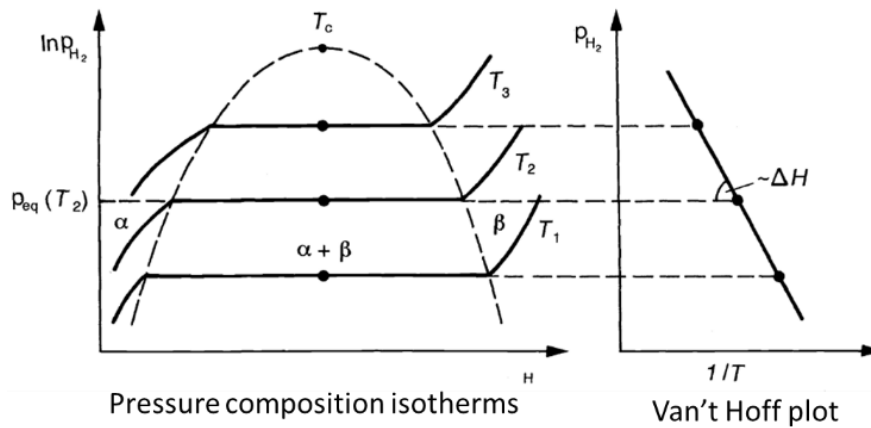

Figure 2-1: Pressure-composition isotherm of a solid solution of hydrogen in a metal (α-phase) and the hydride formation (β-phase) and the van't Hoff plot for estimation of formation enthalpy [LIJ].

Each equilibrium pressure p_{eq} is related to the change in enthalpy ΔH and entropy ΔS, which can be expressed as a function of temperature:

$$\ln \frac{p_{eq}}{p^0} = \frac{\Delta H}{R T_{eq}} - \frac{\Delta S}{R} \tag{3}$$

Where p^0 is the standard pressure, R the gas constant, and T temperature of the system. For the systems studied here, more details will be given in the upcoming chapters.

2.2   Kinetics of diffusion

In order to obtain a new phase, hydrogen has to disperse (diffundere) in the metal. Phase transformations in the solid state are mostly of heterogeneous nature, meaning that the parent and product phase can be distinguished by an interface in all stages of the reaction. The kinetics of phase formation/decomposition are controlled by the diffusion coefficients of the different species present in the material and, thus, these parameters are of great importance. During this work, the diffusion coefficients that control the formation of the hydride phase will be quantified experimentally. A brief reminder on the theory of diffusion is given in this chapter, in order to establish Fick's laws later needed for the analysis of the experimental data in chapters 5 and 6.

As previously mentioned, the separation of the phases must to be thermodynamically activated. In order to form the hydride phase, the atoms have to diffuse inside the material, a process that requires activation energy which is in this case provided in the form of heat. The speed of atom migration in the material as a function of temperature is then characterized by temperature dependent diffusion coefficients. The phenomenon of diffusion implies the transport of atoms in a solid. These atoms can be of the same nature as the matrix, or different, which is called self-diffusion or hetero-diffusion, respectively. In this work, focus will be given on diffusion of hydrogen into Magnesium (Mg), Magnesium Hydride (MgH_2), Titanium (Ti), Titanium Hydride (TiH_2), Palladium (Pd) and Titanium Oxide (TiO_2). There are two main mechanisms used to understand the diffusive transport of the atoms inside a crystal. One is the interstitial diffusion, as in the case of TiH_2 formation. In this case, the impurity atom is placed on an interstitial site of the crystalline material and can jump towards a neighbor interstitial site. The second case, vacancy mechanism, involves the possibility that an atom migrates in an empty site of the matrix. These two mechanisms are part of a more complex system, but they are often addressed to describe numerous problems in materials physics, such as diffusion of doped materials or interstitial diffusion during hydrogenation. More detailed description of these diffusion phenomena is given in the book of Diffusion and Mass transport in solids [Ph91].

There are numerous mechanisms that can describe the diffusion on an atomic level. However, by considering the atoms isolated, the process of diffusion is mostly random and the movement of a solute atom is approximated as a Brownian random movement. By considering a certain concentration of atoms B in a matrix of atoms A, the first Fick's law can be established, which considers the flux of movement (J_B) of atom B in a material. A. Fick, a German physician, was the first to describe the phenomenon of diffusion (in 1855) formulating that the gradient of concentration of an atom B (C_B) along the x direction is proportional to the number of diffusion species crossing a unit area:

$$J_B = -D_B^A \frac{\partial C_B}{\partial x}$$

(4)

This expression (1ˢᵗ Fick's law) is equivalent to a thermal flux. It directly relates the flux of atoms diffusing inside the volume, to the gradient of concentration inside the volume by the diffusion coefficient of the moving species (hydrogen for this work) inside the metal. Figure 2-2a) illustrates this gradient of concentration along a metal. During this work, the concentration of hydrogen over time cannot experimentally be measured with sufficient accuracy. Therefore, focus is given on the chemical potentials instead. The driving force for transport, in all cases is the difference of chemical potential between two interfaces. Focus is given in estimating the diffusion limits of the hydrogen transport process. Naturally, two possibilities can be observed in nature: a) Interfacial barriers, which slow down the growth and introduce a linear regime in the kinetics growth. This usually dominates the initial stages of a reaction. b) Fast interfacial transport, but self-limitation by the growing product slows down the growth and introduces a parabolic regime in the kinetics of growth. The latter usually dominates the later stage of a reaction. At the end of a reaction, entirely parabolic growth is expected. The nature of interfaces between different elements/phases varies broadly and this will lead to very different kinetics behaviors. Figure 2-2b) illustrates the gradient of the chemical potential along a diffusion zone for the two cases mentioned above a) for linear and b) for parabolic growth law.
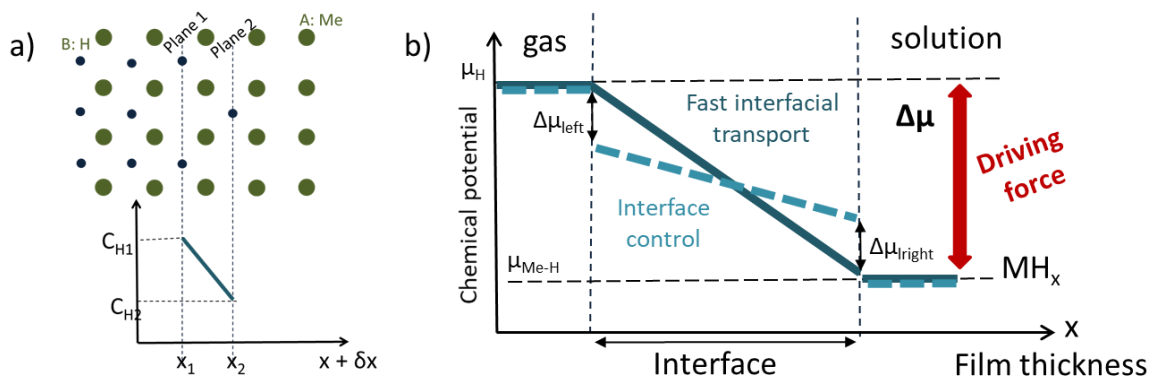

Figure 2-2: Schematic representation of a) 1st Fick's law showing the gradient of concentration changing inside the material where green atoms represent the matrix of the metal and blue atoms the hydrogen interstitials and b) the inter-diffusion potentials across the diffusion zone for the two cases of linear (dashed line) and parabolic (solid line) growth kinetics.

The driving force for transport can therefore be calculated based on:

$$\Delta\mu := \mu_H - \mu_{Me-H} \tag{5}$$

where μ_H represents the chemical potential of hydrogen atoms in the outer atmosphere form and μ_{Me-H} the chemical potential of H in the Metal solution.

The chemical potential is an energetic measure of the general tendency of a substance to transform. It's a form of energy that is absorbed or released during a phase transformation (or any reaction). The higher the value of μ, the more active or more bustling a substance is. In contrast, the smaller the value, the more passive a it is. The chemical potential is therefore strongly dependent on the nature of the substance and its concentration. Furthermore, the chemical potential of gases is sensitive to

changes of pressures, according to a logarithmic relation between the chemical potential (μ) and pressure (p). In cases where the transformation depends on both gas pressure and temperature simultaneously, the chemical potential can be expressed by:

$$\mu = \mu^0 + \frac{RT}{2} \ln \frac{p_{H_2}}{p_0} + \frac{\partial \mu^0}{\partial T}(T - T_0) \tag{6}$$

where R is the fundamental gas constant and μ^0 represents the chemical potential of hydrogen at standard conditions. While the molecular hydrogen has $\mu^0(H_2/g) = 0$ by definition, the atomic hydrogen has a slightly higher potential of $\mu^0(H/g) = + 203$ kJ/mol, which reflects its tendency to form hydrogen molecules.

Following Deal-Grove model [TSE17], which is based on the growth of an oxide layer on the surface of a material, the flux through the interface and the phase can be expressed by:

$$j_{left} \approx \kappa_{left} \frac{\Delta \mu_{left}}{RT} \quad ; \quad j_D \approx \frac{D}{x} \frac{\Delta \mu_D}{RT} \quad ; \quad j_{right} \approx \kappa_{right} \frac{\Delta \mu_{right}}{RT} \tag{7}$$

Based on the scheme shown in Figure 2-2b). This model assumes that the reaction occurs at the interface between the surface and the material and, thus, it is necessary to consider that, in this case, hydrogen diffuses from the gas to the surface and from the interface towards the solution (bulk) of the material where it reacts to form the hydride. It is implicit that these steps proceed at a rate proportional to the concentration of hydrogen. In steady state, the three fluxes mentioned in equation (7) are equal to each other. Transforming equations (7) and (4) in this way:

$$j \approx \frac{\nu}{\Omega_{sites}} \frac{D}{x + \dfrac{D}{\kappa}} \frac{\Delta \mu_s}{RT} \tag{8}$$

where at small thicknesses, x the effective barrier coefficient κ is dominant (linear kinetics) and when x is high, the diffusion coefficient D becomes dominant (parabolic kinetics).

The two kinetics laws will be described in more detail hereafter.

The atomic transport leads to the growth of the layer:

$$\frac{dx}{dt} \approx \frac{D}{x + \dfrac{D}{\kappa}} \frac{\Delta \mu}{RT} \tag{9}$$

which is integrated to:

$$t \approx f'(D) + f''(\kappa) \tag{10}$$

This model shows the sequential evolution of the layer thickness, while clarifying the essential general features of interfacial barriers. Firstly, they slow down the growth and secondly they introduce a linear regime in the growth kinetics, which dominates the initial stages of the reaction.

2.2.1   Linear Kinetics – interface control

In any system considered, the slowest process is the one controlling the reaction. Being able to calculate the chemical potential and taking into consideration the driving force between the interfaces, the diffusion coefficient can be determined. When the thickness of the layer is small and the diffusion inside the bulk is considerably fast, it can be expected that a transfer of atoms across the interface becomes the kinetically limiting factor (see Figure 2-3). No matter what the detailed atomic mechanism is, the surface transport presents a constant dominant barrier and, therefore, a growth kinetics linear is expected in time.
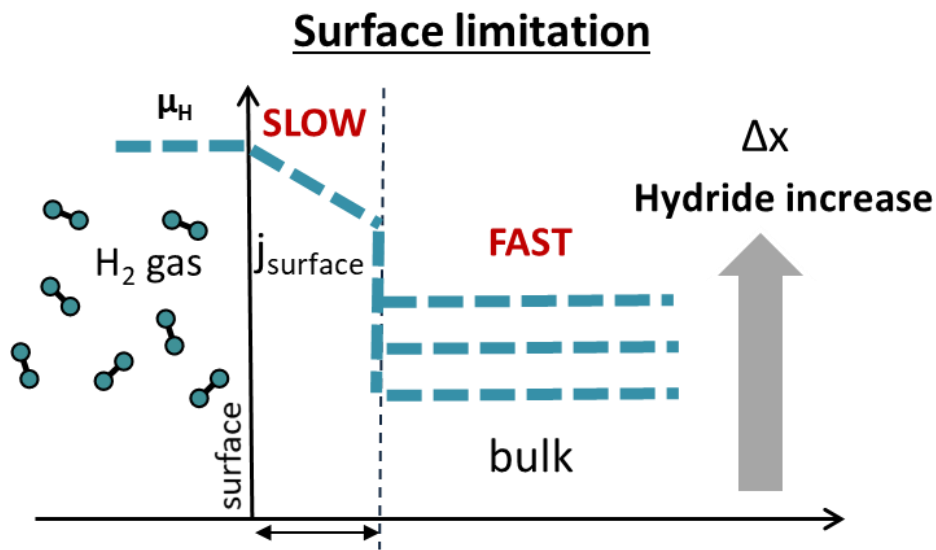

Figure 2-3: Schematic representation of the process along the interfaces in the case of a surface controlled reaction.

Considering equation (8) the flux through the interface (slow process) is given by:

$$j_{surface} = -\frac{\kappa}{RT}\frac{\Delta\mu_s \cdot \nu}{\Omega_{sites}} \tag{11}$$

where Ω_{sites} and ν are cancelled out when the growth of the hydride phase is calculated and the equation is therefore transformed to:

$$\frac{d\Delta x}{dt} = \frac{\Omega_{sites}}{\nu} \cdot j_{surface} = -\frac{\Delta\mu_s}{RT}\kappa \Rightarrow \kappa = \frac{RT}{\Delta\mu_s}\frac{d\Delta x}{dt} \tag{12}$$

Δx describes the thickness of the hydride after a given time. This equation shows the linear behavior of the system. The growth constant κ may depend on the temperature.

If surface transport is limiting, diffusion must be the faster process. Thus, it is required:

$$D_{limit} \geq \kappa \cdot \Delta x \tag{13}$$

This characteristic kinetics regime is illustrated graphically in Figure 2-5.

2.2.2   Parabolic Kinetics – fast interface transport

Staying consistent with the previous arguments, the gradient of the chemical potential is the relevant driving force. When the thickness x increases in equation (8), then the D may become dominant. In this case, the interface transport is fast and the growth is now limited by the diffusivity, meaning it determines how fast the hydride phase is formed (see Figure 2-4). This diffusion transport is in general dependent on temperature.
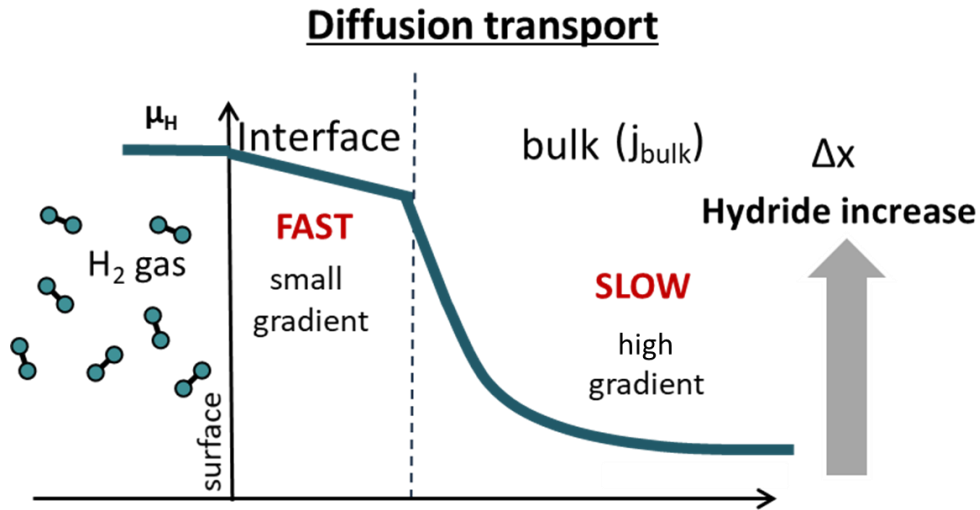

Figure 2-4: Schematic representation of the process along the interfaces in the case of a diffusion controlled reaction.

Considering equation (8) again, the volume diffusion can be calculated by:

$$\dot{j}_{diffusion} = -\frac{D}{RT}\frac{\Delta\mu}{\Delta x}\frac{v}{\Omega_{sites}} \tag{14}$$

where similarly as previously the equation is transformed to:

$$\frac{d\Delta x}{dt} = -\frac{\Omega_{sites}}{v}\cdot \dot{j}_{diffusion} = \frac{\Delta\mu}{\Delta x}\frac{D}{RT} \tag{15}$$

$$\Delta x\cdot d\Delta x = \frac{\Delta\mu}{RT}D\cdot dt \tag{16}$$

Integrating the equation, the square of thickness versus time relation is obtained:

$$D = \frac{1}{2}\frac{RT}{\Delta\mu}\frac{\Delta x^2}{t} \tag{17}$$

From the last equation, the conclusion can also be drawn, that the front of penetration of any given concentration, in this case hydrogen, is proportional to the square root of time. Furthermore, the time required for any point to reach a given concentration is proportional to the square of its distance from the surface and varies inversely to the diffusion coefficient. Lastly, the amount of diffusing elements

entering the bulk medium through unit area varies with the square root of time.

The typical characteristic behavior of both kinetic regimes is shown graphically in Figure 2-5 in two important plotting variants: thickness and thickness squared.
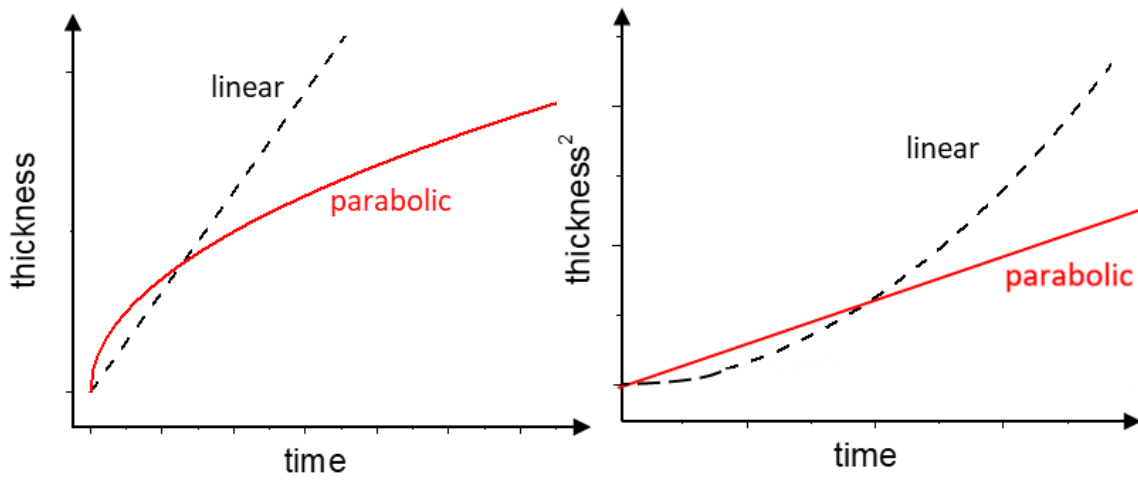

Figure 2-5: Graphic behavior of typical linear and parabolic regimes shown in both plots of thickness and thickness squared versus time.

3 STATE OF THE ART

In this chapter, the recent state of relevant research is summarized. Necessary background information on the materials, some historical facts and what is known so far in literature will be discussed here. A small part is devoted to information about the hydrides used in electrochemical cells (batteries). However, this is not the focus of this work and therefore, only essential information will be given.

3.1 Magnesium/Magnesium hydride

Magnesium was named from Magnesia, a district of Thessaly in Greece were it was first found. It was discovered in 1618, when a farmer in England attempted to give his cows water from a well and they refused to drink, due to bitter taste of the water. Remarkably, the farmer noticed that water seemed to heal scratches and wounds, which was eventually recognized to be magnesium sulphate ($MgSO_4$), the well known today as Epson salt.

Magnesium is a very light metal, with a density of 1.738 g/cm^3 in its solid state. Its heat of fusion is equal to 8.48 kJ/mol and that of vaporization reaches 128 kJ/mol. Due to its abundance and low cost, interest in using it as a solid-state hydrogen storage material is vast. Most importantly, magnesium reacts with hydrogen and forms MgH_2 with high gravimetric density ρ_g = 7.6 wt.% and high volumetric hydrogen density ρ_v = 110 g H/l. Compared to the categories previously mentioned, MgH_2 belongs to the ionic hydrides since Mg as an alkaline earth metal is very electropositive. San Martin and Manchester [SM87a], presented the Mg-H phase diagram at 100 bar first in 1987. Investigating the solubility of hydrogen in the bulk has been challenging, due to the high vapor pressure and chemical reactivity of Mg. The phase diagram between Magnesium and Hydrogen is presented in Figure 3-1, at 1 bar measured by Abdessameud et al. [AMM14]. The Mg-H system consists of hcp-Mg, the interstitial solid-solution of H in Mg (α-Mg) close to the hcp structure of pure Mg and the hydride (β-MgH_2), which is represented by the horizontal line at 0.66 molar fraction of H in Figure 3-1. The hydride phase decomposes at T = 287.6 °C and the melting point of Mg is at T = 650 °C. Hydrogen solubility in Mg has been of great interest in many experimental studies [Do07], [Ma11]. The solubility limit is found to be very low and it's calculated, first by San Martin and Manchester, to be at room temperature c_H = 3 · 10^{-7} H/Mg [SM87a].

It has been reported that the β hydride phase is transformed from its original tetragonal structure into a metastable phase when exposed to high compressive stresses. Describing the Gibbs free energy as a function of the volume and temperature, computation of the temperature (T) - pressure (p) phase diagram of MgH_2 (and its isotopes) was performed by Crivello et al. [Cr16a], as shown in Figure 3-2c). Two other phases appear at higher pressures γ-MgH_2 and δ-MgH_2. Table 1 gives more details about

the crystal structures of Mg and its hydrides. During this work, 10-20 bar (0.002 GPa) were used and 20-300 °C (≈ 450 K), which gives rise only to the β-MgH$_2$ phase to be formed. Therefore, no further consideration is given to the phases stable at higher pressures. Figure 3-2a) shows the hexagonal structure of pure Mg and b) the tetragonal MgH$_2$ with the big circles representing Mg and small circles the hydrogen atoms. As demonstrated in Figure 3-2 Mg atoms are six-fold, octahedrally coordinated by the H atoms. Each MgH$_6$ octahedron shares the hydrogen atoms at its corners with neighboring octahedral. Each hydrogen atom is shared by three octahedrons and is therefore coordinated by three Mg atoms.

Table 1: Crystal structure information on the MgH$_2$ phases, data obtained by Crivello et al. [Cr16a].

| PHASE	TYPE OF STRUCTURE	a (nm)	b (nm)	V (Å^3)
Mg	hcp	0.321	0.321	
β-MgH$_2$	TiO$_2$ (rutile)	0.450	0.301	61.07
γ-MgH$_2$	α–PbO$_2$	0.450	0.541	120.06
δ-MgH$_2$	Distorted CaF$_2$	0.466		101.55
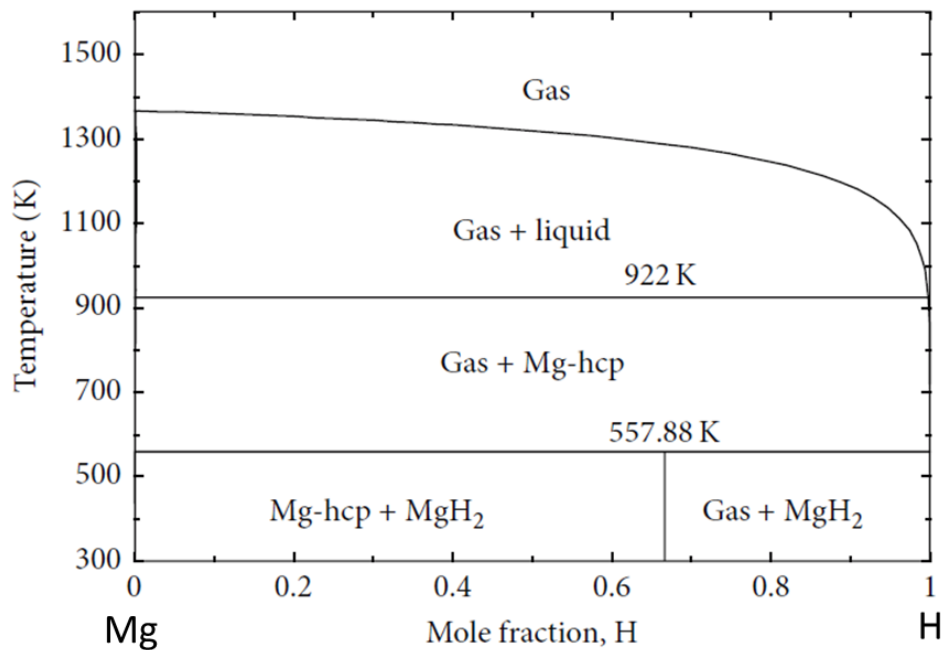
Figure 3-1: Phase diagram of Hydrogen - Magnesium at 1 bar [AMM14].

The critical drawback of MgH$_2$ that hinders its use in current applications, is its high stability, e.g. unfavorable thermodynamics and slow kinetics for hydrogen uptake and release. Its unfavorable thermodynamics is due to the strong Mg-H bond, which causes a pronounced reaction enthalpy and thus very low desorption pressure or high desorption temperature. The enthalpy of decomposition, is measured to be $\Delta H_{dec} \approx 75$ kJ/mol [Do07]. Calculated from the enthalpy of decomposition and the reaction entropy $\Delta S_0 = 0.13$ kJ/mol, for a bulk sample, the hydrogen release temperature at 1 bar is equal to T = 300 °C.
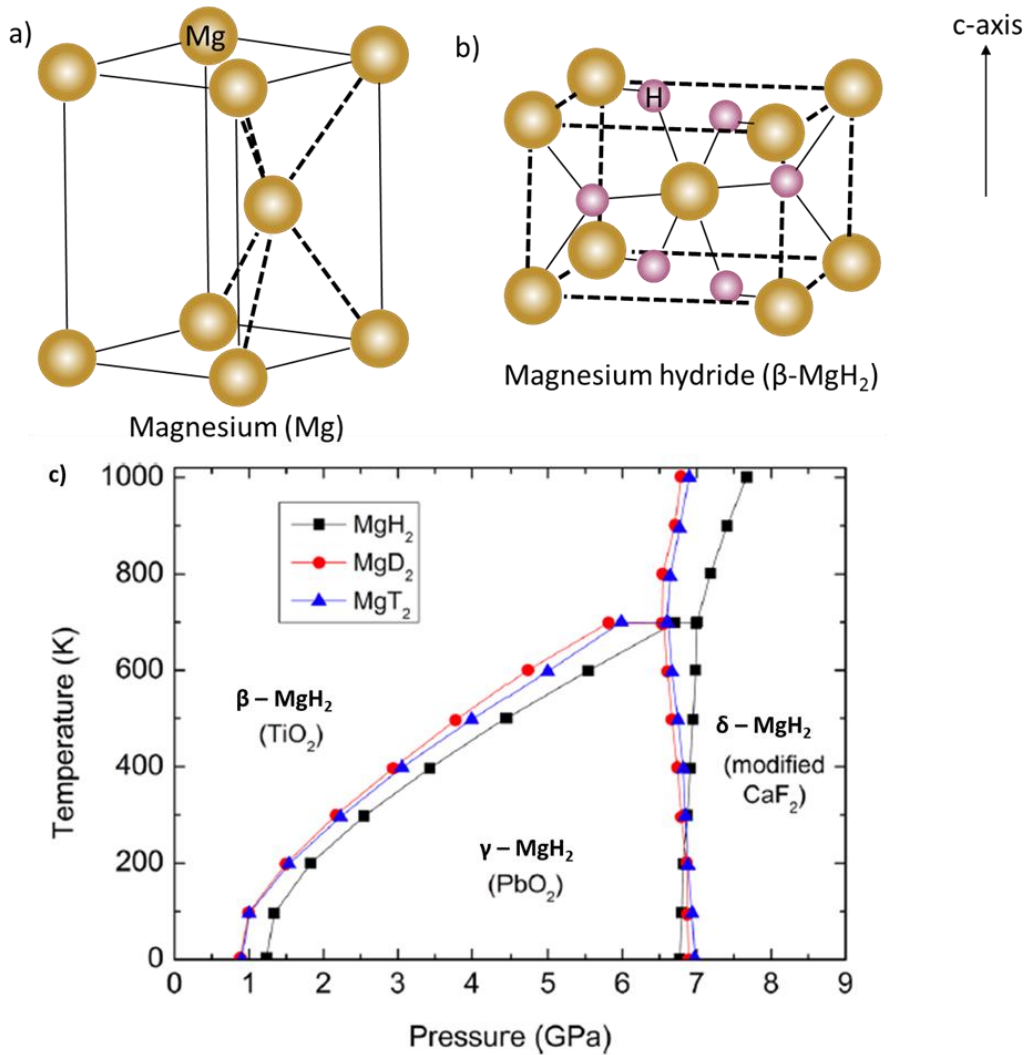
Figure 3-2: a) hexagonal close packed (hcp) structure of metallic Mg (space group P6₃/mmc, b) rutile-type tetragonal structure of β-MgH₂, (space group P4₂/mmm), c) Phase diagram of MgH₂ at different pressures. During this work a maximum of 20 bar at (0.002 GPa) and temperatures from room temperature to 300 °C (≈ 450 K) were used, where only the β-MgH₂ phase is stable.

For a pure Mg layer at room temperature, the absorption of hydrogen is slow, because the dissociation rate of hydrogen molecules at the surface is low. Furthermore, MgH₂ also shows high reactivity towards oxygen and moisture. The natural magnesium oxide layer created on the surface of Mg once it's exposed to air, prohibits fast hydrogen absorption [Do07], [ALJ99]. According to literature, this MgO layer is about 2.5 nm, with negligible increase in its thickness over time [Ch97], [FMO02]. In practice, Mg powders require temperatures above 330 °C in order to achieve reversibility in hydrogen loading. For this reason, using Pd to cover the Mg layer is a common practice in experimental work, in order to avoid the formation of MgO as well as speeding up the splitting of the hydrogen molecule in atoms. It is important to note that the Pd coating does not alter the thermodynamics of the system, but only lowers the barrier in the first step of the process, which is the dissociation of hydrogen molecules on the surface of the material. The diffusion coefficient of hydrogen in Pd is D_H^{Pd} = 3 · 10⁻⁷ cm²/s at room temperature [Ho70].

With increasing hydrogen concentration in a metal, the interactions among the H atoms become important, since the lattice is expanding and the phase transition into the hydride phase takes place.

As previously mentioned, the hydride formation is described by the hydrogen absorption isotherm diagrams. The study of absorption/desorption properties of Mg/MgH$_2$ has been of great interest. A pcT diagram was experimentally demonstrated by Saita et al. [Sa07] for Mg as shown in Figure 3-3 a). The plateau observed on the isotherm curve represents the range at which α-Mg and β-MgH$_2$ coexist. Its width provides the miscibility gap in the phase diagram at the specific conditions. At a higher hydrogen concentration, the pure hydride phase is found and the hydrogen pressure increases steeply with further increasing concentration.
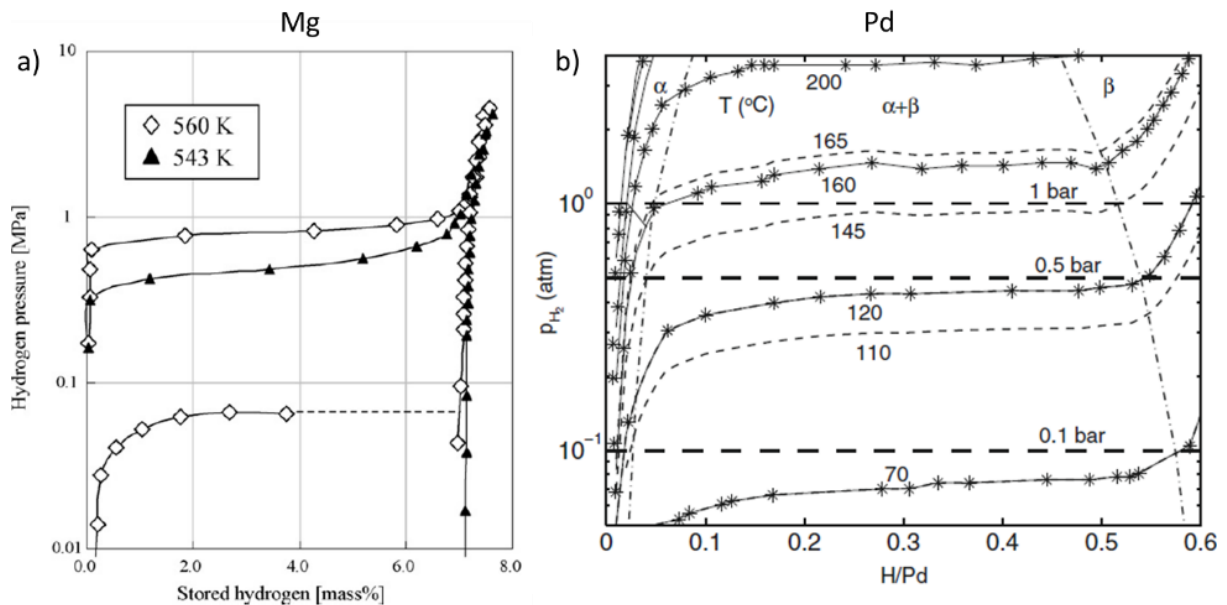

Figure 3-3: pcT diagram of a) Mg [Sa07] and b) Pd [Jo10].

Similarly, Johansson et al. [Jo10] studied the Pd-H system and the pcT diagram is shown in Figure 3-3b). In the Pd-H system, there is no change in the matrix of the metal upon hydrogen adsorption. Both are fcc, however, pure Pd has a lattice parameter a = b = c of 389.07 pm and PdH has a = b = c 403 pm.

Figure 3-4 represents a Van't Hoff plot corresponding to the transitions of Mg-MgH$_2$ and Pd-H. As previously discussed, a Van't Hoff plot indicates the direction of the sorption process for each element and it is related to the pcT curves. It is noteworthy, that by extrapolating the reported data in Figure 3-3 to room temperature, the plateau pressure for β-MgH$_2$ is p_{H2} = 10^{-6} bar, which is 4 orders of magnitude lower than that of bulk β-Pd formation.

The formation enthalpy, which is represented by the slope of the fitted line in Figure 3-4, is negative. This means that both, Mg and Pd heat up while absorbing hydrogen. The reaction heat may give rise to problems of heat transport during cycling of the material.
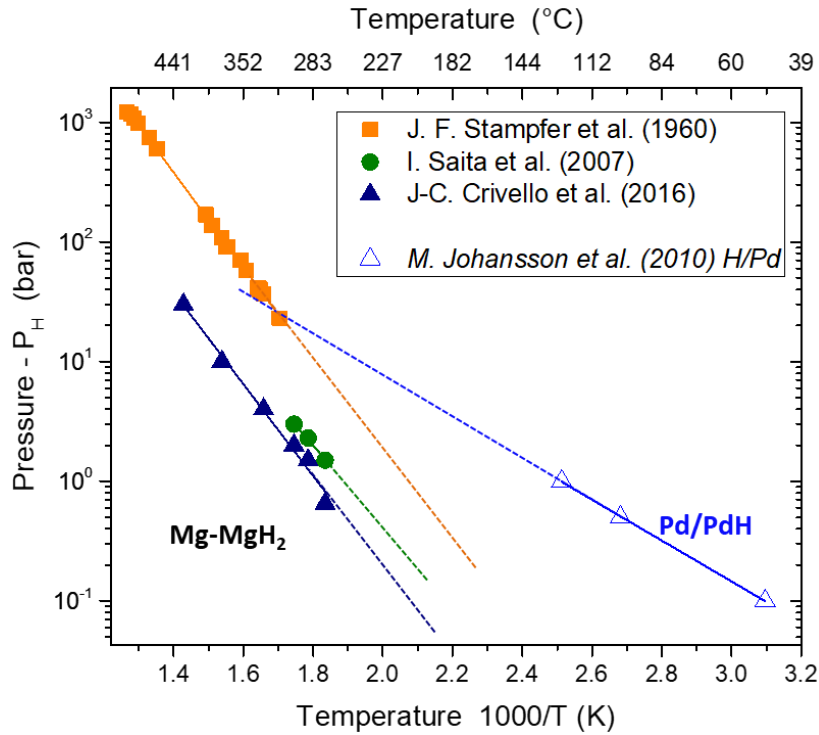
Figure 3-4: Van't Hoff plot for Mg-MgH$_2$ (filled symbols) and Pd-PdH (empty symbol).

Another important parameter necessary to keep in mind, is the fact that Mg diffuses into Pd at low temperatures. Okamoto et al. [Ok10] have improved the Mg-Pd phase diagram obtained from 1985. The revised Mg-rich part of the phase diagram is shown in Figure 3-5. Many different Mg-Pd phases are possibly formed in the interfacial region. Also their crystal structure is well known and discussed by Makongo et al. [Ma06].
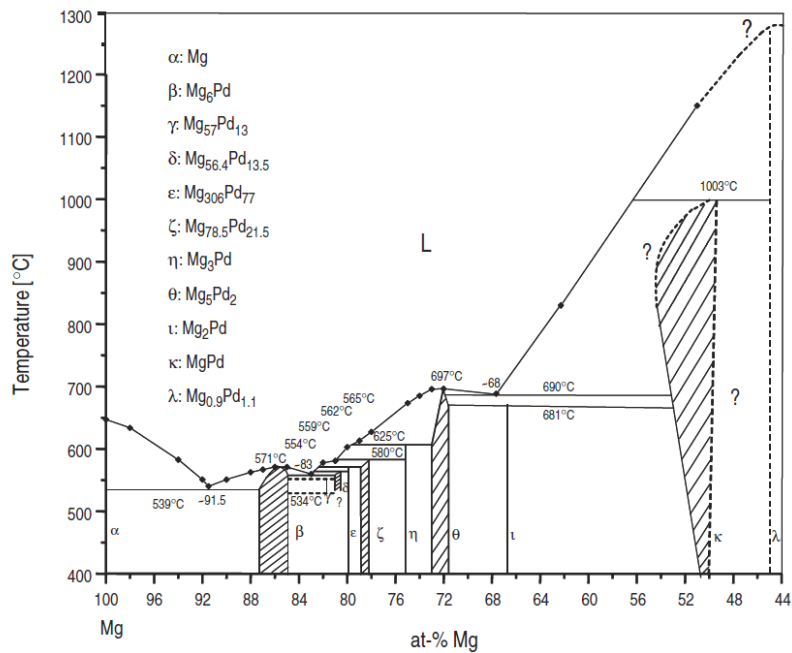

Figure 3-5: Mg-rich part of Mg-Pd phase diagram [Ma06].

3.1.1 Hydrogen sorption kinetics in Mg

As mentioned previously, the biggest drawback of Mg for hydrogen storage is its slow kinetics. The origin of this slow kinetics is mainly attributed to the slow diffusivity of H atoms through the hydride and the metal [Uc15]. The diffusion coefficient of hydrogen in metallic Mg has been experimentally demonstrated to be $D = 10^{-7}$ cm^2/s at room temperature. Figure 3-6 shows the reported sparse litera-ture data on diffusion coefficients of Hydrogen in Mg and MgH$_2$. The diffusion coefficients differ strongly in the relevant two phases. In the α-Mg phase, hydrogen diffuses much faster via interstitial diffusion, while in the β-MgH$_2$ hydrogen diffuses several orders of magnitude slower. In 1993, P. Spatz et al. [P.93] determined the hydrogen diffusion coefficient of MgH$_2$ and showed it to be as low as $D = 10^{-20}$ cm^2/s at room temperature. They studied Mg thin films of few Å thickness and for the first time-have shown that the hydride is preferentially formed at the Pd-Mg interface and forms a diffusion barrier for subsequent diffusion of hydrogen. More recently in 2017, Teichmann, N. et al. [THP17] showed experimentally that the effective H diffusion coefficient in lateral Mg film direction, is in the order of $D = 10^{-8}$ cm^2/s at room temperature. They attribute this high value of hydrogen diffusion to the preferential H diffusion along the Mg/MgO interface, anisotropy of diffusion coefficients and low-ering of diffusion energy barrier upon anisotropic film expansion. Despite many variations within ex-perimental investigations, it has experimentally been accepted today [Cr16b], that the hydrogenation in this system is controlled by the diffusion through the MgH$_2$ layer created over hydrogenation, since the diffusion of hydrogen in the new phase is significantly decelerated. The kinetics of diffusion through Mg thin films has also been studied by electrochemical measurements, where the amount of hydrogen content in thin films can be estimated as well [P.93]. Significant to note is that since 1993, no experimental data has been obtained on the diffusion of hydrogen into the hydride phase, which motivates this work to quantitatively obtaining the diffusion coefficient of hydrogen in the β-MgH$_2$ experimentally.

The latest research by Mooij et al. [MD13], has shown in 2013 that at low pressures ($7 \cdot 10^{-4}$ bar of H$_2$ pressure) and 10 nm of Mg thickness, the formation of hydride islands is observed by optical transmis-sion. At a slightly higher pressure however, of $1 \cdot 10^{-3}$ bar, the MgH$_2$ domains cannot be distinguished anymore. Furthermore, they note that during dehydrogenation they do not observe any nucleation and growth mechanism.

Knowing the diffusion coefficient of hydrogen at different temperatures one can calculate the activa-tion energy (E_a) of hydrogen diffusion. The activation energy represents the minimum energy required for the atomic jumps and in the case of MgH$_2$, it has not been determined experimentally so far. Pre-cisely, the activation energy (E_a) is defined by the exponential term in the Arrhenius equation:

$$D = D_0 \cdot e^{-\frac{E_a}{RT}} \tag{18}$$

where D is the diffusion coefficient, R is the gas constant and T the temperature. Taking the natural logarithmic of both sides, equation (18) yields:

$$\ln D = \ln D_0 - \frac{E_a}{RT} \tag{19}$$

an equation that has a linear form (y = ax + b) and in the corresponding graph, the y interception represents the value of D_0, while the slope represents (-E_a/R). Since diffusion is expressed in logarithmic scale, the activation energy has a decisive effect on the diffusion coefficient. With regard to Figure 3-6, it is obvious that the Arrhenius slope of the experimental data given in literature can be obtained by extrapolation of only two or three measurements. However, a clear tendency that the slope of the α-Mg is less steep (lower E_a) than that of MgH$_2$, meaning that the reaction is less sensitive to temperature changes than in the case of β-MgH$_2$.
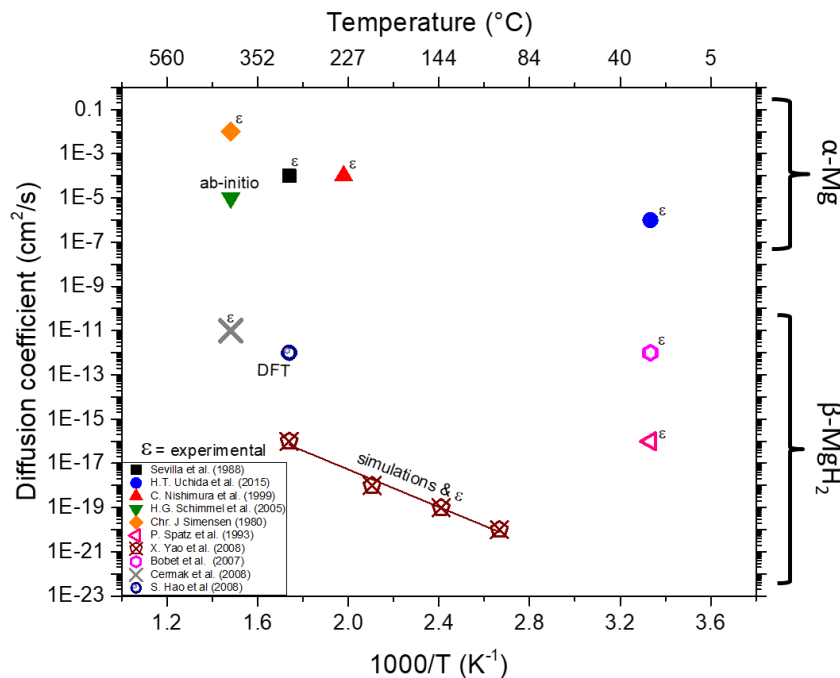

Figure 3-6: Diffusion coefficient of hydrogen in Mg and MgH$_2$. Authors and applied techniques as labelled.

By interpolating the theoretical results by X. Yao et al. [Ya08], shown in Figure 3-6, the activation energy obtained by using equation (18) amounts to 107.9 kJ/mol of H. A large activation energy that is attributed to the fact that the formation of vacancies in MgH$_2$ demands a much higher energy, since the chemical bond between Mg-H is ionic and covalent, and therefore rather strong. Hydrogen diffusion into the hydride grains is, therefore, very slow since the activation energy is so high. However, the fluctuations in the reported values are big, since most experiments are done only at a small range of temperatures and with different techniques.

It is also important to mention, that the activation energy of hydrogen diffusion in Pd has experimentally been determined by J.W. Simons [SF65] by using a Pd wire and hydrogen absorption method in a wide range of temperatures, between room temperature and 400°C. The obtained activation energy

was equal to 23 kJ/mol of H.

While the stability of metal hydrides can be changed by partial substitution of the consisting elements with other atoms - where the delocalized electrons influence the overall stability of the interstitial hydrogen atoms - this is not possible for ionic hydrides such as MgH_2. Here the electrons are strongly localized. Therefore, other routes have been developed to destabilize ionic hydrides. Decreasing the particle size, has been shown to be an efficient way. Lowering the grain size, increases the density of grain boundaries. It was shown by M. Hamm et al. [HP17] that the grain boundaries have a strong influence on the overall hydrogen diffusion coefficient measured in MgH_2. This hypothesis is supported by simulations that show that grain boundaries become the dominant diffusion path when their diffusion coefficient is at least thousand times larger than the volume diffusion coefficient. Ball milling [Fl13], [Hu13], [St10], is the most common technique to reduce the grain size and it increases the volume fraction of grain boundaries [SLH07b]. As indicated by the data shown in Figure 3-6 as well, many published diffusion coefficients might be strongly influenced by the microstructure of the sample. Unfortunately, using only smaller particles is not enough for lowering the enthalpy of formation of MgH_2. Researchers have tried successfully to decrease the stability of the compound by adding transition metals such as Fe, Cr, Ni, Ti, Nb, Pd and many others [Do06]. A compromise between price and performance as well as cyclability is still a concern. Furthermore, nanoconfinement is another recent way studied to improve the desorption kinetics of the hydrides.

Regardless the intensive research activities, the diffusion coefficients and the study of the slow kinetics of hydride formation in this system, is still a surprisingly open field of research and the focus of this work. A way to directly see the phase growth/change and observe the formation process of MgH_2 is proposed here. With the help of X-ray diffraction (XRD), in-situ measurements of resistivity, cross section preparations by focused ion beam (FIB), scanning electron microscopy (SEM) and transmission electron microscopy (TEM), the mechanism of formation of MgH_2 is investigated under different temperatures and pressures. Quantitative measurements of the growth constant and diffusion coefficients will be derived and discussed.

3.1.2 MgH_2 as battery electrode

Another potential application of MgH_2 , is using it as a battery electrode. Magnesium has been used in its metallic form as an anode, due to its theoretical charge capacity and high energy density. At the moment, there are commercially available Mg batteries with aqueous electrolytes, mostly used for military applications, because of the fast self-discharge. Magnesium water activated, Mg-air batteries and rechargeable magnesium batteries are also under further investigations, however, not commercially available yet. However, magnesium compounds, can also be used in Li-ion batteries. Due to the

high demand in reliable batteries, moving from pure Li batteries to alternatives is a high challenge in today.

In 2008, Oumellal et al. [Ou08] [Ou08] proposed the use of metal hydrides as electrode materials for lithium-ion batteries. Metal hydrides belong to the materials undergoing a conversion reaction with lithium according to the general equation:

$$MH_x + xLi^+ + xe^- \leftrightarrow M + xLiH \tag{20}$$

During lithiation, the hydride is reduced to its metal and lithium hydride (LiH) is formed. Based on the nature of the hydride, the lithiation can be completed in one step or more. Metal hydrides are promising candidates for future lithium-ion batteries, because they have: a) Interesting working potential window, generally between 0.1 V and 1 V vs. Li+/Li, suitable to the application as an anode, b) higher theoretical capacity compared to graphite (375 mAh/g) and c) in comparison to other conversion compounds, metal hydrides, show the lowest polarization. Polarization is a side-effect observed in electrochemical reactions developed at the interface between electrolyte and electrode and can drastically influence the reaction mechanism over cyclability. Such side effects can be the accumulation of gasses at the electrode interface, SEI (solid electrolyte interface) formation, concentration gradients, etc. Hydrides appear to have a good interface contact with specific electrolytes, lowering the effect of polarization. On the other hand, the slow kinetics at room temperature and the short cycle life are still important concerns that need to be improved before using metal hydrides as electrode materials in practical energy storage applications.

The first hydride studied for its lithium ion reactivity was MgH_2 in 2008 by Oumellal et al. [Ou08]. They characterized the process of MgH_2 lithiation by XRD patterns at the different lithiation steps during cycling of powder-pressed batteries in a liquid electrolyte. Unfortunately, their bad reversibility has not allowed the expected breakthrough and afterwards, different approaches have been suggested in order to enhance the cycle life of this electrode. It has been reported that the Mg-Li alloy reaction at very low potential (0.1 V) is one of the limitations against cyclability. Consequently, Aymard et al. [AOB15] have shown a significant increase in the reversibility by stopping the cycle at 0.15 V. They also argue that this lowers the volume expansion in the cell, since the Mg-Li alloy reaction has an excess volume of 200 %, whereas the conversion reaction between MgH_2 and Li only increases the volume by only 83 %.

Furthermore, ball milling of the powders has been shown to improve the cyclability of the cells. Brutti et al. [Br12] have shown that nano-sized powders show better electrochemical activity, similarly as in the Mg absorption/desorption cyclability. A similar approach by altering the particle size of the electrode was studied by Oumellal et al. [Ou14], where they showed that composite MgH_2 nanoparticles dispersed into porous C-scaffold can enhance the electrical conductivity of the electrode and, therefore, increase the cyclability. They were able to reach 500 mA/g over 100 cycles using this electrode

composite material.

Zaïdi et al. [Za11] studied the effect a binder can have on the reversibility of the cell. They used carboxymethyl cellulose (CMC) and carboxymethyl cellulose-formate (CMC-f) as binders for MgH_2 electrodes and showed initial reversible capacity of $\approx$ 90 % of the theoretical expectation, however there was still a capacity retention of $\approx$ 20 % after 40 cycles. This improvement has been attributed to the mechanical stability of the binder to accommodate the volume changes during cycling.

Different catalysts, such as transition metals, but also transition metal oxides and halides, have been reported in literature to improve the kinetics of MgH_2 during H_2 absorption/desorption cycles [SCL16]. Therefore, it was suggested to study the effect of transition metals with respect to the improvement of electrochemical reactions. Following this idea, Zeng et al. [Ze15] showed the effect of Nb_2O_5 additives on MgH_2 as electrode material, obtaining a higher reversibility with also a flatter plateau potential, implying a better kinetics, probably due to a faster diffusion of hydrogen atoms into the electrode. Nowadays, also solid state electrolytes for lithium ions batteries attract attention for replacing the liquid electrolytes. Islam et al. [Ik13] investigated the electrochemical properties of MgH_2 as a solid state electrolyte system. Several complex hydrides have shown to have promising ionic conductivity, such as $LiBH_4$, $LiBH_4$-$LiNH_2$, $LiAlH_4$-Li_3AlH_6 [Ma09b], [MO11], [Ma09a], [Og10]. These hydride solid-state electrolytes work well, at least at slightly elevated temperatures ($\approx$ 200 °C), at which conductivity becomes comparable to that of liquid electrolytes. Cells using such electrolytes have shown high discharge capacity even at high current densities, featuring also a flatter plateau and smaller polarization effect [Ma09b], [Og10].

Despite many attempts with all the mentioned partial improvements, MgH_2 is still not ready to be introduced in the market as electrode material. The poor capacity retention at room temperature still remains the main issue to overcome. Hence, more research efforts are needed to find the right optimization for practical applications.

During this work a collaboration was created between ECOSTORE partners of the funding (Marie Curie ITN n° 607040 – Novel complex metal hydrides for efficient and compact storage of renewable energy as hydrogen and electricity). MgH_2 thin films were prepared in Grenoble and cycled in CNRS in Paris. The characterization by FIB-cross sections and TEM of these thin film electrodes was completed within the frame of this work and the results will be discussed in the later chapters.

3.2   Titanium/Titanium hydride/Titanium oxide

Titanium is the ninth most abundant element in Earth's crust (not in its pure form) and the fourth most abundant metallic element. It was first discovered in 1790 in England by reverend William Gregor. However, it was named five years later, by the German chemist Martin Heinrich Klaproth, which he named after the "Titans", the sons of goddess Earth, from Greek mythology. The name seems to be

very appropriate, since it indicated the advantageous characteristics of this element: light weight among the transition metals (it weighs 56% less than steel), high strength to weight ratio, flexible with low elastic modulus (112 GPa) [SR10], resistant to corrosion and erosion, high thermal conductivity, as well as low coefficient of expansion. It is an element that also has an important biological role (as a biocompatible metal in medical implants), but its role in aerospace industry as a structural material is similarly essential.

The interaction of titanium (Ti) with hydrogen (H) is of high interest in a variety of different applications. Significant work shows hydrogen embrittlement of Ti components [Se04], as well as the influence of titanium hydride (TiH_2) in biocompatible Ti implants [Sh07] for controlling the surface roughness. TiH_2 is also used as a foaming agent in the production of metal foams [LR04]. Additionally, the adoption of TiH_2 as a possible negative electrode in rechargeable lithium-ion batteries [Ou09] and as a high-temperature-metal hydride in a solar power plant (as a thermal energy storage system) becomes relevant today.

Moreover, Ti is of general interest in the field of metal hydrides for solid-state hydrogen storage materials. Due to its low gravimetric density of 4 wt.% [SLH07a], but also because of the high stability of TiH_2, pure Ti is not of great interest as a hydrogen storage material, despite its high affinity to hydrogen. However, titanium alloys have attracted attention regarding their catalytic effect to other hydrogen storage materials. It has been reported that pure Ti (and other transition metals) improves the sorption kinetics of other interesting metal hydrides, such as $NaAlH_4$ and MgH_2. Hence, considerable effort has been expended towards investigating H diffusion in Ti for various applications.

In 1987, the same year as the Mg-H system and in the same group, San-Martin et al. described the phase diagram of Ti-H for the first time. The appearance of a simple eutectoid system of β- titanium hydride to α-titanium and δ-titanium hydride in a temperature range from -273 to 900 °C was shown, with a composition of 0 to 60 at.% hydrogen. A more detailed description was given by Y. Fukai [Fu05], with a larger temperature (-273 – 1800 °C) and composition (0 – 100 at.%) range at a pressure of 300 bar. This phase diagram is shown in Figure 3-7. Further, theoretical calculations of phase diagrams presented in the work of Wang et al. [Wa96] are in agreement with the shown experimental data. Their calculated phase diagrams at different pressures from 1 bar up to 370 bar have shown little variation with pressure, especially at the temperature and pressure range studied in this thesis (18 °C – 300 °C and 1 bar – 100 bar).

The α-Ti phase occurs at temperatures below 900 °C. Without the presence of hydrogen, the α-titanium transforms into β titanium at temperatures above 900 °C. The melting temperature of titanium is at 1650 °C. The hydrogen solubility in the α phase increases with temperature up to a maximum of ≈ 10 at.% is reached at about 450 °C. The titanium hydrogen system is an eutectoid system with an

eutectoid temperature of $T_e \approx 300\,°C$. The solubility limit for α-titanium at this temperature was exper-imentally determined to be ≈ 6.7 at.% by Setoyama et al. [Se04]. A recent theoretical DFT calculation for the hydrogen solubility in α-titanium at 325 °C of ≈ 7.2 at.% [Po16a] is in good agreement with the experimental results.

The solubility range in the β-titanium hydride phase is much broader and can vary from 0 - 60.32 at.% hydrogen. With increasing hydrogen concentrations, the transition temperature from α-titanium to β-titanium hydride decreases until the eutectoid composition of ≈ 39 at.% hydrogen is reached at $T_e \approx$ 300 °C [KZ70]. The composition range of δ-TiH_2 is between 51.22 - 66.67 at.% hydrogen. This range depends on the respective temperature and pressure conditions. At temperatures below 300 °C, the phase transformation from α-titanium to δ-titanium hydride occurs without a previous β-titanium hy-dride formation. As many studies show, the decomposition of the δ-titanium already takes place at a temperature around 500 °C and finishes after reaching approximately 800 °C. This is however depends on the dimension (e.g. particles, films, bulk), pre-treatment of the samples (oxide layer on the surface) and heating rates [Ga11a].
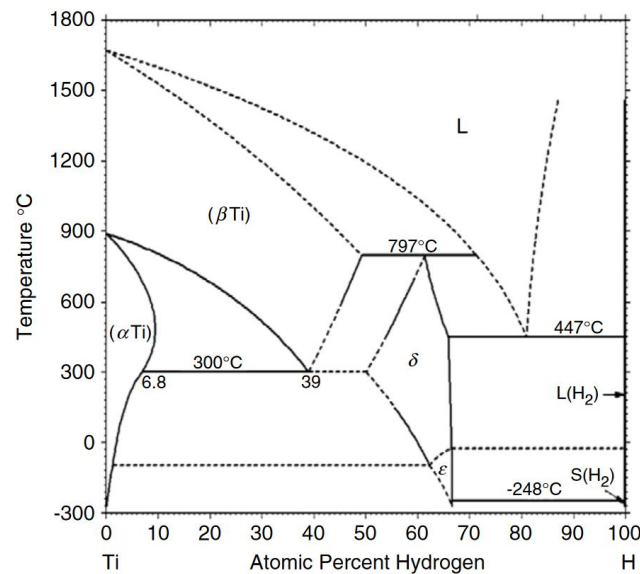
Figure 3-7: Phase diagram of Hydrogen - Titanium at 300 bar [Wa10].

The different structures, lattice parameters and volume of the titanium and titanium hydride phases are listed in Table 2. The α-titanium has a hcp structure, the β-titanium a bcc structure and the δ-titanium hydride an fcc structure. Hydrogen should be solved in the α-titanium only on the tetrahedral interstitial lattice sites. Nevertheless, theoretical ab-initio calculation by Bakulin et al. [Ba16] state, that occupation of all interstitial sites seems to be stable. In the δ-titanium hydride phase the hydrogen atoms are dissolved on the tetrahedral lattice sites. With increasing amounts of hydrogen solved in titanium or titanium hydride, the lattice parameter increases. Indeed, this is exemplified for the δ-titanium hydride phase δ-TiH_x, depending on the composition x in Table 2.

Table 2: Structure, lattice parameter and volume of unit cell for different titanium and titanium hydride phases.

PHASE	STRUCTURE	LATTICE PARAMETER (Å)	VOLUME (nm³)	REF.
α-Ti	*hcp*	a = b = 2.95; c = 4.76	0.0361	[R.62]
β-Ti	bcc	a = b = c = 3.33	0.0369	[Le53]
δ-TiH$_{1.23}$	fcc	a = b = c = 4.39	0.0846	[PM82]
δ-TiH$_{1.56}$	fcc	a = b = c = 4.40	0.0852	[PM82]
δ-TiH$_{1.8}$	fcc	a = b = c = 4.44	0.0874	[PM82]
δ-TiH$_2$	*fcc*	a = b = c = 4.46	0.0887	[PM82]

As previously discussed for the magnesium hydride, a characterization of the hydride formation is possible by the hydrogen adsorption isotherms (pcT curves). Figure 3-8 shows the pcT curve of the Ti-H system at different temperatures.
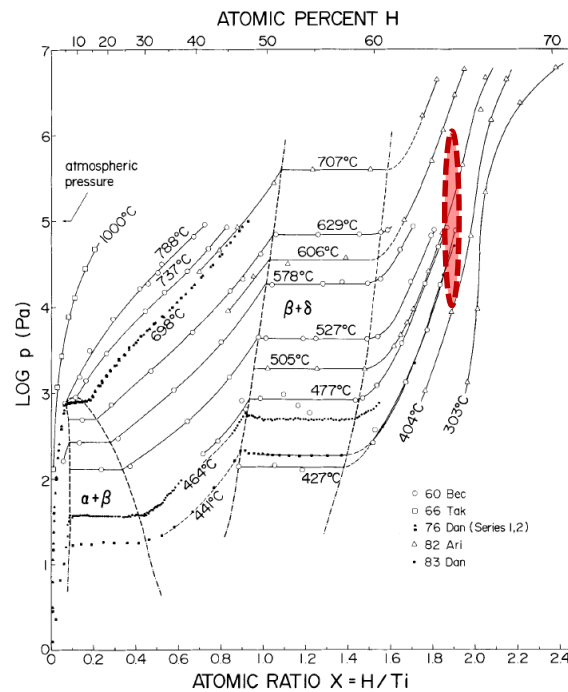
Figure 3-8: P-C-T curves of the titanium hydrogen system over a wide pressure and composition range for elevated temperatures above 300 °C with both phase regions [Wa96].

Available quantitative data for the solution process of hydrogen in a titanium matrix shall be shortly summarized. In the work of Wang et al. [Wa96], a Sievert apparatus was used to obtain the pcT curves. The enthalpy and entropy of formation was determined by plotting the experimental results in a Van't Hoff plot. An alternative experimental method to obtain such thermodynamically data is calorimetry. In Table 3, the dissolution enthalpies of hydrogen in α-Ti, β-Ti and δ-TiH$_2$ hydrides are listed. They all are exothermic, which means that the product of these reactions is energetically more stable than the reactants. Furthermore, the exothermic heat release increases from α-Ti to β-Ti to δ-TiH$_2$ hydride. The energy for breaking the bonds between hydrogen and titanium is the highest for the δ-TiH$_2$ phase.

Table 3: Dissolution enthalpy of hydrogen in the different Titanium/Titanium hydride phases as reported in [Wa96], [Da83].

PHASE	$\Delta H_{formation}$ (kJ/mol H_2)
α-Ti	-91
β-Ti	-133
δ-TiH$_2$	-157

For further information on the thermodynamics of the phase transformation from α-Ti to δ-TiH$_2$, the enthalpy and entropy of formation gathered from different sources is listed in Table 4. In literature the formation entropy is reported to be close to $\Delta S \approx -130$ J K^{-1}mol^{-1} , as recently reported by Fukai et al. [Fu05]. The pronounced variation of the formation entropy in the work of Want et al. [Wa96] can be explained by the different calculation methods of the formation entropies.

Table 4: Formation enthalpy and formation entropy of δ-TiH2.

TEMPERATURE (°C)	$\Delta H_{formation}$ (kJ/mol)	$\Delta S_{formation}$ (J/K·mol)	REF.
450 – 550	-142	-174	[Wa96]
465	-137	----	[Da83]
400 – 700	-179	-145	[ASl82]

With increasing amounts of hydrogen, the Gibbs free energy of formation becomes more negative. The lower the Gibbs energy, the more a reaction is favored to happen spontaneously. In this work, the hydrogenation is studied at 300 °C. So, the most favorable state should be the δ-TiH$_x$, with a composition of x = 2.

Despite many advantages, once exposed to air, Ti directly forms a thin oxide layer of few nanometers in thickness. This effect is sometimes useful in application, when TiO$_2$ is formed purposely to be used as a catalyst in optical biosensors [Do17]. Yet, in most cases it is undesirable. In the case of metal hydrides, there are many unanswered questions, since on the one hand, it has been shown that diffusion of H in the oxide is much slower than in the metal phase [QZS13], which makes it challenging to use Ti as a catalyst on the surface of a hydride. On the other hand, TiO$_2$ has been reported to play a catalytic effect itself, on the dehydrogenation properties of some metal hydrides. M. Daryani et al. [Mo14] milled nanostructured MgH$_2$ powder mechanically with TiH$_2$ and TiO$_2$ particles and have shown, by thermogravimetric analysis during dehydrogenation, that these compounds lower the activation energy of MgH$_2$ significantly. In order to clarify the role of the oxide, its influence on H diffusion in Ti, TiO$_2$ and TiH$_2$ are of great interest. Further details on the passivation layer will be given in the following chapter.

3.2.1   H sorption kinetics in Ti

Hydrogen diffusivity in Ti, TiH$_2$ and TiO$_2$ was studied previously. Figure 3-9 shows some of the reported values for the different diffusion coefficients in the three different compounds: α-Ti (squares), TiH$_2$ (circles) and TiO$_2$ (triangles). Most studies on H diffusion in Ti are done in bulk systems in ideal conditions without a passivating oxide layer formed on the surface [Po16b], [Ga11a], [Ca16], [Ma15]. Diffusion of hydrogen at 300 °C appears to be quite similar in α-Ti and δ-TiH$_2$ with D ≈ 10^{-7} cm^2/s. Obviously, the difference between metal and hydride, is not as significant as it is in the case of other metal hydrides such as MgH$_2$, where a difference of 9 orders of magnitude between the metal and the hydride is stated. In the case of Ti, the hydride phase does not hinder further diffusion of H significantly. From Figure 3-9, it can also be seen (plotted in stars) that simulation studies nevertheless predict a tendency that hydrogen moves slower at higher concentration of hydrogen.
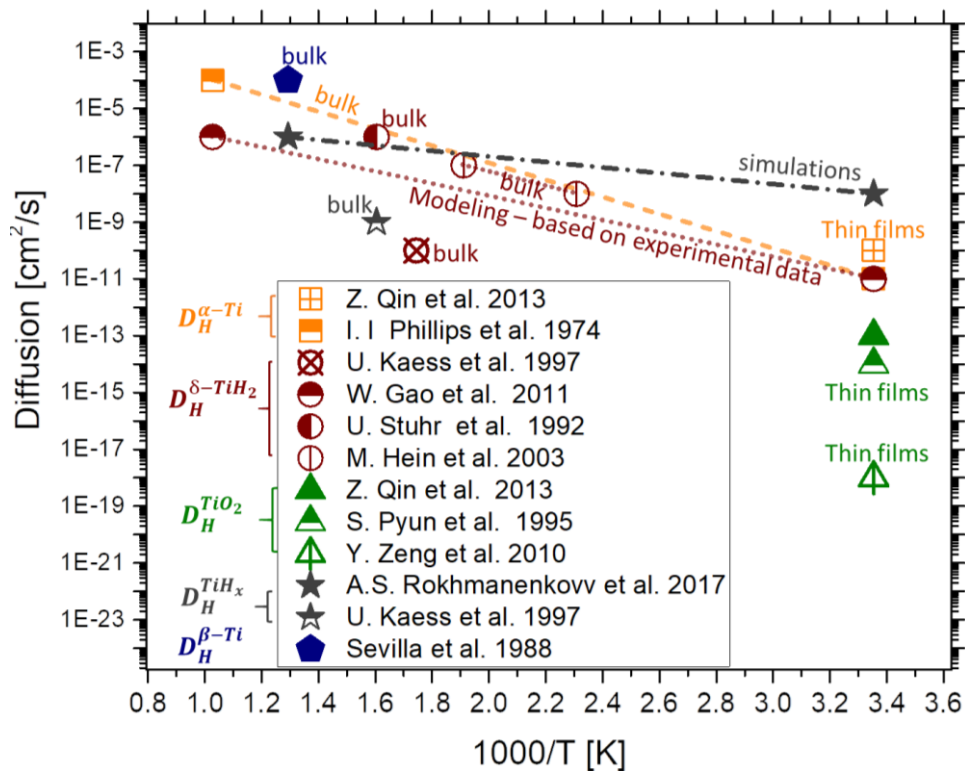
Figure 3-9: Literature data of diffusion coefficients of hydrogen in the different compounds: α-Ti (squares), TiH$_2$ (circles), TiO$_2$ (triangles), TiH$_{x<2}$ (stars) and β-Ti (polygon). Authors and applied techniques are labelled.

The Ti-H phase diagram in Figure 3-7, also shows a β-Ti phase stable at elevated temperatures. Experimental data in Figure 3-9 show that diffusion is faster in β-Ti, which has a bcc structure, than in α-Ti that has an hcp structure. This is to be expected, since bcc structures offer more interstitial sites for H to be inserted. Unfortunately, the bcc phase is only stable at higher temperatures and therefore not interesting for applications.

In the case of TiO$_2$ the values vary strongly. TiO$_2$ films formed by plasma-enhanced CVD on Pd substrates have revealed a diffusion coefficient of hydrogen of 10^{-14} cm^2/s [PPY95], [QZS13]. Thermally

grown TiO_2 on pure Ti substrates show a diffusion coefficient of 10^{-16} cm^2/s [Yu03], while single crystal rutile TiO_2 even shows a diffusion coefficient of only 10^{-20} cm^2/s [Po91]. However, the tendency of systematically slower diffusion through TiO_2, than through α-Ti or TiH_2 seems to be clear. Despite some scatter in the data, all of the above-mentioned papers agree that diffusion of hydrogen in TiO_2 is much slower that in the Ti metal. Thus, the retardation of H permeation by TiO_2 films may be due to a combination of low H adsorption and dissociation at the oxide surface and/or slow hydrogen transport through the oxide. In general, it is difficult to predict the rate of hydrogen transport through a TiO_2 film and how many hydrogen atoms generated on the TiO_2 surface will actually reach the Ti layer each time.

3.2.2   Titanium oxide phases

It is important to realize that different polymorphes of TiO_2 exist. Rutile is the most common one, the anatase (metastable tetragonal structure), brookite (orthorhombic structure) and akaogiite (monoclinic form) are alternatives. The rutile form is the most stable polymorph of TiO_2 and the one naturally formed on the surface of Ti when exposed to air. Evidence of this will be given in the later chapter when a characterization of the samples is discussed. For purposes of this work, all TiO_2 discussed in the results part, concern the rutile TiO_2 phase. Figure 3-10 shows the rutile structure of TiO_2.

The diffusion of hydrogen through rutile TiO_2 has been a key research point for years. It is not a simple case of transport of hydrogen through the layer, since a chemical reaction can also occur between hydrogen and the oxide. Commercially, TiO_2 is used for many applications such as solar cells, toxic materials conversion, air purifying, self-cleaning windows etc. From many studies, it has been shown that the surface defects play a very important role in the chemistry of the oxide. Here, one may ask what happens to the oxide once it comes in contact to hydrogen. Interestingly, a number of phenomena have been suggested for what may appear a relatively simple system, with however no final answer to this question.

The structure of the different oxides created on the surface has been investigated and different suggestions have been reported in literature. One of the most important reviews on this oxide surface has been given by Kunat et al. [KBW04]. For many years, no information was available on whether the hydrogen atoms form an ordered layer on the surface of the oxide [Sh00]. By the Ab-initio calculations by Suzuki et al. [Sh00], indicating that OH species should be stable at the surface once the oxide is exposed to hydrogen atmosphere, many experimental investigations were motivated on this interesting surface. In 2004, Kunat et al. [KBW04] demonstrated experimentally by scanning tunneling microscopy (STM), that exposing the TiO_2 surface to atomic hydrogen at room temperature leads to the formation of a stable and highly ordered hydrogen over-layer containing two hydrogen atoms per unit

cell, one OH and one TiH species. They've also shown that by exposing the surface at higher tempera-tures, up to 230 °C, the hydrogen over-layer varies. At high temperatures, the layer consists only of OH species (1 hydrogen atom per unit cell). It is also known in literature [KBW04], that heating the oxide surface higher than 575 °C gives an excessive loss of the oxygen.
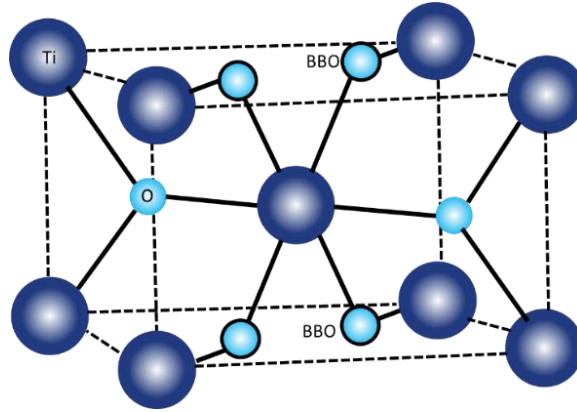

Figure 3-10: Crystal structure of the Rutile TiO_2, indicating the bridge bonded oxygen (BBO) formed.

While most studies focused only on the surface reaction, quite recently, in 2008, Li et al. [Li08] have studied experimentally and theoretically the diffusion of hydrogen in the rutile structure. They suggest that hydrogen diffusion in the rutile oxide proceeds via a two-step mechanism. First the initial diffusion of localized charge followed by the hydrogen diffusion. The presence of repulsive OH-OH interactions on the surface was shown to be significant in both experimental and theoretical calculations.

Kunat et al. [KBW04] studied by helium atom scattering the adsorption and desorption kinetics. How-ever, their kinetics pre-factors as well as their diffusion activation energy determined experimentally, differ significantly from Li's theoretical calculations, pointing out a more complex diffusion mechanism. The surprisingly complex and intriguing behavior of hydrogen on TiO_2 surface, points to a limited un-derstanding of this model surface. Some researchers, [Du12], [ICP11], [Yi08] have also excluded the formation of TiH on the surface. The situation became even more complicated since in 2012, Tao et al. [Ta12] have shown that the bulk adsorption of H is different for the rutile (110) and (011) surfaces.

Regardless the wide activities on this system, the fluctuation and disagreement between different characterization methods is remarkable and numerically shown in Figure 3-9 as well. In this work, the hydrogenation of Ti thin films of controlled thickness (50 to 800 nm) is investigated. The oxide studied during this work is formed naturally by exposing the Ti thin film to air. By measuring the time for full phase transformation from α-Ti to δ-TiH_2, a comparison of the kinetics, with and without the presence of a surface oxide layer, can be made. Also for this comparison, samples were prepared with palladium (Pd) coating, in order to prevent the formation of TiO_2. As in the case of Mg, Pd is known to act as a catalyst for H_2 splitting and, therefore, H absorption occurs faster, eliminating the risk that the oxide surface acts as the barrier to hydrogen absorption. Furthermore, experiments were done to observe the pressure dependency, when an oxide layer is present.

Due to its high theoretical electrochemical capacity and electronic conductivity, TiH_2 was also investigated as electrode material by [Ou08], [Ou14]. Interestingly, the conversion reaction taking place during the lithiation of TiH_2 differs significantly to that of MgH_2. XRD analysis of the electrode during the discharge showed that the reactivity of TiH_2 with Li ions cannot be described by a single reaction like for MgH_2, but it involves three different steps.

This work focuses on the diffusion coefficient of hydrogen into Ti as well as the permeation coefficient of TiO_2. Experimental investigations at 300 °C allow hydrogenation of Ti films of different thicknesses (50-800 nm). A way to directly see the phase growth/change and observe the formation process of the hydride is proposed here, similarly as in the Mg system. With the help of X-ray diffraction (XRD), cross sections by focused ion beam (FIB), scanning electron microscopy (SEM) and bright field transmission electron microscopy (TEM) as well as diffraction patterns, the mechanism of formation of TiH_2 is investigated. Quantitative measurements of the diffusion coefficient and a pressure dependency will be discussed.

4   METHODOLOGY

An experimental challenge of this work is the characterization of materials that have a very low atomic mass such as hydrogen, lithium and magnesium. Transmission electron microscopy (TEM) is one of the few techniques that allow imaging and diffraction analysis of the particles in parallel and, therefore, it becomes possible to identify their microstructure and their crystal structure. As a further complication, MgH_2 is unstable under the electron beam so that the direct identification of the hydride in the TEM was not possible, since it is easily oxidized during transport to the tool. This chapter describes the experimental procedure that was followed.

4.1   Sample preparation

Ion beam deposition is a physical vapor deposition (PVD) used for depositing thin films. It's a well-established technique for the creation of thin films of controlled thicknesses and smooth surfaces. The equipment used (Figure 4-1) was custom-made by Dr. Patrick Stender in 2005. The principle of deposition is explained hereafter and shown in more detail in Figure 4-2.
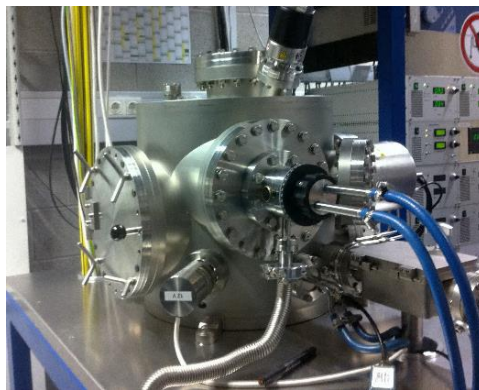
Figure 4-1: Ion beam sputtering system.

All samples were prepared by ion beam sputtering (IBS), a physical vapor deposition (PVD) technique. The apparatus consists of an UHV chamber with a residual gas pressure of $1 \cdot 10^{-8}$ mbar equipped with a *Veeco* DC 3 cm ion gun. The thin films are deposited using pure Ar gas that was ionized by a cathode made of a W-thoriumoxid filament. By applying a DC current of 2-3 A, the filament is heated and electrons start to emit. Between the cathode and a cylindrical wall (anode) a discharge voltage is applied, which causes acceleration of the electrons outwards. On their way to the anode, electrons ionize the Ar gas atoms by penning ionization. Therefore, positive ions are accelerated to the cathode. A conductive neutral plasma (of nearly equal numbers of electrons and ions) is formed. An acceleration system is also added, composed of two isolated carbon grids. The inner grid is on cathode potential and is used to focus the beam, while the ions passing are accelerated by the voltage applied to the outer grid.

Outside the gun, before reaching the target, the ions are neutralized by another W helical filament (38 turns), to prevent charging of the target surface. The energetic particles hit the target and, due to collisions, the target material is evaporated and deposited to the substrate.
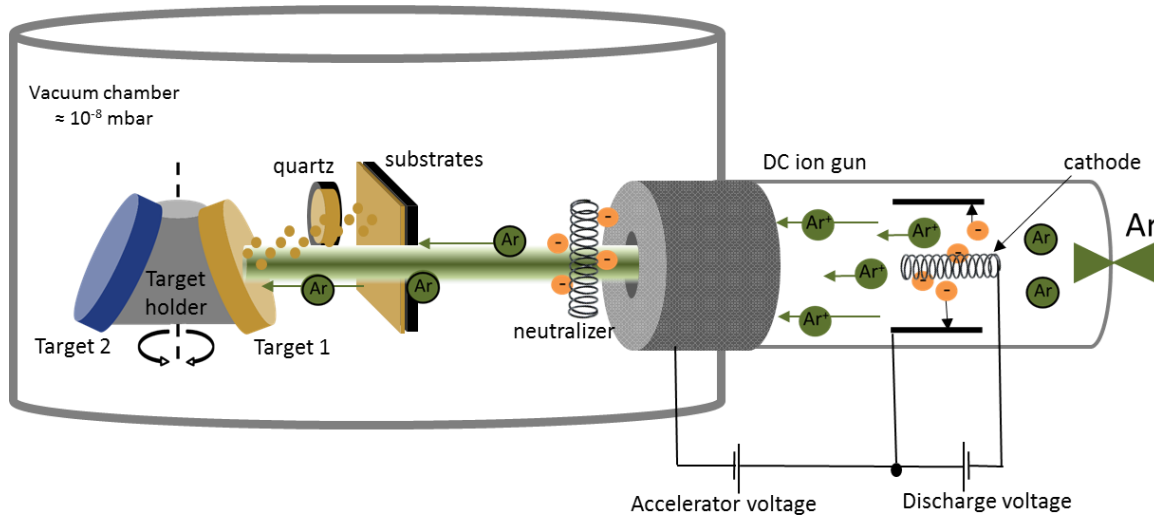
Figure 4-2: Scheme of the Ion beam sputtering chamber.

Constant parameters were used for all samples, in order to produce a set of well-defined layers. The selected sputtering conditions are shown in Table 5:

Table 5: Sputtering parameters during deposition of the thin films.

WORKING PRESSURE	$2 \cdot 10^{-4}$ mbar
BEAM VOLTAGE	600 V
BEAM CURRENT	20 mA
ACCELERATOR VOLTAGE	200 V

The thickness of the deposited films (5 – 1100 nm) was controlled via a crystal quartz microbalance (CQM) SQM -160 Rate/Thickness Monitor from Sigma Instruments, placed parallel to the substrates and was also confirmed by electron microscopy (SEM/TEM). The deposition rates were 1.2 Å/s for Mg, 0.6 Å/s for Ti and 0.8 Å/s for Pd.

Mg and Ti disks of 8 cm in diameter and 5 mm thickness, were used as targets, purchased from *Hauner-Metallische-Werkstoffe (HMW)* with a purity of 99.95%. A further Pd disk of the same dimensions was used, delivered by *Wieland Edelmetalle* with a purity of 99.95 %. All targets were cleaned by the ion beam inside the sputtering chamber for 15 min prior to deposition. Furthermore, the Mg target was stored in a desiccator under vacuum in order to avoid oxidation.

As a first step, the possibility of hydrogenating Mg directly by reactive ion beam sputtering (with hydrogen inside the chamber during Mg deposition) was investigated. Figure 4-3 shows a comparison of the expected hydrides vapor pressures, with the working pressure of different sputtering techniques. For ion beam sputtering, the working pressure is at 10^{-4} mbar. This is far below the partial pressure, at

which deposition of the hydride is possible at low temperatures. However, magnetron sputtering, which can operate at pressures up to 10^{-1} mbar, allows the direct formation of the hydride during sputtering. A magnetron chamber was custom made during this work and was therefore possible to produce the hydride in-situ during sputtering. Figure 4-4 shows the importance of high pressures for the hydride formation. After using a pressure of 10^{-2} mbar, the film was not pure, but traces of Mg were still found. Increasing the pressure to 10^{-1} mbar, formed a pure hydride film. However, the constructed magnetron chamber only allowed the deposition of one material at a time. So, it was not possible to protect the layer by Pd, before exposing it in air for further use. Since during this work, focus was given on the kinetics of hydrogen diffusion into the films, better control of the time, pressure and temperature were necessary. The samples were subsequently produced by ion beam sputter deposition in the pure metallic Mg or Ti form and ex-situ hydrogenated at high temperatures, as it will be discussed in further detail in the hydrogenation part of this chapter.
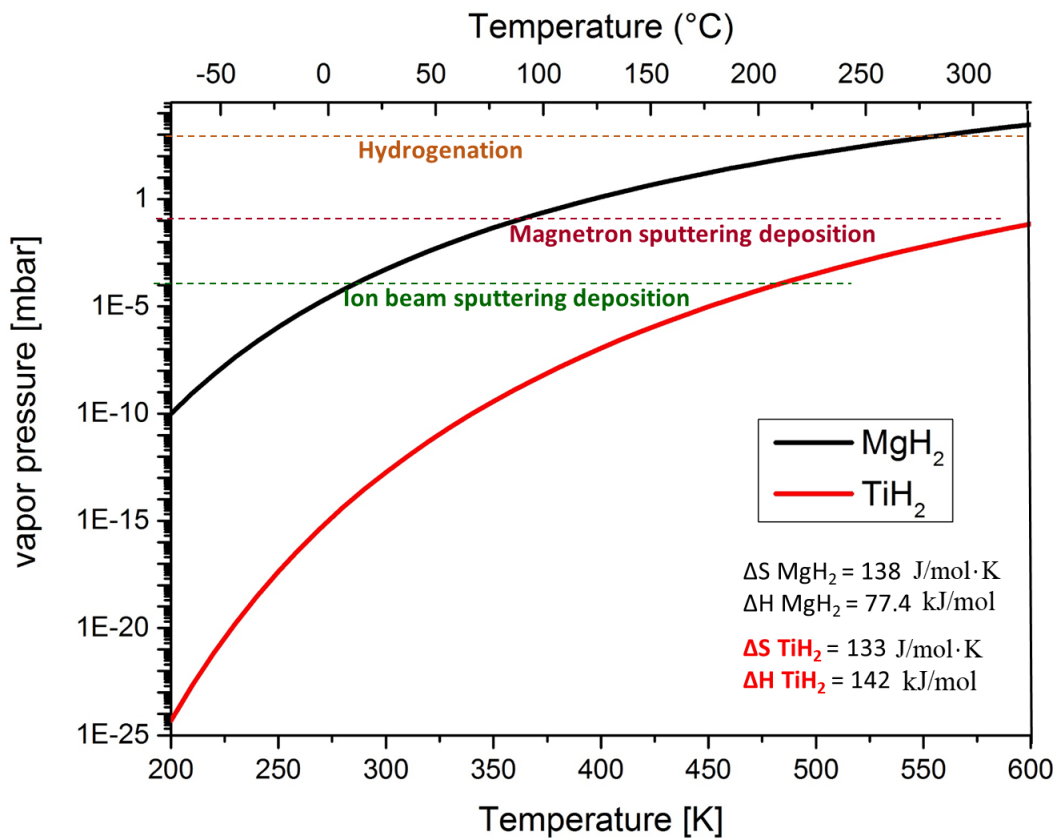
Figure 4-3: Vapor pressure of hydrides over temperature, showing the stability of the hydrides formation during the different available methods.

In the Mg-MgH$_2$ system, the samples were sputtered at room temperature on Si (100) oriented wafers (*from Siltronic AG*). The Si wafers were previously oxidized at 1100 °C for 3 hours under ambient atmosphere. The annealing time and temperature were chosen to obtain an amorphous SiO$_2$ thickness of about 200 nm, which has been shown to be stable in the later experiments. Pure Si wafers could not be used, since Mg-Si form intermetallic phases [Ok07] at the temperature of hydrogenation. Figure

4-5a) shows an example of the phases that are created with Mg/Si once the sample is heated up to 300 °C, if no oxide diffusion barrier layer is present. The use of the silicon oxide layer prevents the formation of these undesired silicates reliably.
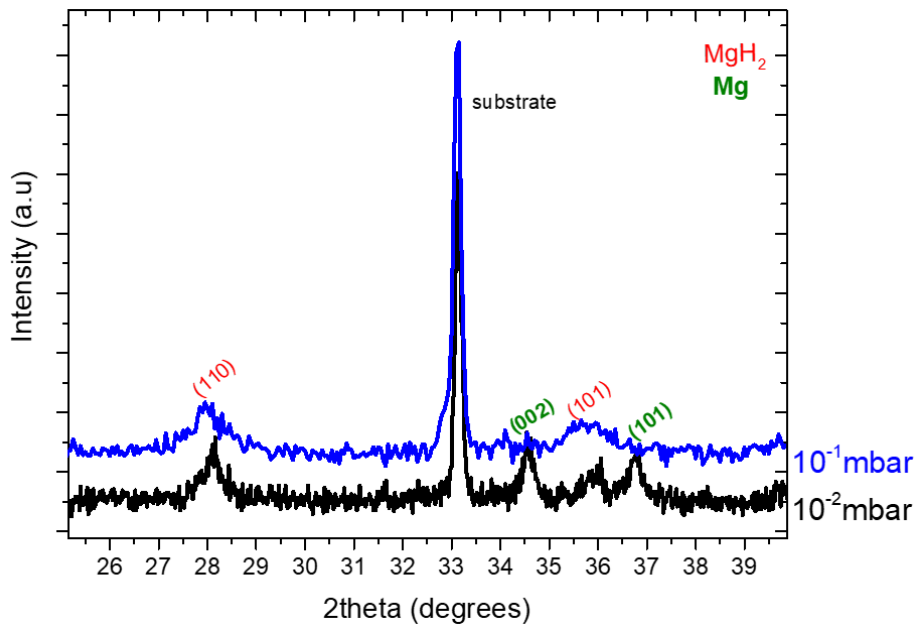
Figure 4-4: In-situ formation of MgH$_2$ by magnetron sputtering at two different hydrogen pressures, indicating that the pure hydride needs higher pressures in order to be formed.
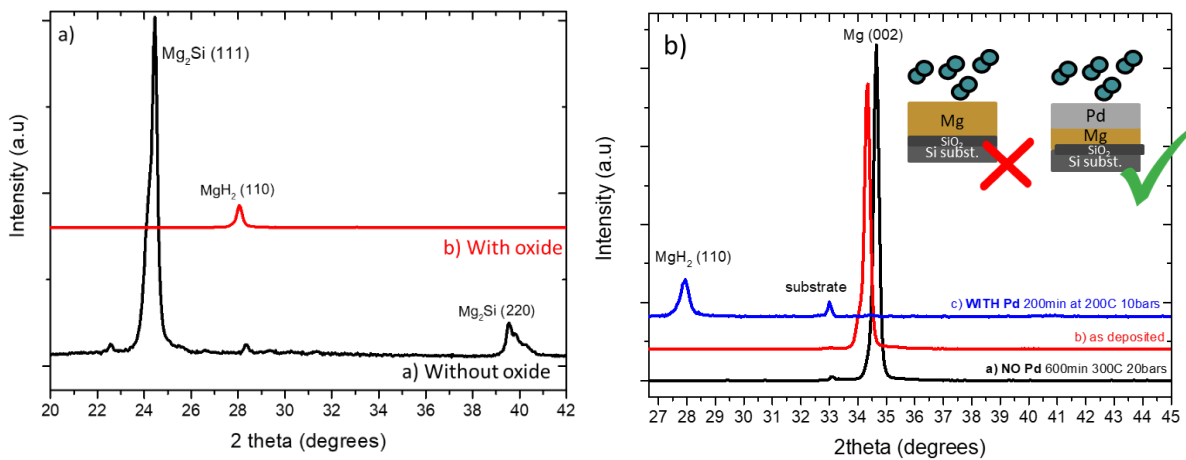
Figure 4-5: XRD diffractograms with Cu K$_\alpha$, of preliminary tests showing the choice of a) the substrate and b) the need of using Pd as catalyst for the Mg system.

Furthermore, different thicknesses of Pd (5 – 40 nm) were deposited on top of the Mg films, in order to protect them from any oxidation as well as for catalytic assistance in the hydrogenation. Different thicknesses were studied in order to see, whether the Pd thickness has any effect on the splitting of hydrogen molecules. Figure 4-5b) demonstrates the importance of using Pd as a catalyst on top of Mg layers. Samples without Pd could not be hydrogenated within a reasonable time. An attempt to hydrogenate a Mg sample without Pd layer on the surface, at a rather high H$_2$ pressure of 20 bar and 300 °C

was shown to be unsuccessful even after 600min. In contrast, coating with the Pd layer fully formed the hydride even at lower temperatures and within a shorter time.

For the studies on the Ti-TiH$_2$ system, three sets of samples were produced by IBS deposition: TiO$_2$/Ti thin films, Pd/Ti and Pd/TiO$_2$/Ti layers. Layers were deposited at room temperature on Si (111) substrates that were cleaned by the Ar beam before deposition. In order to identify the influence of the surface oxide on the Ti films, 5 nm of Pd were directly deposited on fresh Ti films. When the vacuum was kept in the chamber an oxide-free bilayer Pd/Ti was produced and with an intermediate venting of the chamber a triple layer Pd/TiO$_2$/Ti was obtained.

A sketch of all the prepared layer systems is presented in Figure 4-6.
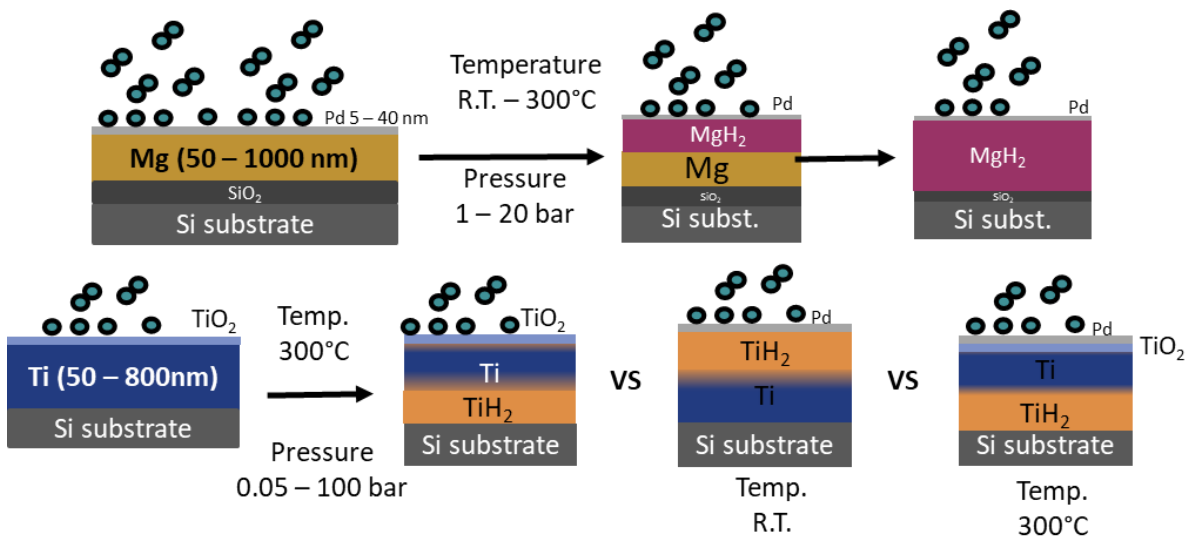
Figure 4-6: Sketch of the systems studied during this work showing the configuration of the layers investigated.

4.2 Hydrogenation

Hydrogenation of the samples was performed using a high pressure laboratory reactor *highpreactor*^{TM} *BR-300* from *Berghof* shown in Figure 4-7a) with a temperature controller and data logger. The experimental process of hydrogenation is illustrated in more detail in Figure 4-7b). The change of pressure and temperature over time is shown in order to describe the main steps of the experiments. The hydrogenation sequence takes place as follows: 1) pumping the reactor, 2) heating up to the required temperature while pumping continuously for removal of any impurities or oxides that might evaporate during heating up of the interior of the reactor, 3) insertion of pure H$_2$ (provided with a purity of 99.999 % H$_2$ by *Westfalen Gas*) and holding at these conditions for a specific duration, 4) pumping to remove H$_2$ atmosphere and finally 5) cooling down to room temperature under vacuum. This method assures that the time measured for full hydrogenation starts at the same moment for all samples, when hydrogen is inserted inside the reactor.

The experiments were carried out in the temperature range from room temperature up to 300 °C and pressures of 0.05 to 100 bar H_2 gas atmosphere for different durations. For each system, different temperatures and pressure were used. They are presented in more detail in the discussion part (chapters 5 and 6).
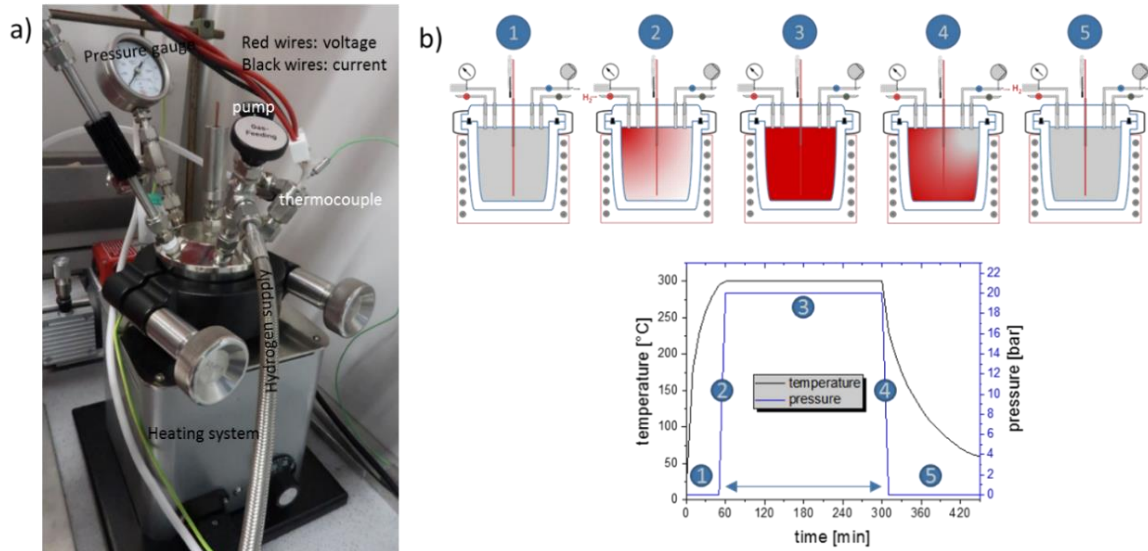
Figure 4-7: a) Hydrogenation reactor from outside and b) a sketch of the hydrogenation process, illustrating the change in pressure and temperature over time for each sample. 1) pumping the reactor, 2) heating up to the required temperature while continues pumping, 3) insertion of pure H_2, 4) hold at these conditions for a specific time and finally 5) cooling down to room temperature with no hydrogen inside the reactor

4.3 Resistance measurements

A convenient way of investigating the progress of hydrogenation in an Mg thin film is by observing the change in resistivity. Mg is a conductive metal, which upon hydrogenation converts into a less conductive hydride phase. The electronic structure of the hydride is non-metallic with the energy gap of ≈ 4 eV [NV15]. So, despite the volume changes during the transition from a metal to a semiconductor, a significant difference is expected to be observed in the resistivity as well. Not much has been reported in literature regarding the resistance change in this system. Therefore, focus was placed in investigating this resistance change upon the hydrogenation process during this work. This sub-chapter focuses on the theoretical background, necessary in understanding the change of resistance and how the thin film structure may affect this in addition.

When introducing hydrogen into Mg there is a small hybridization of the orbitals between the H and the Mg states in the valence bands, which have a dominant hydrogen character [Y.07]. The conduction bands have however mixed contributions from the hydrogens and the metal cations. Since the solubility of H in Mg is very low (to be at room temperature $c_H = 3 \cdot 10^{-7}$ H/Mg [SM87a]) the change in resistance at the beginning is very small. However, once the hydride starts to form, an increase in resistance is expected.

In 2005, Ingason et al. [IO05] investigated 100 nm Mg thin films with a thin Pd layer on the surface at different pressures in the range of 0-4 mbar and, with resistance isotherms, showed that the binding energy of the hydride is similar to the bulk. Through their isotherms, a weak increase of resistance is visible, when H is solved in the α-Mg phase, while a steep increase in resistance is observed when the hydride is formed.

Later, Özgit et al. [GAÖ13] studied the resistance change in Mg thin films, also with a thin Pd layer, under isochronal conditions between 60 °C and 120 °C with a constant pressure of 1 bar. In this way, it was shown that higher thicknesses need higher temperatures to fully hydrogenate within the same time. However, they have focused more on the texture change once hydrogenation took place.

During this work, Mg layers are covered with a Pd layer on the surface for reasons previously explained. Assuming a parallel layer structure and measurement in the plane directions, the structure of the layers is considered to give a total resistance according to a parallel circuit. So, the total resistance is given by:

$$\frac{1}{R_{total}} = \frac{1}{R_{Pd}} + \frac{1}{R_{MgH_2}} + \frac{1}{R_{Mg}} \tag{21}$$

Values of resistivity of each element, in bulk, are found in literature. Wagner et al. [WP11] studied in 2011 Pd hydrogenation and showed that the base resistivity of Pd is 100 Ohm·nm at room temperature. Mg is known to have a resistivity of 40 Ohm·nm at room temperature. Furthermore, the intermetallic phases formed between Mg and Pd appear to have a higher resistivity. With ρ_{MgPd3} = 180 Ohm·nm and ρ_{MgPd2} = 700 Ohm·nm
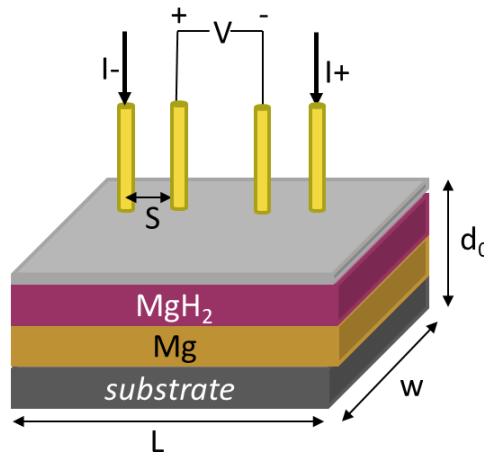
Figure 4-8: Schematic representation of sheet resistance measurements. Current is applied on the outer pins and voltage is read through the inside pins.

From the resistance measurements, the evaluation of the thickness of the hydride upon time can be estimated. Knowing the resistivity ρ , of a material, its resistance can be calculated as:

$$\rho = \frac{R \cdot A}{L} \rightarrow R = \frac{\rho \cdot L}{A} \tag{22}$$

where L is the length of the sample and A the area through which the current travels. Bearing in mind all the layers contributing to the total resistance, equation (22) becomes:

$$\frac{1}{R_{total}} = \frac{A_{Mg}(t)}{\rho_{Mg}L} + \frac{A_{MgH_2}(t)}{\rho_{MgH_2}L} + \frac{A_{Pd}(t)}{\rho_{Pd}L} \tag{23}$$

where A = d·w, with d and w the thickness and width of the respectively layer. Considering that the resistance of the Pd is negligible during the first cycle, equation (23) transforms to:

$$\frac{1}{R_{total}} = \frac{w}{L}\left(\frac{d_0 - d_{MgH_2}(t)}{\rho_{Mg}} + \frac{d_{MgH_2}(t)}{\rho_{MgH_2}}\right) \tag{24}$$

where $d_{Mg}(t) = d_0 - d_{MgH_2}(t)$ (while the hydride is growing in the film, the Mg metal layer is decreasing accordingly). Solving equation (24) for $d_{MgH_2}(t)$ the hydrogenation thickness is experimentally obtained from the measured resistance:

$$d_{MgH_2}(t) = \frac{\rho_{Mg} \cdot \rho_{MgH_2} \cdot L - w \cdot \rho_{MgH_2} \cdot d_0 \cdot R(t)}{\rho_{Mg} \cdot w \cdot R(t) - w \cdot \rho_{MgH_2} \cdot R(t)} \tag{25}$$

This formula is used later to estimate the remaining hydride in the layer during dehydrogenation.

The resistance discussed so far is usually calculated by using Ohm's law where R = U/I. However, in the case of thin films, that are nominally uniform in thickness, it makes more sense to discuss the sheet resistance as a materials property. Using therefore: $R_{sheet} = (U/I) \cdot (\pi/\ln2)$. This presumes preconditions for the distance between the contact points. Figure 4-8 shows a schematic representation of the current flow in the samples. It is important to note, that the spacing between the pins is constant and that the film thickness has to be less than 40 % of this spacing. The change in the final end is only a factor of $(\pi/\ln2)$ [Sm58]. However, in a four-point probe measurement, where current is passing through the outside two contacts, and the voltage is measured across the inner two contacts, it is more scientifically correct to consider the sheet resistance.

Resistance measurements were carried out in a custom made setup. This setup is using the same "reactor chamber" as for the hydrogenation measurements and allows recording in-situ resistance measurements while hydrogenation and de/re-hydrogenation take place. These experiments were performed only for the Mg system for which the resistance change upon hydrogenation is remarkable. The device is used at the same conditions as in the before mentioned hydrogenation treatments between room temperature and 200 °C and 20 bar. An image of the setup is presented in Figure 4-9. It is composed of the main chamber, which contains a heating plate. The sample holder is composed of four spring-loaded gold plated pins mounted at room temperature delivered by *Feinmetall contact technologies.* The outer pins of the sample (I_A and I_B) are connected to a DC Current source (*6181C HP – Hewlett Packard*) and 1 mA is applied. A *Rohde and Scharz HAMEG Digital* multimeter is used for measuring the corresponding voltage contacted at the inside pins (V_A and V_B). This way, a four-point

probe resistance measurement was realized according to the configuration sketch in Figure 4-9, where I is the applied current and V the recorded voltage. Samples were heated to 200 °C under controlled conditions and the temperature was measured using a K-type thermocouple, connected to and controlled by the *Berghof* electronics.
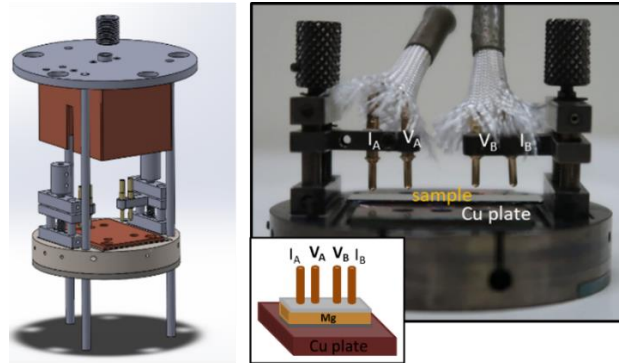
Figure 4-9: Resistance measurement setup. Sketch and photo of the sample holder.

4.4   X-Ray Diffraction

X-ray diffraction (XRD) is a non-destructive analysis technique frequently used in material sciences to determine the crystal structure and texture of a sample. X-rays are scattered elastically on the periodic crystal lattice, which results in a material specific diffractogram. Analysis of the reflection peaks is based on Bragg's law.

4.4.1   XRD - Ex-situ Measurements

Lattice structure and properties of hydrogenation of the specimens were investigated by a *D5000 X-Ray Diffractometer* from *Siemens (*Figure 4-10)*, with* Cu K_{α}-radiation. The characteristic peaks of the hydrides and the pure metals are recorded. For a more accurate determination of the peak position, the measured intensity profiles were fitted with a Lorentz function with the Program QtiPlot 0.9.8 from Ion Vasilief.
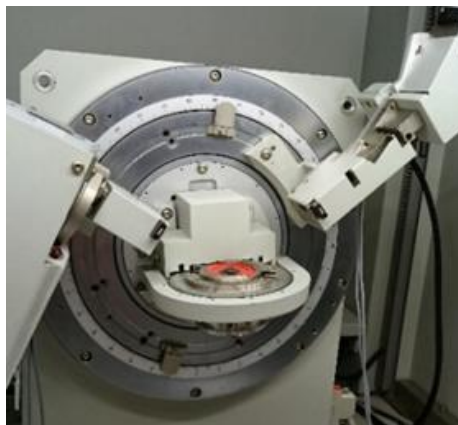
Figure 4-10: XRD Diffractometer D5000 - from IMW – Stuttgart department

4.4.2   XRD - In-situ Measurements

Some samples of the Mg system were further characterized by in-situ measurements in collaboration with the group of Prof. Orimo at the University of Tohoku, Japan. Dr. Sato helped with these measurements, for which a *PANalytical X'PERT* (Figure 4-11), with Cu Kα radiation, wavelength λ = 1.5406 Å for $K_{\alpha1}$ and 1.5444 Å for $K_{\alpha2}$, was used. Samples were placed in a reactor chamber (Anton Paar XRK 900) and hydrogenated at 5 bar of H_2 pressure, while heated up to 150 °C from room temperature with a heating rate of 5 °C/min. The X-ray diffractograms from 2θ = 20 ° to 60 ° were obtained over a 10 min measurement at 25 °C and, subsequently at stepwise increased temperatures from 50 to 150 °C in 10 °C intervals. At 150 °C and 5 bar a further isothermal measurement was performed for 60 min in order to attain a fully hydrogenated sample. This temperature was chosen so that the half hydrogenation of 400 nm samples is clearly visible by XRD and focus on the peak shift was given. The results are discussed in detail in chapter 5.1.1.

Figure 4-11: Diffractometer PANalytical X'PERT – from Prof. Orimo's lab.

4.5   Electron microscopy (SEM/FIB and TEM)

In order to investigate the samples microstructure high resolution transmission electron microscopy (TEM) was employed. A *Philips CM200-FEG* (Figure 4-12) was used at 200 kV for imaging as well as electron diffractometry.

Figure 4-12: TEM Philips CM200 FEG.

In TEM, a high energetic electron beam irradiates a thin film sample to provide detailed information about the structure or chemistry of the specimen. The beam, however, can cause permanent, un-wanted changes to the electron transparent thin films. Many hydrides decompose fast upon irradiation with the electron beam. This has already been reported for $LiBH_4$, LiH, AlH_3, $LiAlH_3$, $NaBH_4$, $NaAlH_4$. Recent work on MgH_2 [SSR17] shows also the instability of the hydride investigated during this work. Transparent thin films for TEM observations were prepared for cross-sectional imaging by means of a FIB (SCIOS-FEI dual beam - Figure 4-13). Scanning electron microscopy (SEM) as well as the energy dispersive x-ray (EDX) characterization was performed at 5kV.

The preparation takes place in four main steps. The micrographs obtained by the SEM illustrate these steps in Figure 4-14. First step (Figure 4-14a)) is the deposition of the Pt protective layer of 1.5 μm on the surface of the sample in order to reduce the damage of the area of interest during the preparation. This layer is deposited by a gas injection system (GIS). It is designated as "protective layer" throughout this work. Once the Pt is deposited, two parallel squares are milled on top and bottom of this area (Figure 4-14b), using focused ions accelerated with a voltage of 30 kV and 65 nA. In this way, a lamella is created and is ready to be extracted. The third step is called the "lift-out", Figure 4-14c) and shows the extracted piece of the material mounted on a needle called the micromanipulator. Using the micromanipulator, the lamella is transported to a Cu grid (Figure 4-14d-e), which is fixed by gluing with Pt.

Figure 4-13: SCIOS Duel beam (SEM/FIB).

The fourth step consists of thinning the lamella progressively until it reaches a thickness that makes the sample electron transparent (Figure 4-14f-g)). This is succeeded by using different ion currents 1 nA, 300 pA and 100 pA until a thickness lower than 100 nm is achieved. The final step of the preparation of the samples consists of "cleaning" the surface of the lamella by the ion gun. The use of the FIB

introduces the implantation of gallium ions and/or amorphization of the surface of the sample. In order to minimize this damaged layer on the surface, the use of low acceleration voltages (5-2 kV) is necessary. These ions are rather slow, so that they allow a gentle polish of the sample by removing only the surface layer that has previously been damaged.
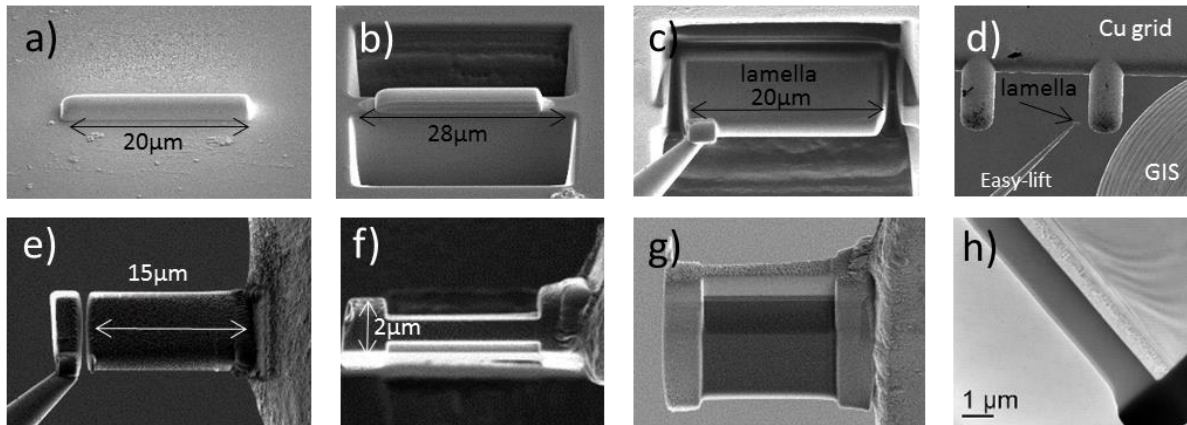
Figure 4-14: Steps of TEM lamella preparation out of thin film sample, with the FIB-SCIOS dual beam: a) the protective layer of Pt using the GIS is deposited in a length of 20 µm, b) cuts to free the layer of interest, c) the free lamella is ready to be moved, d) the lamella is glued to the Cu TEM grid with the help of the easy lift and the GIS, e) the micromanipulator (easy-lift) is removed, f) the lamella is thinned while controlling its thickness, g) when tranparency is shown in the electron image, h) the layer is thin enough for imaging in the TEM where a higher resolution can be obtained.

To perform the subsequent analysis by TEM, the samples are transported from the FIB to the TEM in contact to air. An inconvenience, unfortunately unavoidable with the available equipment.

4.5.1   Grain size analysis

Analysis of the grain size was completed for both systems in order to confirm that investigations during this work are done on nanostructured crystalline thin films. Figure 4-15 shows the bright and dark field TEM images of both systems. For a first orientation, 20 nm of the metal was deposited on a C coated Cu grid. This is giving an overview of the grain size of the samples. However, the actual grain size might differ since the deposition of these layers is done on a different substrate, which may affect the size of the grains. Image-J was used to analyze the grain size and the distribution was fitted with a Gaussian fit.

In the case of Mg, an average of 17.3 ± 7.6 nm in grain diameter was obtained. The grain distribution is shown in Figure 4-15c). In the case of Ti, an average of 4.3 ± 2.3 nm diameter was obtained. The corresponding grain distribution is shown in Figure 4-15f) and the rather large error is attributed to the precision of the image threshold chosen with the software. Because of the very small grain size and the artificial carbon substrate, further analysis was done by XRD at thin films of different thicknesses

deposited on oxidized Si (in the case of Mg). The grain size can be calculated using the Scherrer-equation:

$$L = \frac{\lambda \times K}{w \times \cos\vartheta} \tag{26}$$

where L represents the size of crystalline domains perpendicular to the surface, K the Scherrer shape factor and w the broadening of the measured peak (full width at half maximum in 2θ in radians). For the shape factor, a value of $K \approx 0.9$ was used, valid for approximately spherical grains [J.78]. This way an average grain diameter of 16 ± 0.5 nm was obtained for Mg and 4 ± 0.5 nm for Ti.
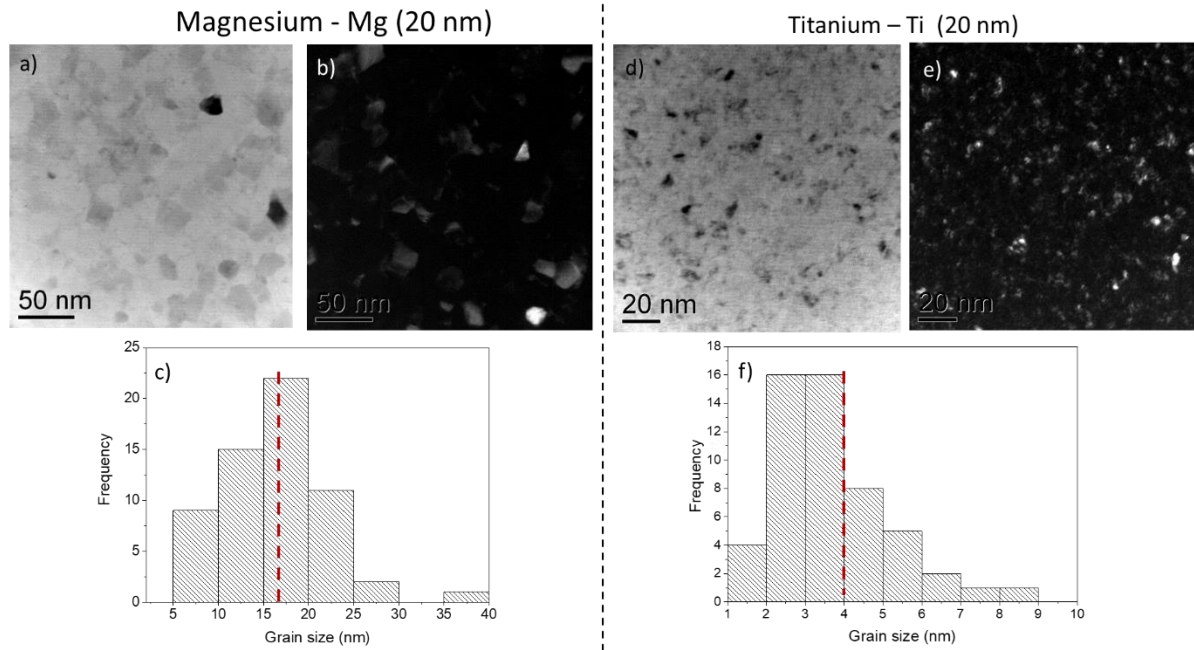
Figure 4-15: Grain analysis of both metalic films: a) Bright field image and b) dark field image of 20 nm Mg deposited on a carbon film c) Grain diameter analysis from the TEM images of Mg showing an average grain diameter of 17.27 nm marked with dashed line d) Bright field and e) dark field of Ti 20 nm deposited on a carbon film f) grain diameter distribution of Ti recording an average size of 4.15 nm marked with dashed line.

From this analysis, it is clear that the films grains in the range of 5-20 nm in diameter. Furthermore, Ti has the tendency to form smaller grains than Mg during ion beam sputter deposition.

Additionally, the lattice parameter of the as-deposited samples was calculated in order to see whether there is any systematic change with a variation of the thickness. The d-spacing was determined based on Bragg's law and consequently the crystal geometry and the Miller indices of the peak are used in order to calculate the lattice parameter. Since the lattice structure is hcp in both cases the appropriate equation is:

$$n\lambda = 2d_{hkl}\sin\theta \ \ \text{and for \underline{hcp:}} \ \frac{1}{d_{hkl}^2} = \frac{4}{3}\left(\frac{h^2 + hk + k^2}{a^2}\right) + \frac{l^2}{c^2} \tag{27}$$

in which θ represents the measured angle by the XRD characterization, h, k, l are the Miller-indices of the respective peak, a and c are the lattice parameters and λ the wavelength of the x-rays (Cu Ka λ = 0.15418 nm). d_{hkl} represents the distance between the planes. This XRD characterization focuses on

the (002) and the (100) peaks (depending on the thickness). Figure 4-16 shows the calculated lattice parameters versus deposited thickness for both systems, showing the constant lattice parameter at all thicknesses of film deposition.

$$\text{For } \underline{\text{hcp (002)}}\ c = \lambda \sin \vartheta^{-1} \text{ and } \underline{\text{for hcp (100)}}\ a = \lambda \left(\sqrt{3} \sin \theta \right)^{-1} \tag{28}$$
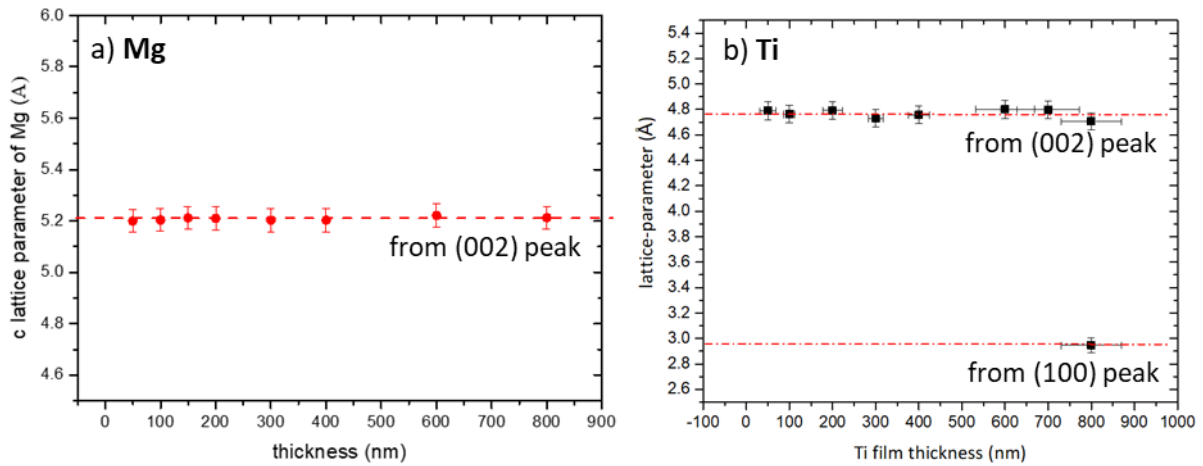
Figure 4-16: Calculated lattice paterameters versus thickness of the deposited films. Values obtained by XRD characterization data. Red dashed line represents the literature values for a) Mg system b) Ti system.

4.5.2   HRTEM Image analysis

In high resolution TEM (HRTEM) micrographs shown in the later chapters, analysis of the lattice fringes observed was done in order to identify the phases. Here an example of the analysis is presented, taken the example of Pd. Later the Pd layer is often seen as a black/ dark layer. This is due to its high density and high electron order number. However, when thinning the material to few nm (with the FIB), it is possible to observe the lattice planes in HRTEM, which allows to evaluate, whether the sputtered layer is pure Pd. It is important to mention that good thinning of the TEM lamellas and detailed preparation of the sample are essential for the HRTEM analysis.

From the HRTEM images obtained and shown in Figure 4-17, one can use the Fast Fourier Transformation (FFT). Whereas FFT is often used for focusing during the experimental imaging, it can also yield important information after the images have been obtained. The image transformation decomposes the image into its sine and cosine components. The output represents a frequency domain, whereas the image observed directly in the TEM represents the spatial domain. Each point, therefore, represents a particular frequency contained in the spatial domain image. In microscopy, this effect is essential, since one can identify the crystalline nature of a material localized in very small regions. In other words, it gives information on the reciprocal space of the selected region.

Regarding Figure 4-17, each dot from the FFT in b) (reciprocal pattern) shows a periodicity in the direct image in Figure 4-17a). This can help obtain a clearer image and observe the lines of the planes more

clearly, when removing the background information of the image.

In order to do this, Figure 4-17 shows the performed image processing. The same process is followed for all HRTEM images referred in chapter 5.1.3. By selecting the dots seen in the FFT, which represent the crystalline material and inversing them into an image, a "Fourier filtered image" is obtained, where the lattice fringes are more clearly seen and the contrast gives a better precision to the evaluated lattice spacing.
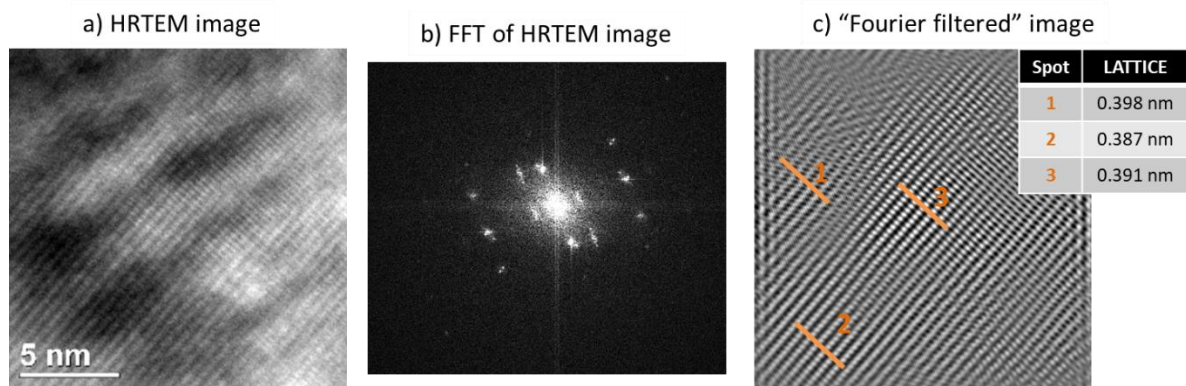
Figure 4-17: HRTEM analysis method a) HRTEM image obtained, b) FFT transformation of image a), c) "Fourier-filtered" image from inversing the FFT after only the dots of the FFT have been selected.

5 MAGNESIUM SYSTEM

In the following chapter, the quantitative analysis of the hydrogen sorption kinetics of the Mg/MgH$_2$ system will be presented. With the XRD in-situ characterization, the hydrogenation process is first followed. TEM imaging confirms three important stages, the as-deposited, the partially hydrogenated and the fully hydrogenated samples. The kinetics is studied at different temperatures, from room temperature to 300 °C, so that the characteristic Arrhenius plot can be given for the first time. More precisely, the nature of the hydrogen transport, during the first hydrogenation, is studied in detail at 200 °C (10 bar and 20 bar) and 300 °C (20 bar) by ex-situ XRD measurements and a quantitative calculation of the diffusion coefficients is given. Additional characterization by electrical resistance measurements allows studying the growth of the hydride at various different temperatures. Dehydrogenation as well as subsequent re-hydrogenation at 200 °C and 300 °C will also be characterized by XRD, resistance measurements and TEM. The latter especially demonstrates the creation of Mg-Pd alloys supported by EDX measurements. Its stability and effect to the cyclability of the material will be discussed. Table 6 summarizes the important parameters and the techniques used in each sub-chapter.

Table 6: Samples and parameters summary for each sub-chapter.

	CHAPTER	Mg LAYER (nm)	Pd LAYER (nm)	PRESSURE (bar)	TEMP. (°C)	TIME (min)	TECHNIQUES
HYDROGENATION	**5.1**	400	20	5	**150**		In-situ XRD/TEM
	5.2	50 - 800	5 - 40	10 / 20	**200**	10 - 400	Ex-situ XRD
	5.2	50 - 1100	20	20	**300**	60	Ex-situ XRD
	5.2	80 - 1100	5 - 40	20	**R.T. - 200**	10 - 7200	Resistance
DE/RE-HYDROG.	**5.3**	**MgH$_2$** 600	(initial) 20	**Vacuum 20**	200	≈ 300	Ex-situ XRD/ Resistance/TEM

5.1 Hydrogen sorption (1st hydrogenation)

5.1.1 Overview characterization of the hydrogenation process
(Collaboration with Tohoku University)

In the first part of this chapter, the hydrogen sorption kinetics of pure Mg layers under hydrogen atmosphere is studied. The samples are covered with a Pd layer as previously described, in order to avoid

any oxidation of Mg during transport and to accelerate the dissociation of hydrogen molecules on the surface. Only single hydrogen atoms migrate into the metal. Part of this sub-chapter has been already reported in the publication by Hadjixenophontos et al. [Ha17].

In order to estimate the time needed for full hydrogenation of different Mg thicknesses, the samples were tested first in incremental time steps. Figure 5-1 shows the XRD diffractograms of 400 nm Mg layers at different stages. In a) (blue), the as-deposited state is shown with a fiber texture along the (002) plane at $2\theta = 34.348\,° \pm 0.02\,°$, which is the energetically or kinetically preferred orientation for a hcp structured material during deposition [Sc98]. At 200 °C (100 min / 20 bar), the formation of MgH_2 is observed by a peak at $2\theta = 27.947\,° \pm 0.02\,°$ which represents the (110) plane of the hydride, shown in the red (b) partially hydrogenated sample). Increasing the time at 200 °C (250 min / 20 bar), full hydrogenation is taking place and more orientations of the hydride become visible, at $2\theta = 57.756\,° \pm 0.03\,°$ and $2\theta = 35.744\,° \pm 0.02\,°$ for the orientations (220) and (101), respectively. The fully hydrogenated sample is visible in Figure 5-1c) (black).
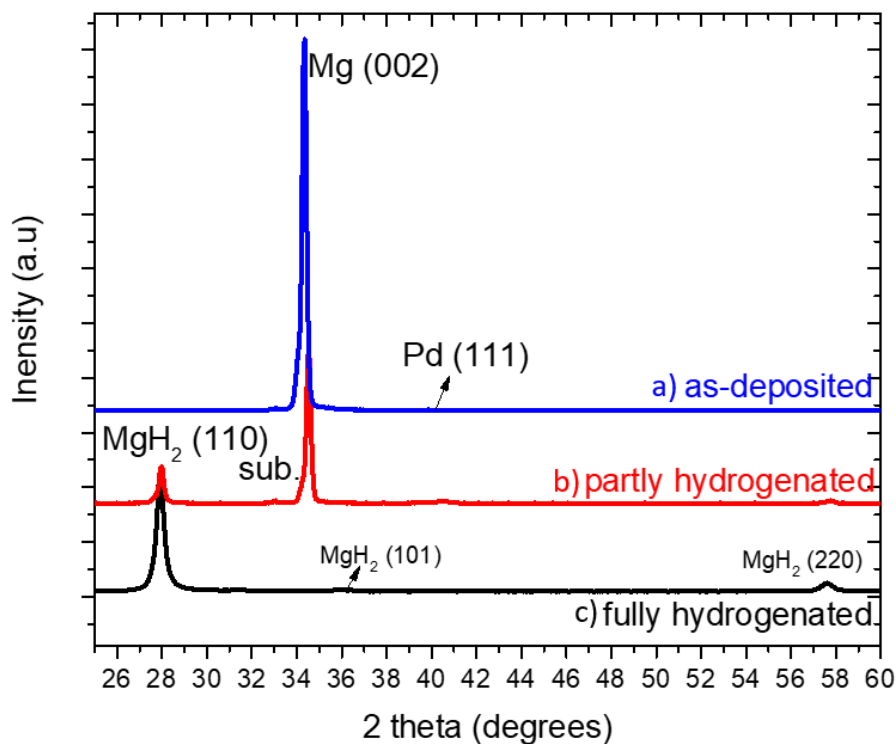
Figure 5-1: X-ray-diffraction diffractograms of three samples of Mg, 400 nm in thickness coated with Pd 20 nm, investigated at different hydrogenation steps: a) as-deposited Mg, b) partially hydrogenated sample (100 min at 200 °C / 20 bar) and c) fully hydrogenated for 250 min at 200 °C and 20 bar.

Evaluating the XRD diffractograms, the intensity of the Mg peak seems to be much higher than the intensity of the final MgH_2 layer of same thickness. This is however no surprise since the scattering factor of hydrogen is very low as the element is so light. For a clear comparison and to ensure the purity of MgH_2 thin films, a comparison was done with a MgH_2 powder sample. Figure 5-2 shows that

the peak position of the thin films are comparable to the one of powders, besides the fact that a strong texture is present in the thin films along the (110) direction of the tetragonal MgH_2 phase.
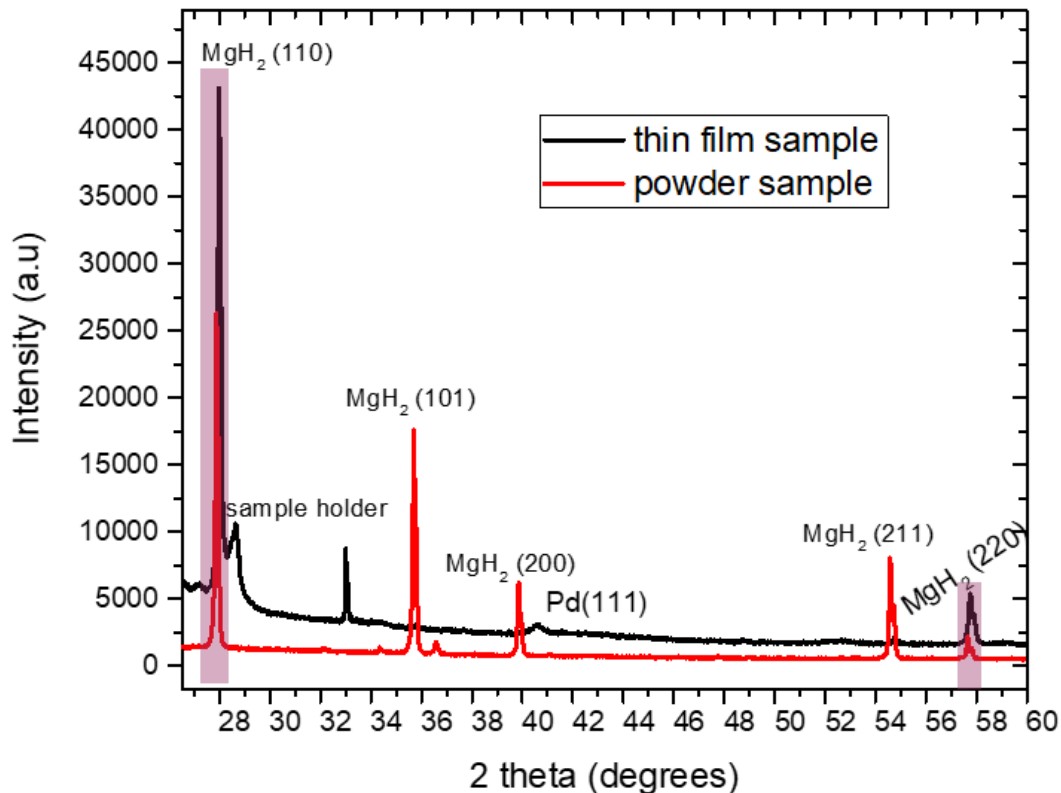
Figure 5-2: X-ray-diffraction patterns for a comparison of the intensities between powder and thin films of magnesium hydride. A powder sample of MgH_2 (red) with multiple reflections visible, compared with a thin film (black) where the reflections have a preferred orientation along (110) direction. Peaks from the sample holder are also visible when measuring thin films.

The Mg (002) peak in Figure 5-1a) and b), is only weakly shifting from lower angles to higher angles from the as-deposited to the partially hydrogenated sample. Further in-situ x-ray diffraction experiments were performed in order to observe the hydrogenation of 400 nm Mg thin films during isothermal treatment in more detail. In Figure 5-3, the shift of the peaks is better observed by the in-situ characterization of the sample, while heating up from room temperature to 150 °C. Significant is the Mg (002) peak (see Figure 5-3b), that shifts from $2\theta = 34.516$ ° at room temperature to $2\theta = 34.41$ ° at 100 °C, where it then stays constant while decreasing its intensity over hydrogenation (see Figure 5-3b'). This shows that the c lattice parameter expands from 5.196 Å to 5.211 Å, since the film is attached to the substrate and the perpendicular direction to the substrate has a higher possibility to change. Although the Mg peak does not shift anymore above 100 °C, the Bragg peak positions of the hydride (110) shift to lower angles (see Figure 5-3a'), probably due to thermal expansion. D. Moser et al. have reported volume expansion during hydrogenation and dehydrogenation reactions of powder MgH_2 as a function of temperature [Da09]. The volume expansion can be roughly calculated from the volume ratio of the unit cells. Since Mg has a hcp structure and the hydride has a tetragonal structure

the volume of the unit cells can be calculated by: $V_{Mg} = a^2_{Mg} c_{Mg} \sin\frac{\pi}{3}$, $V_{MgH_2} = a^2_{MgH_2} c_{MgH_2}$. With

$c_{Mg} = 5.19\,\text{Å}$, $a_{Mg} = 3.20\,\text{Å}$, $c_{MgH_2} = 3.01\,\text{Å}$ and $a_{MgH_2} = 4.50\,\text{Å}$ the volume ratio $\frac{V_{MgH_2}}{V_{Mg}} = \frac{60.95}{46.02} = 1.32$.
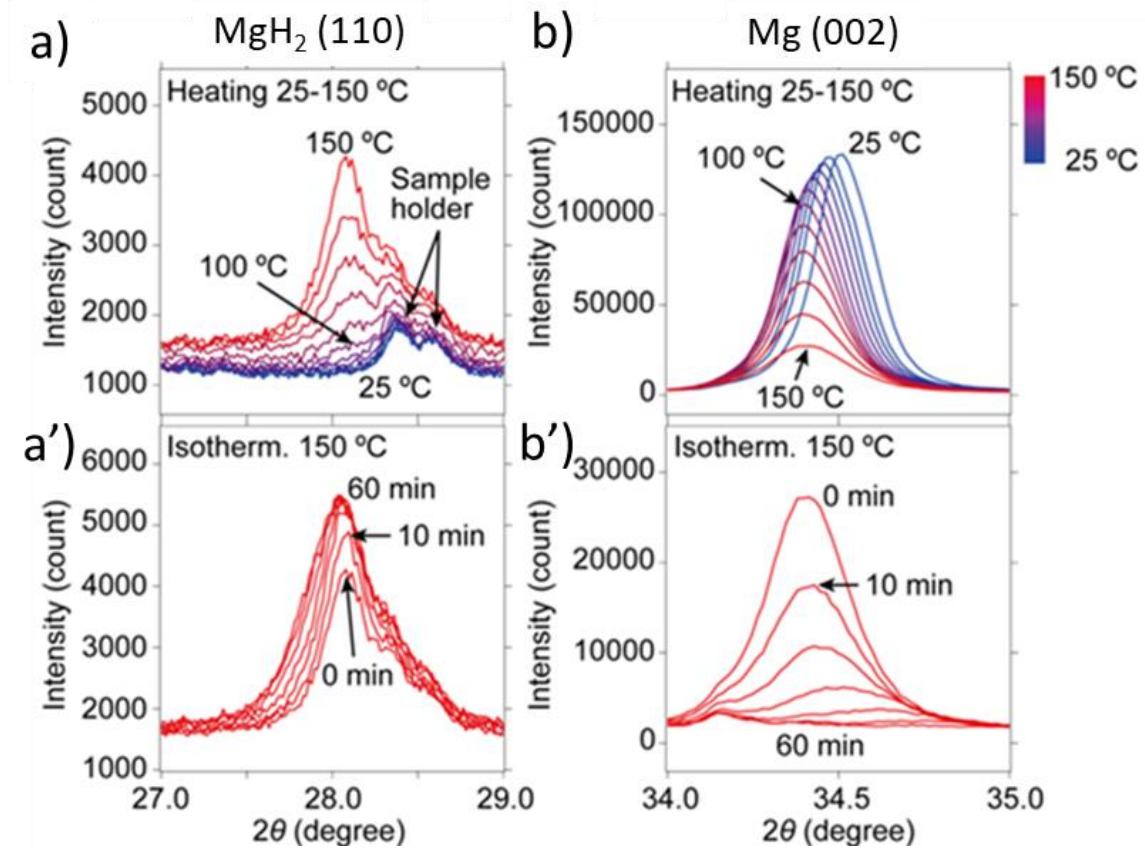
Figure 5-3: In-situ characterization of a Mg film heated from room temperature to 150 °C. XRD data recorded every 10 °C showing the peak shift during hydrogenation a) and b) during heating up, a') and b') during isothermal measurements at 150 °C [Ha17].

TEM observations of this study, that will be further discussed later, allow the statement that MgH₂ forms as a layer from the surface of the Mg towards the substrate. This, however, explains the Bragg peak of Mg (002) above 100 °C, which is observed near the substrate. The thermal expansion of the thin film can be assessed by simple calculations of the thermal expansion coefficient of bulk Mg (α = 0.000025 m/m°K). This estimation shows that the expansion of the c lattice parameter of Mg caused by thermal expansion should bring the lattice up to 5.26 Å. This is more clearly shown in Figure 5-4a), where the theoretical increase is shown by the dashed line. Therefore, it is assumed that the un-shifted Bragg peak of Mg (002) above 100 °C is related to compressive stress coming from the MgH₂ phase, which overlays the expansion of the Mg lattice as shown by the arrows in Figure 5-4a). If the hydride is not formed, the lattice should theoretically continue expanding as shown with the dashed line. However, the Bragg peak position of Mg (002) shifts even to higher angles in the first 10 min of isothermal annealing at 150 °C with increasing fraction of MgH₂, which corresponds to a shrinkage of the lattice along the c- axis as shown in Figure 5-4b). This can only be due to the phase transformation of Mg to

MgH$_2$, which is even further confirmed, since the thin film is attached to the substrate and a thermal expansion along the c-axis should be even more pronounced.

Any variation in temperature can give rise to stress-free variations in the lattice spacing. Consequently, while keeping in mind that the solubility of hydrogen in Mg is very low and thus cannot cause such expansion, it can be concluded that the initial change in Mg lattice is caused by thermal expansion. Once the hydride starts to form, the expansion initially stops and later a decrease of the Mg lattice is even observed, since the expanding hydride lattice provokes compressive stresses to the Mg.
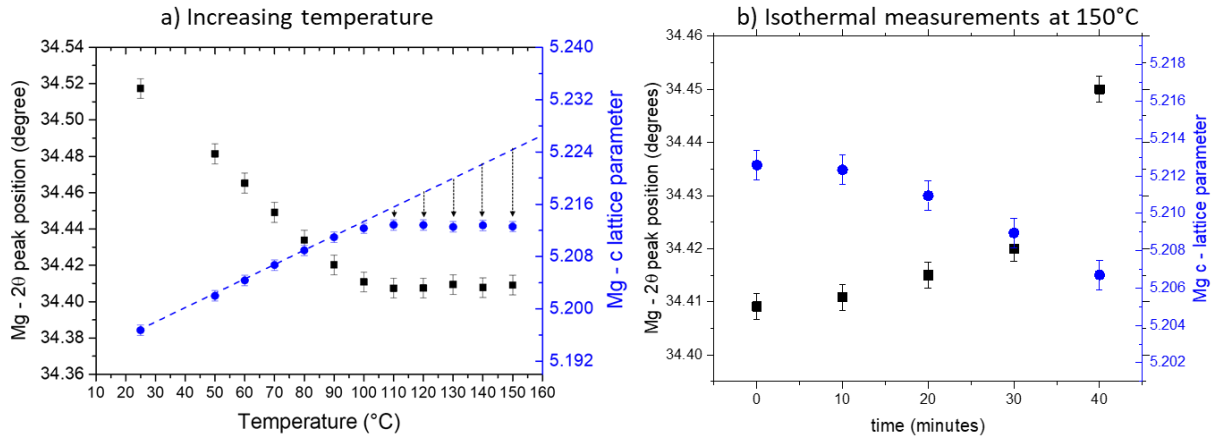
Figure 5-4: Mg 2θ peak position and c lattice parameter calculated upon a) increasing temperature b) isothermal measurements at 150 °C.

From the peak shift observed in the XRD diffractograms, the in-plane mechanical stresses σ, occurring from the hydrogen absorption, can be evaluated when using the Freund and Suresh formula [L.09] for biaxial stress:

$$\sigma = -\frac{E_{Mg}}{1-v_{Mg}}(\frac{d_{\sigma}^{\alpha}(T)-d_0^{\alpha}(T)}{d_0^{\alpha}(T)}) \tag{29}$$

where E$_{Mg}$ is Young's modulus of Mg (for bulk Mg E$_{Mg}$ = 45 GPa [Uc15]), v$_{Mg}$, the Poisson ration of Mg (equal to 0.35 [Uc15]) and d_0^{α} (equal to 2.598) and d_{σ}^{α} are the lattice spacing of α-Mg phase obtained from the (002) plane with and without stress σ respectively. Using equation (29), a simple prediction of the compressive stress value caused by the hydride formation starting from 100 °C is given in Figure 5-5. As previously indicated, the peak position shifts to higher angles while increasing the temperature, showing that the film increases its compressive biaxial stress while heating, probably due to the formation of the hydride.
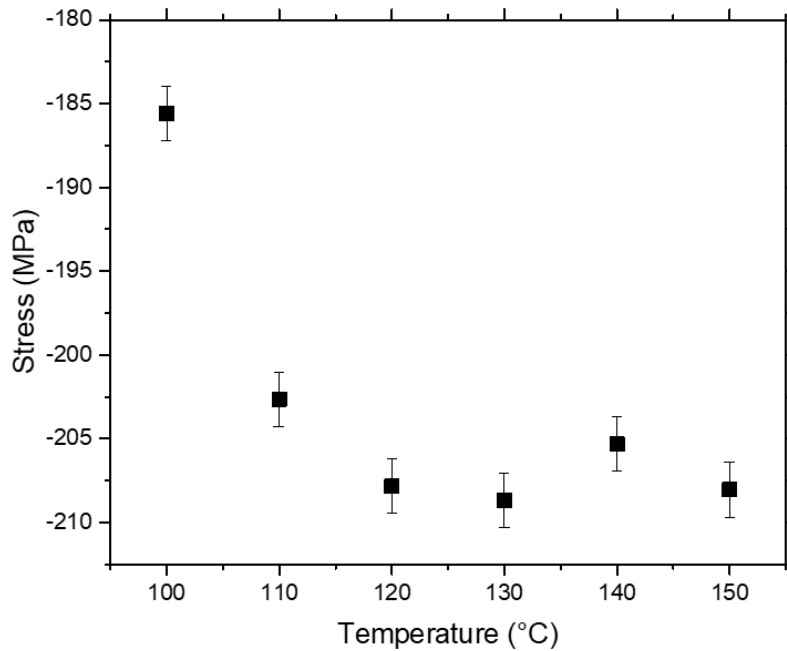
Figure 5-5: Compressive stresses caused by the hydride phase starting at 100 °C.

At 5 bar of hydrogen and 150 °C, full hydrogenation is observed since there is no Mg peak visible anymore in the XRD (blue graph in Figure 5-1). Furthermore, the Pd peak is no longer observed over full hydrogenation, indicating that Mg-Pd phases can be formed at these conditions according to the phase diagram shown in Figure 3-5. This is further investigated later and discussed in more detail in the desorption chapter of this work. The nanocrystallinity of the intermetallic reaction products seems to be the reason why no corresponding new peaks become visible in the diffractograms during the first hydrogenation.

5.1.2 Microstructure transformations

Physical vapor deposition techniques may produce different microstructures depending on the deposition parameters. Using ion beam sputtering deposition, very smooth and defined structures allow the investigation of the atomic transport of materials. These smooth layers are first confirmed by SEM and are demonstrated in Figure 5-6. In order to witness the change in the Mg thin film by hydrogenation, SEM characterization was conducted on the three samples previously described in Figure 5-1. Figure 5-6 shows the cross sections of the three samples at different stages. EDX analysis was performed on the as-deposited sample to verify the purity of the elements present inside the film. Carbon (C), platinum (Pt) and gallium (Ga) stem from the FIB sample preparation, for which a protective layer is deposited on top of the region of interest. Pd is observed to be on the surface of the layer as expected

and Mg represents the main part of the film with a thickness, in this case, of 400 nm. SiO_2 appears to be 200 nm thick and the pure Si of the substrate is observed at the bottom.
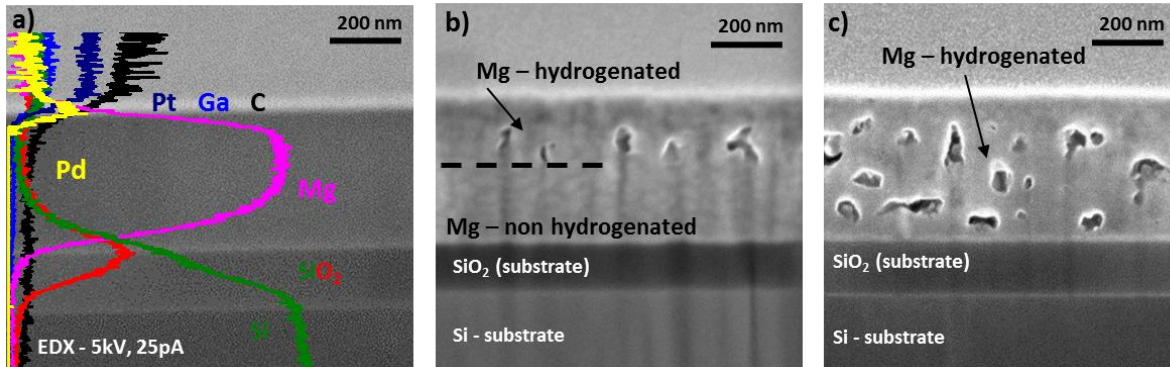
Figure 5-6: Cross sectional SEM images of thin films: a) as-deposited smooth 400 nm Mg layer and EDX measurement at 5kV showing the various elements along the layer, b) half hydrogenated 400 nm Mg film, where the electron beam creates "holes" in the hydride portion of the layer, c) fully hydrogenated [Ha17].

SEM images show a "hole" effect on the assumed hydride part. It is known that MgH_2 is sensitive under the electron beam. A. Surrey et al. [SSR17] have reported that an electron beam can induce dehydrogenation of MgH_2. What is remarkable to observe here, is that these "holes" appear only above a line in the half-hydrogenated sample in Figure 5-6b), which obviously indicates a reaction front. In Figure 5-6c), the same effect is observed for the fully hydrogenated sample, but now the "holes" appear everywhere in the sample. Therefore, it is concluded, that these holes, are created from the instability of the hydride phase under the beam. In 2011, Dura et al. reported the observation of similar "holes" in a Mg hydrogenation system [Du11]. They attributed this effect to the fact that the lattice of the Mg matrix is expanding upon hydrogenation. When the electron beam of the SEM induces dehydrogenation, the extra space left from this expansion creates these holes. Noticeably, the beam induces dehydrogenation of the film, even at a low acceleration voltage of 5 kV.

To clarify the microstructural conditions in more detail, cross-sections of the same samples were prepared and investigated by transmission electron microscopy. Figure 5-7 shows three stages in correspondence to the XRD diffractograms of Figure 5-1. In the as-deposited state (Figure 5-7a), the Mg layer reveals a columnar grain structure with a pronounced texture, the latter also confirmed by the reflection intensities in the corresponding selected area diffraction pattern - SADP (Figure 5-7d). The visibly pronounced fiber texture is also in agreement with the XRD results previously shown, with one main peak along the preferred texture axis.

A partially hydrogenated sample (200 °C / 20 bar, 100 min) is shown in Figure 5-7b). The former homogeneous layer has split into two halves. In the upper area, close to the surface, the microstructure has transformed to fine globular grains. Also there, the fiber texture has disappeared from the SADP (Figure 5-7e). Noteworthy, the diffraction pattern of this region shows traces of MgO instead of MgH_2 ,

which serves as evidence of the instability of the hydride under the electron beam [SSR17]. Furthermore, the transfer of the samples from the FIB to the TEM was done in air, which can oxidize the thin (few nm thick) lamella. Nonetheless, a layer-like reaction is clearly identified by the reaction front in the microstructure. A sample hydrogenated for 250 min at 200 °C / 20 bar demonstrates full hydrogenation (Figure 5-7c). In summary, it is concluded that the hydride is formed uniformly at the surface of the film and grows towards the substrate in a uniform layer-like reaction.
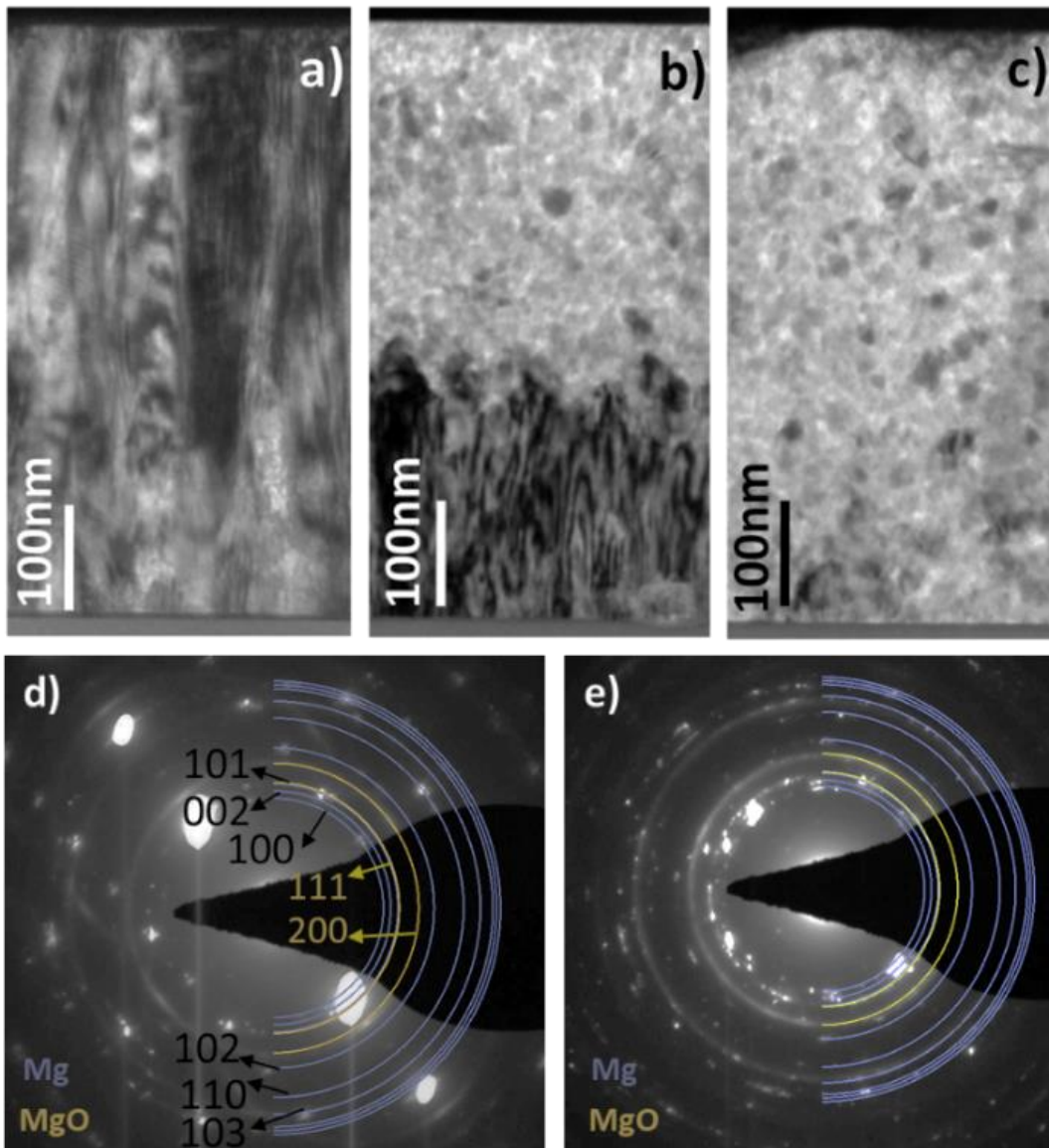
Figure 5-7: TEM bright field images of cross sections of a 400 nm Mg layer (layer surface at the top): a) As-deposited, b) partially hydrogenated at 200 °C / 20 bar / 100 min, c) fully hydrogenated 250 min. Corresponding SADP of d) Mg and e) MgH$_2$. MgH$_2$ has transformed into MgO under the electron beam.

Further analysis was completed on the as-deposited state using dark field imaging of the sample. One of the bright spots/reflections along the diagonal of the SADP was chosen for imaging. Direct imaging of this area in dark field, as shown in Figure 5-8, shows the strong fiber texture of the as-deposited sample more clearly. Many of the columnar single grains are appearing bright in dark field imaging.
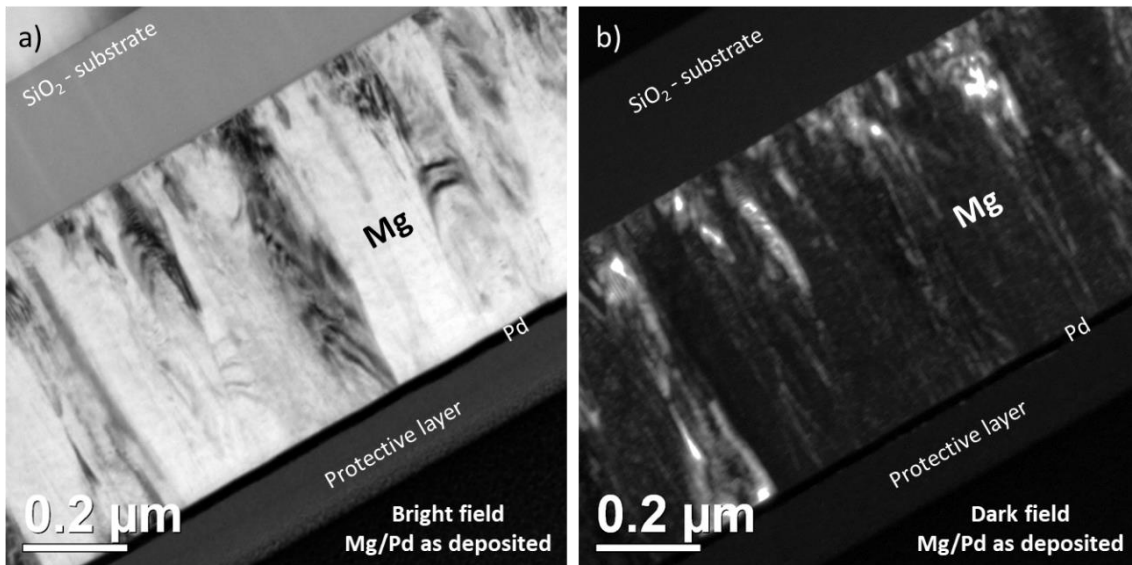
Figure 5-8: Bright field a) and dark field b) images of an as-deposited sample of 500 nm Mg and 20 nm Pd. The protective layers from the FIB sample preparation is observed.

5.1.3   HRTEM investigations

5.1.3.1   After high temperature (200 °C) treatment

Further TEM investigations at higher resolution were carried out in order to observe details at the interfaces. Figure 5-9 shows a bright field image of a partially hydrogenated sample where the hydride is shown again to nucleate at the Pd/Mg interface (close to the Pd layer shown in the figure). The equi-axed fine grains of the hydrogenated part are more clearly visible in the dark field image in Figure 5-9b). Figure 5-9c) shows a higher magnification of the layer close to the substrate, where the layer is expected to represent pure Mg. HRTEM allows measurement of the lattice planes observed. Lattice plane distance, measured from the image obtained close to the substrate, with the help of ImageJ software, gave an average value of 3.36 ± 0.05 Å, the value of lattice parameter from literature of Mg as given in Table 1 is 3.21 Å, whereas for MgH_2 the lattice parameter is 4.50 Å. This confirms that mainly pure Mg is present in this part of the film.

Figure 5-9d) shows a respectively higher magnification of an area closer to the surface, where the hydride is expected to be formed. Here, the average value of the lattice obtained is equal to 2.41 ± 0.3 Å. An attempt was carried out to see the lattice planes of the two phases of the layers. Unfortunately, the hydride is not stable under the electron beam, as discussed previously. However, the lattice parameter of MgO given in literature is equal to 2.573 Å. This supports previous SADP shown Figure 5-7, obtained at the partially hydrogenated sample showing the presence of MgO.
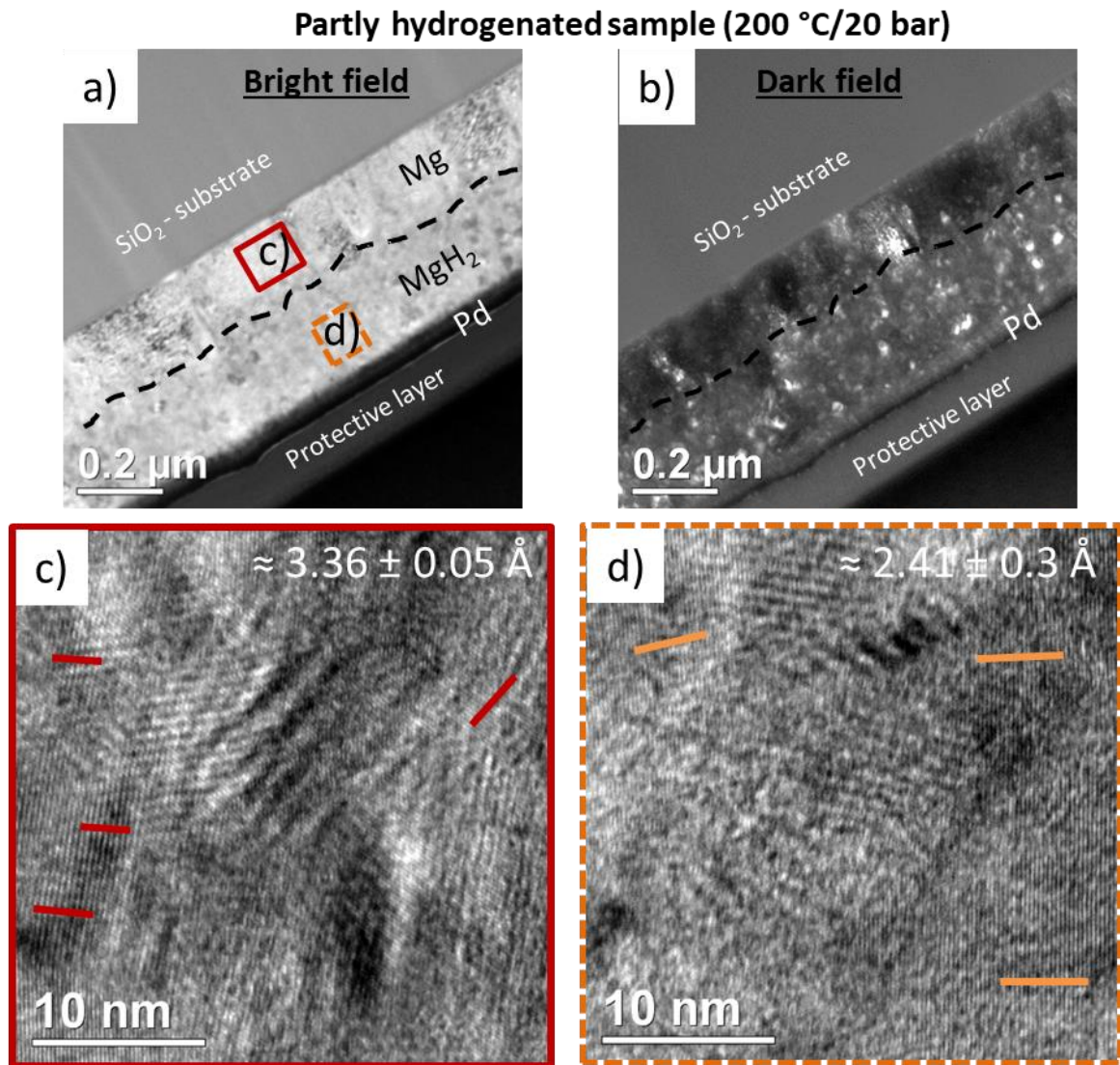
Figure 5-9: a-b) TEM bright field and dark field images of a partially hydrogenated sample 400 nm Mg 20 nm Pd. c) HRTEM of an area close to the substrate where Mg is present, the lattice planes observed give an indication of the pure Mg phase (≈3.21 Å). d) HRTEM of an area close to the surface where the hydride is formed. The lattice parameter of the oxide is measured in the planes visible (≈2.573 Å).

From the phase diagram between Mg and Pd, intermetallics may be expected, especially since the Pd peak disappears in the XRD after heat treatment, as previously presented (see Figure 5-1). From the phase diagram shown in Figure 3-5, Mg_5Pd_2 and Mg_6Pd are the phases expected to be observed at 200 – 300 °C. In order to see whether there was any mixing of the metallic elements, HRTEM images were taken especially from the respected interface. Figure 5-10 shows the comparison between a Pd layer as-deposited and the Pd layer after partial hydrogenation at 200 °C. Clearly, inter-diffusion of Pd and Mg is observed. However, the initial thickness of this Mg-Pd mixed layer, during the first hydrogenation, remains very small, which is probably the reason it is not observed in the previously shown XRD.
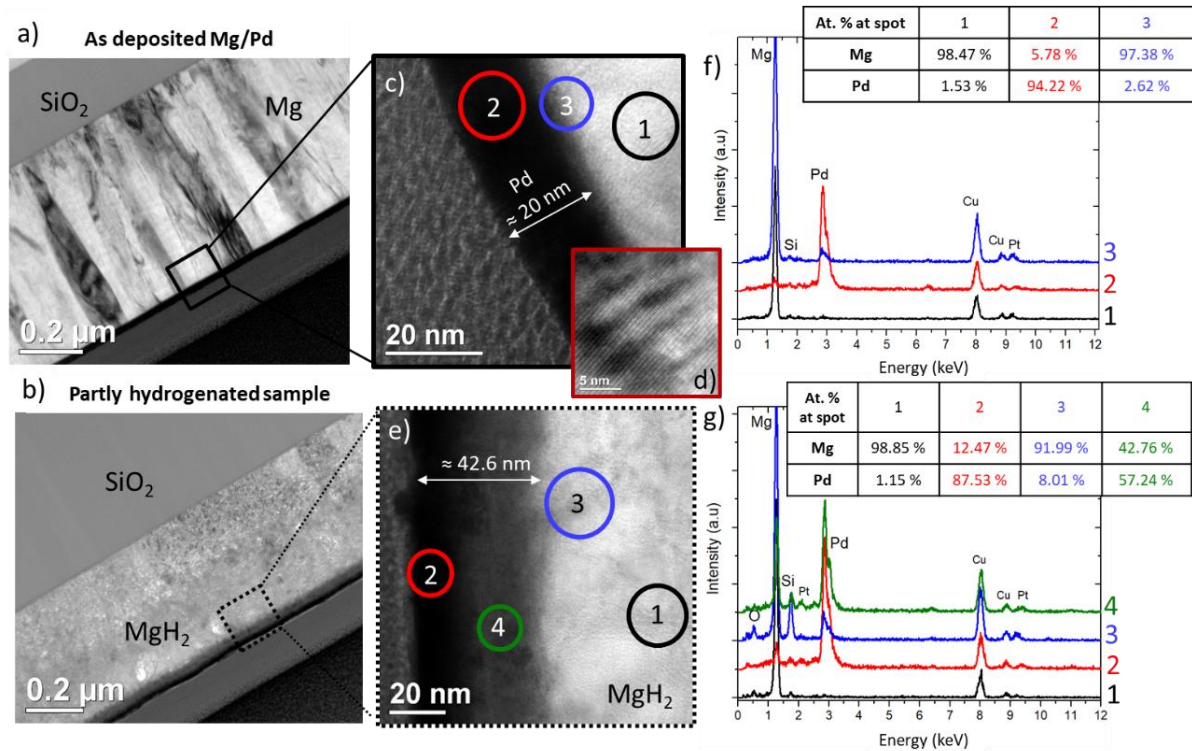
Figure 5-10: a) Bright field image of an as-deposited sample with columnar Mg structure visible. b) Bright field image of a partially hydrogenated sample, where the hydride has been in a layer formed closer to the surface. c) HRTEM of the Pd interface on the surface with each spot indicating the EDX spectra position. d) HRTEM of a thinned Pd layer, where its crystallinity is observed, due to the visible lattice planes. e) Higher magnification of the interface between Pd and Mg after hydrogenation at 200 °C. The EDX spectra obtained demonstrate the reaction of Pd with the Mg layer upon hydrogenation. The atomic percentage of each element is indicated respectively in each table in f) and g).

In order to confirm this mixing reaction of Mg-Pd, EDX spectra were taken by focusing the electron beam on the respective areas. Figure 5-10 (f), shows in black (spot 1), that in the region of the Mg layer no Pd is present since the spectrum shows 98.47 % Mg. The percentages given in the table are calculated without the Cu and Si signals, also visible in the spectra for a clearer comparison. Cu is detected from the sample holder of the grid, as well as from the C2 aperture used in the TEM. The Si signal is detected from the substrate, which is large in comparison to the studied layer, and some scattering is unavoidable. Regarding the unavoidable inaccuracies, the spectra from the surface region demonstrate that the Pd layer is purely made of Pd, as shown in red (spot 2) with 94.22 %. Spot 3 in Figure 5-10f), confirms the sharp interface between the two layers in the as-deposited state since 97.38 % of Mg is observed.

In contrast, after heating, Figure 5-10 (g) shows the partially hydrogenated sample. The presence of Mg inside Pd in green (spot 4) is pronounced with 57.24 % of Pd and 42.76 % of Mg. Furthermore, some presence of Pd inside Mg is seen in spot 3 (blue), where 8.01 % Pd is observed. Even at the spot 2, which is very close to the surface (red), Mg is present at 12.47 %. This shows, that part of the Mg was not hydrogenated, but has diffused into the Pd layer. However, verification of the exact phases

that are formed is not possible here, since the EDX does not give enough precision. It can be assumed that within the Mg-Pd phases formed, some part of pure Mg/MgO is present. As an independent confirmation, an important increase in the thickness of the Pd layer is observed from 20nm as-deposited to ≈ 42.6 nm after hydrogenation is noticed. This interaction of Pd/Mg shows a direct problem for the dehydrogenation process, discussed later, as well as for the cyclability of this system, since the Pd layer is no longer as effective as at the beginning. This Mg-Pd phase will be further discussed in the dehydrogenation chapter, where its stability and impact is shown.

5.1.3.2 Low temperature reaction (50°C)

In order to investigate the stability of the Mg/Pd interface, further TEM images were taken of samples hydrogenated at lower temperature for a longer period of time. The sample shown in Figure 5-11 was kept in a hydrogen atmosphere of 20 bar and 50 °C for 82 hours until full hydrogenation took place. The Pd layer appears to be more stable than what was shown earlier in Figure 5-10, when 200 °C was used for the hydrogenation. The layer did not grow drastically after the days it took to fully hydrogenate, since its thickness appears to be close to the as-deposited one.

A thin interfacial layer appears grey and by the analysis of the corresponding spot 2 by EDX, some traces of Mg are found. However, the amount looks near identical to spot 2, measured previously on the as-deposited sample (Figure 5-11). This strongly suggests that the Pd layer stays stable at low temperatures. Hydrogenation is possible at such low temperatures, however, it takes much longer since the diffusion is decreasing drastically. Unfortunately, as it will be discussed later in the desorption chapter (chapter 5.3), unloading of hydrogen is not possible at such low temperatures, where the Pd layer could stay stable.
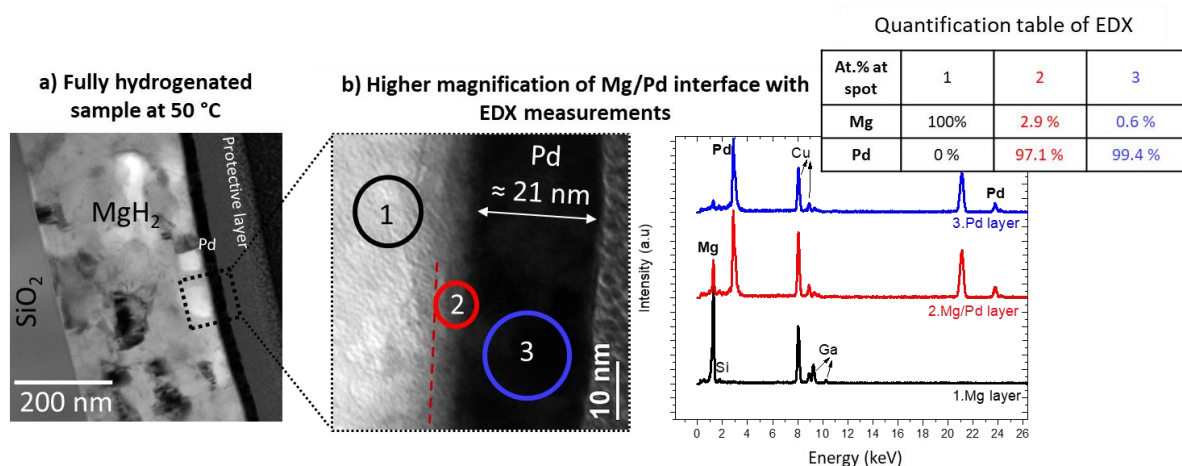
Figure 5-11: a) Bright field image of Mg/Pd interface of a fully hydrogenated sample at 50 °C (4861 minutes under hydrogen atmosphere). b) Higher magnification of the interface where EDX spectra is shown for each part of the sample 1. The Mg layer (white) 2. The Mg-Pd (grey) interface 3. The Pd layer (black).

5.1.4   Conclusion on XRD and TEM characterization

In summary, it has been shown so far that the hydrogen loading inside the Mg metal can be observed by XRD and TEM investigations. As measured by XRD, hydride formation starts at about 100 °C. The lattice expansion of Mg is visible and shown by in-situ XRD experiments, to initially be caused by thermal expansion. Once the hydride is formed, compressive stresses decrease the lattice parameter of Mg. In addition, a microscopic imaging of the co-existence of MgH_2 and Mg was performed using SEM and TEM. It clearly shows, that the hydride is immediately formed at the interface between the Pd catalyst and the Mg thin film, and grows in a layer-like geometry towards the substrate. The ion and electron beam, for cross section view preparation, damages the hydride phase, but the microstructure transformation between Mg and MgH_2 is nevertheless a reliable indicator. The transition from a columnar grain structure of the as-deposited Mg thin film to an equiaxed grainy structure demonstrates the hydride unambiguously. HRTEM shows the crystallinity of the formed layers and allows a further confirmation of the elements present in each layer. It also allows the observation of the Mg/Pd interface, which appears to be unstable, even during the first hydrogenation treatment at elevated temperatures. So far, a comprehensive way to qualitatively observe the kinetics of hydride formation is presented. The combined techniques will allow a measurement of the diffusion coefficients and will give further information on the mechanism of hydrogenation inside the Mg layer in the following chapters.

5.2   Hydrogen Transport

5.2.1   Kinetics of hydrogenation at 200 °C

Using the techniques previously mentioned, it is possible to determine the state of hydrogen loading. The mechanism of diffusion can be characterized by the transport equations that were introduced in chapter 2.2 by evaluating the time of full hydrogenation at different initial film thicknesses. Figure 5-12 (a) presents the measured growth kinetics on a linear scale, showing the time necessary to fully hydrogenate a specific layer versus its thickness as observed for hydrogenation at 200 °C / 10 bar (unfilled symbols) and at 200 °C / 20 bar (filled symbols). Figure 5-12 (b) shows the same experimental data plotted as thickness squared versus time. Multiple samples were measured to reduce errors. The error bars in time are determined from samples that were found to be still partially hydrogenated when tested for slightly less time. The error bars in thickness represent the possible variation in the film deposition that might occur from the different positions of the substrates with respect to the target during sputter deposition. Comparing both plots, the hydrogenation proceeds linearly with time in the studied range of thickness. Next to each data set, the slopes representing the growth rate are stated.

It is also indicated that thicker Pd layers at the surface still improve partially the kinetics, however, without having a dramatic influence.

A linear kinetics applies, which means that the transport is probably interface controlled (see chapter 2.2). The possible interfaces in this case are a) H gas/Pd layer b) Pd/Mg interface or c) MgH₂/Mg interface. However, since H_2 is known to split into atoms at the surface of Pd and to diffuse through Pd very quickly [ALJ99], hydrogen splitting at the surface is not considered to be the limiting process. Moreover, work on Ti described later in chapter 6.3, shows the catalytic effect of Pd, since hydrogenation of Ti is shown to be possible within seconds and at room temperature. By changing the transition metal, further investigations could help understand which of the two remaining interfaces is the limiting one. However, during this work, emphasis was given to studying the same system at different temperatures.

Having a constant hydrogen supply on the surface and adapted to the linear regime, the growth rate of the hydride can be formulated by rearranging equation (12):

$$\frac{d\Delta x}{dt} = \kappa \frac{\Delta \mu_H}{RT} \tag{30}$$

in which Δx and κ denote the width of the hydride layer and the linear growth constant respectively. k and T have their usual meaning.

The driving force $\Delta\mu_H$ to the growth is the difference of the chemical potential on each side of the interface, as explained in more detailed in chapter 2.2.1. On one side, the chemical potential of hydrogen practically corresponds to the gaseous state μ_H , and on the other side, the chemical potential of the MgH₂ phase at the hydrogen solubility limit μ_{Me-H} in the disordered alloy. So, the difference of the chemical potential across the controlling interface can be calculated

$$\Delta\mu_H = \mu_H - \mu_{Me-H} \text{ with } \mu_H = \mu^0 + \frac{RT}{2} \ln \frac{p_{H_2}}{p^0} + \frac{\partial\mu^0}{\partial T}(T - T^0) \,. \tag{31}$$

p_{H_2} and T are the corresponding pressure and temperature of the hydrogenation conditions in the experiments. In order to calculate μ_{Me-H}, the pressure of formation of the hydride was taken into account, obtained from reported pcT curves, as given in Figure 3-3, considering the pressure of the phase equilibria at the experimental temperatures. Table 7 gives the final values of $\Delta\mu_H$ for the Mg system at the different experimental conditions.

Table 7: Chemical potential difference ($\Delta\mu_H$) calculated for the experimental conditions investigated in the Mg system.

CONDITIONS	$\Delta\mu_H$ (kJ/mol)	μ_{Me-H} (kJ/mol)	μ_H (kJ/mol)
200 °C, 10 bar	3.5	181	184
200 °C, 20 bar	4.8	181	186
300 °C, 10 bar	5.5	170	175
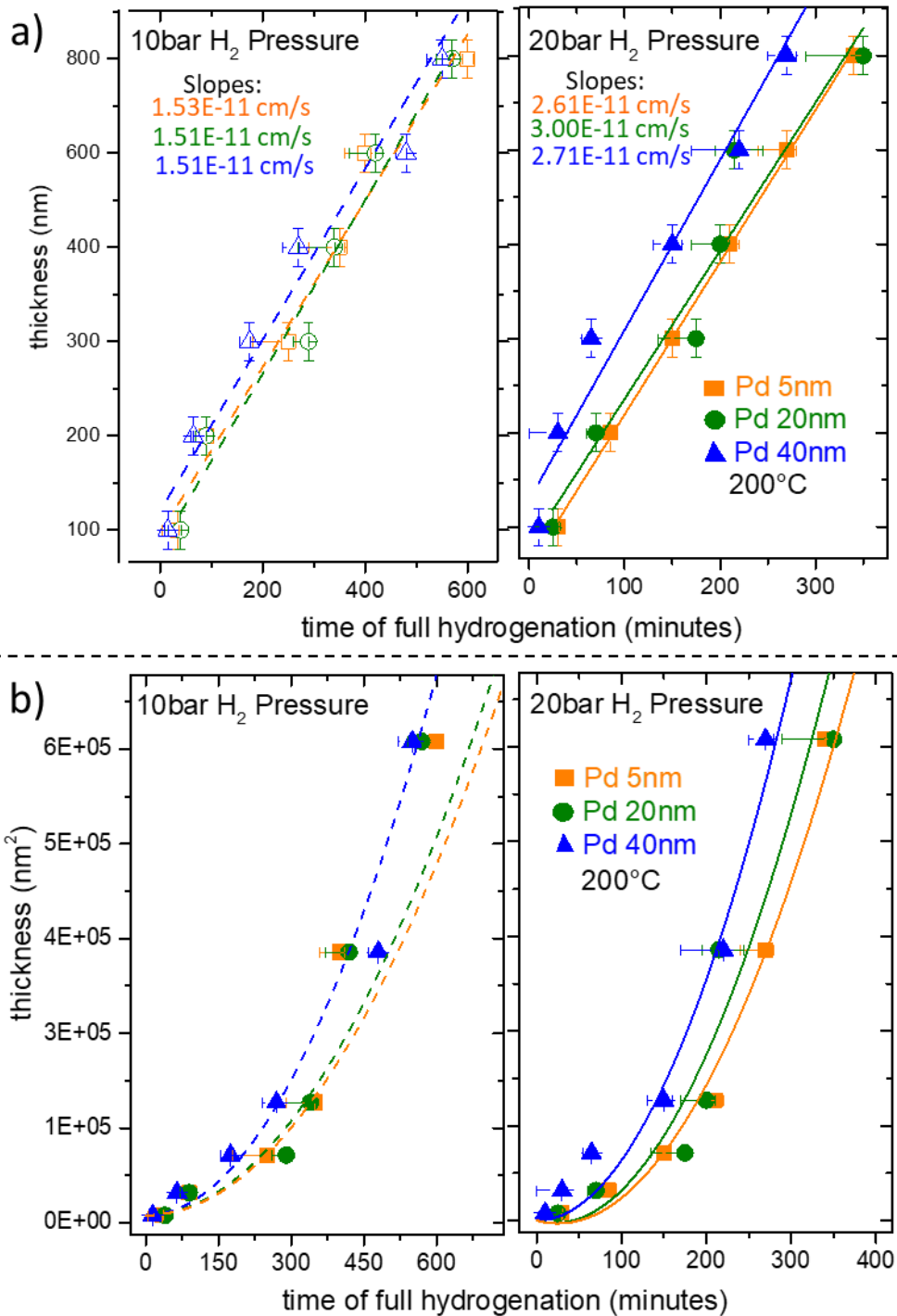
Figure 5-12: Hydrogenation of Pd/Mg layers at different thicknesses. a) Time of full hydrogenation versus film thickness (linear plot) at 200 °C / 10 bar and 200 °C / 20 bar. Data obtained with different thicknesses of Pd as indicated by different symbols b) Thickness squared versus time (parabolic plot) confirming the linear regime at these conditions and thicknesses.

Evaluating the slopes of the experimental data in Figure 5-12 (a) in terms of equation (30) delivers the barrier coefficient for both pressures given in Table 8.

Table 8: Barrier coefficient experimentally calculated by the linear regime observed at 200 °C
at small thicknesses.

EXPERIMENTAL CONDITIONS	BARRIER COEFFICIENT κ (cm⁄s)
10 bar	$2.84\cdot 10^{-12}$
20 bar	$1.21\cdot 10^{-12}$

For all three data sets the R^2 value obtained from the fit is between $0.92 - 0.99$, showing that the fitted lines are close to the experimental data points. The fact that at 200 °C a linear kinetics is observed at all, requires a minimum diffusion coefficient of H in MgH_2 as equation (13) shows: $D_{limit} \geq \kappa\cdot\Delta x$. It can therefore be determined, for the thickest studied layers, that $D_{limit} \geq 7.13\cdot10^{-16}$ cm^2/s. When compared to literature, this limit of diffusion seems to be close to the already reported diffusion coefficient of H through the hydride phase [Ya08]. Comparing the two different pressures, no significant difference is visible. As mentioned in chapter 2.2, usually after a linear growth, a transition to the parabolic regime is expected. We assume therefore that the conditions (thickness, temperature, pressure) used during these experiments are already close to this linear-parabolic transition.

5.2.2 Kinetics of hydrogenation at 300 °C

For comparison purposes, the hydrogenation rate at a higher temperature, 300 °C is characterized as well. Figure 5-13 shows the time to full hydrogenation at 300 °C / 20 bar versus time, in again linear a) and quadratic b) thickness scales for a direct comparison. The straight linear relation in the latter clearly identifies a parabolic kinetics that now demonstrates, at this higher temperature, a diffusion-control, showing that MgH_2 creates a blocking barrier against faster reaction.
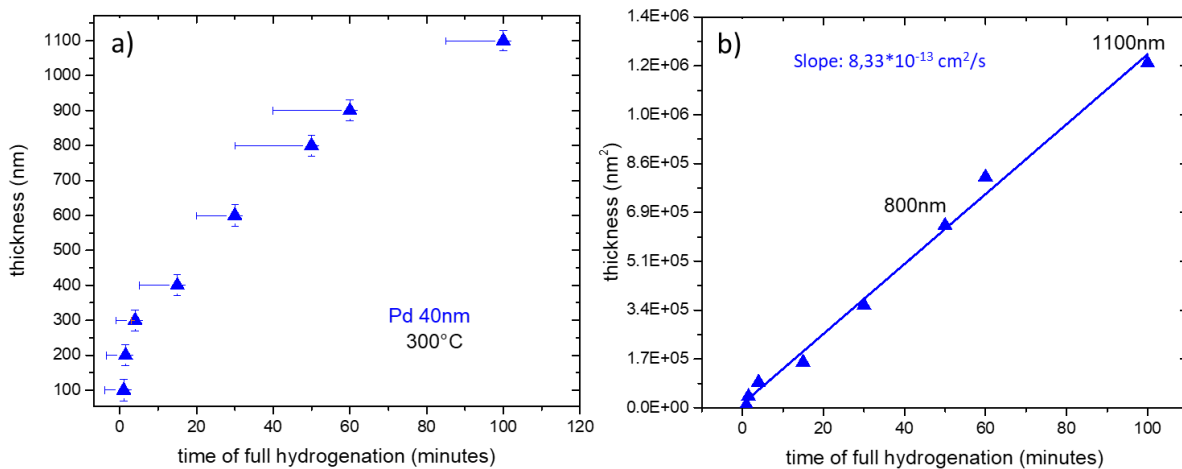
Figure 5-13: a) Hydrogenation of Pd/Mg at 300 °C / 20 bar. b) Squared thickness versus time of full hydrogenation showing the parabolic kinetics at these conditions.

Using the slope of the experimental data in Figure 5-13 (b) and equation (17), previously introduced with the value of $\Delta\mu_H$ given in Table 1, the diffusion coefficient of H at 300 °C is $D_H^{MgH_2}$ = 6.18 · 10^{-13} cm^2/s. Here again, the R^2 value of the fit is equal to 0.99, showing that the experimental points are well described. Figure 5-14 shows a schematic representation of the chemical potential change in the case of a diffusion-controlled mechanism, where the thickness of the hydride layer increases with time and this slows down further diffusion of hydrogen over time.
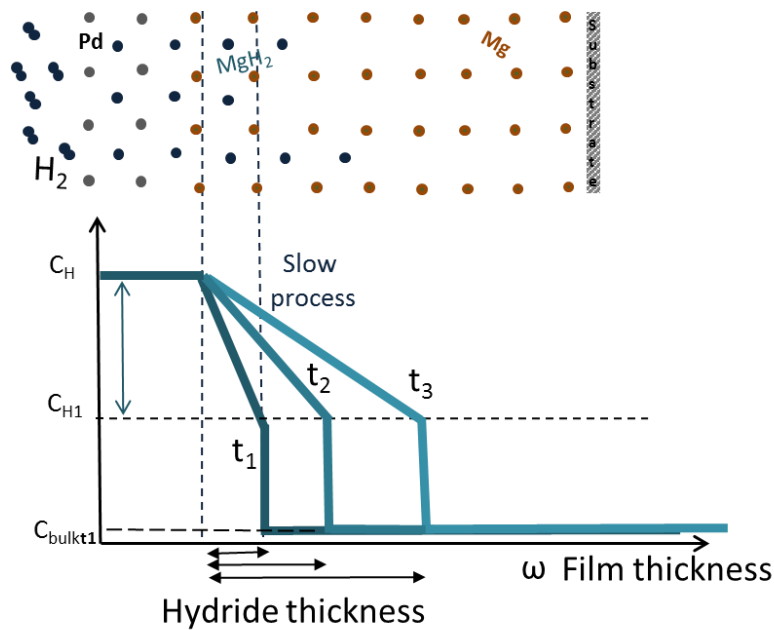
Figure 5-14: Schematic representation of hydrogen diffusing inside Mg at 300 °C, where diffusion control reaction takes place. Over time, the hydride gets thicker and so hydrogen diffuses more slowly through it.

In summary, along the study of hydrogen transport so far, the growth of the hydride at 200 °C is observed following a linear kinetics. This indicates that the transport across the Pd/MgH$_2$ or MgH$_2$/Mg interface is the rate limiting factor. The hydride is nucleated at the Pd/Mg interface and grows from the surface towards the substrate. The growth constant is quantitatively calculated to be κ = 10^{-12} cm/s and the diffusion limit at 200 °C of H in MgH$_2$ is $D_H^{MgH_2}$ ≥ 7.13 · 10^{-16} cm^2/s. Any layer reaction is expected to follow a linear time dependence at the beginning. However, after having reacted to sufficient by large reaction thickness, diffusion through the hydride is expected to become the rate-limiting factor. It is surprising to see that the transition towards a parabolic growth is not observed in the later stages. For this reason, a new setup was developed for investigating the samples with more precision, using the characteristic resistance of the concerned materials. However, the experimental data at 300 °C / 20 bar, evidencing a parabolic growth, allow experimentally calculating the exact diffusion coefficient of hydrogen in the hydride. At 300 °C, the diffusion coefficient is consequently determined to be equal to: $D_H^{MgH_2}$ = 6.18 · 10^{-13} cm^2/s.

5.2.3   Resistance measurements

Measuring a sample at specific conditions (pressure, temperature, layer thickness) for different stages of hydrogenation, is a time consuming method, which makes it difficult to be precise, especially by ex-situ XRD measurements. For this reason, a way to investigate the hydrogenation in-situ was further developed during this work. Resistance changes in the material, as mentioned in chapter 3.1.2, are dominant when hydrogen is inserted into the Mg matrix.

The influence of temperature on the resistance of Mg was initially experimentally measured in order to see how the pure Mg layer behaves when heating up from room temperature to 200 °C. Figure 5-15 (a) shows the experimental values of the sheet resistance of pure Mg, indicating the decrease of resistance with increasing thickness. This is natural when the layer is considered as an electric circuit. If a film consists of lanes of constant thickness, "paths" for the electrons, a thicker layer will eventually have more paths. The average speed of electrons remains the same in all thicknesses, therefore, the gradient of electrons stays constant. Per unit cross section area each layer will carry the same current, however, in total, the current will be higher. A higher current at a given voltage means a lower resistance. This behavior is clearly observed at both, room temperature and elevated temperature. Furthermore, since Mg is a metal, it is no surprise that the resistance is increasing when the temperature is increasing. When a current is applied and electrons travel through the lattice, the waves interfere with the lattice and this causes a resistance in the material. In metals in which a crystal structure is present, temperature excites phonons in the lattice and thus more interference between the Bloch waves increases the resistance.

In order to see the behavior of the hydride at different temperatures, Figure 5-15 (b) shows the resistance measurements carried out from room temperature to 200 °C. The sample is kept under hydrogen pressure, so that no dehydrogenation would take place while heating up. This shows how the resistance of the hydride is increasing with increasing temperature, showing that the hydride is not entirely an insulator, but has a metallic behavior, however, with a higher resistance than the Mg metal. The slight increase of resistance at about 70 min is most probably an effect, due to the fact that heating is unavoidable while passing a current through the thin sample. It takes a few moments for the thermocouple to regulate this difference until the 200 °C is constantly obtained. In order to avoid this effect, all samples were always filled up with hydrogen after the required temperature was reached and confirmed to be constant.
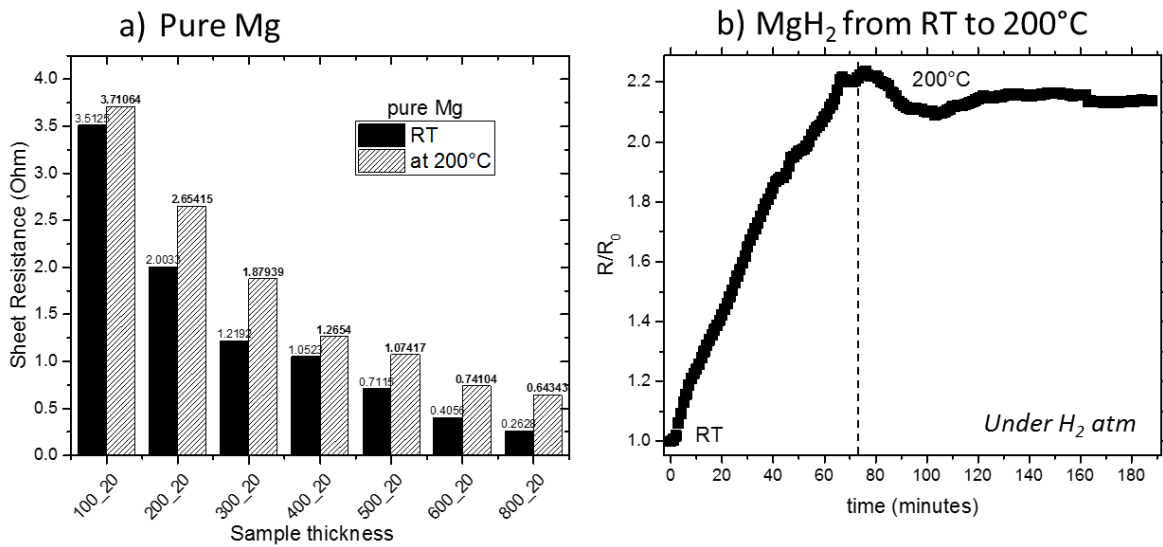
Figure 5-15: a) Sheet Resistance of Mg at room temperature and 200 °C b) Resistance measurement from room temperature to 200 °C.

In four-probe measurements, a voltage drop is measured before the inner contacts, while a constant current of 1 mA is applied to the outer contacts. The samples were first heated to 200 °C and then hydrogen (20 bar) was inserted into the reactor. Figure 5-16 shows the experimental response of resistance change upon hydrogen loading in an Mg layer of 250 nm thickness. The growth of the hydride happens mostly in the first stage, showing a low slope of increase of the resistivity. At the beginning, a small increase is observed where the hydride phase is growing, while towards the end of the process, shortly before complete loading of the film with hydrogen, a steep increase appears. This is the expected behavior of the resistance change, when two resistors in parallel are connected and the relative weight between the resistors is shifting. Therefore, by considering the layer system as varying resistors connected in parallel, evaluation of the system can be done. In comparison to Mg and MgH_2, the resistance contributed from the Pd layer on the surface can safely be neglected. In order to define the time of full hydrogenation, a tangent is plotted to the sharp increase observed at the end of the resistance, as shown in dashed line in Figure 5-16.

Several samples of different thicknesses of Mg were measured with a constant Pd layer of 20 nm on the surface. Figure 5-17 shows the resistance behavior of all the thicknesses investigated during this work. All samples show a similar behavior, with the sharp increase appearing after a characteristic time depending on the thickness of the initial Mg film. The time of full hydrogenation for the higher Mg thicknesses is shown in dashed lines, while Figure 5-18 (a) more clearly shows the smaller thicknesses, where the time for full hydrogenation is given for the samples of 100, 200, 300 and 400 nm of Mg. The table in Figure 5-18 (b) shows the characteristic time of full hydrogenation acquired for each thickness.
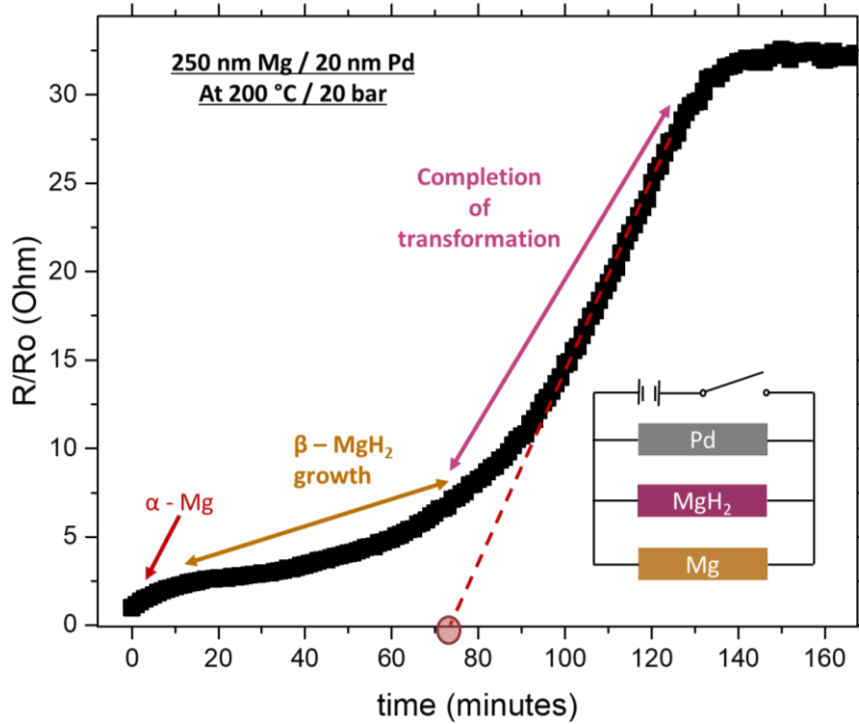
Figure 5-16: Example of resistance change upon hydrogen loading in a Mg 250 nm layer, 20 nm Pd hydrogenated at 200 °C / 20 bar. The time of full hydrogenation is obtained from the tangent along the sharp increase of the characteristic graph, as shown by the dashed line. The time used for further calculations is the one shown in a circle on the x-axis.
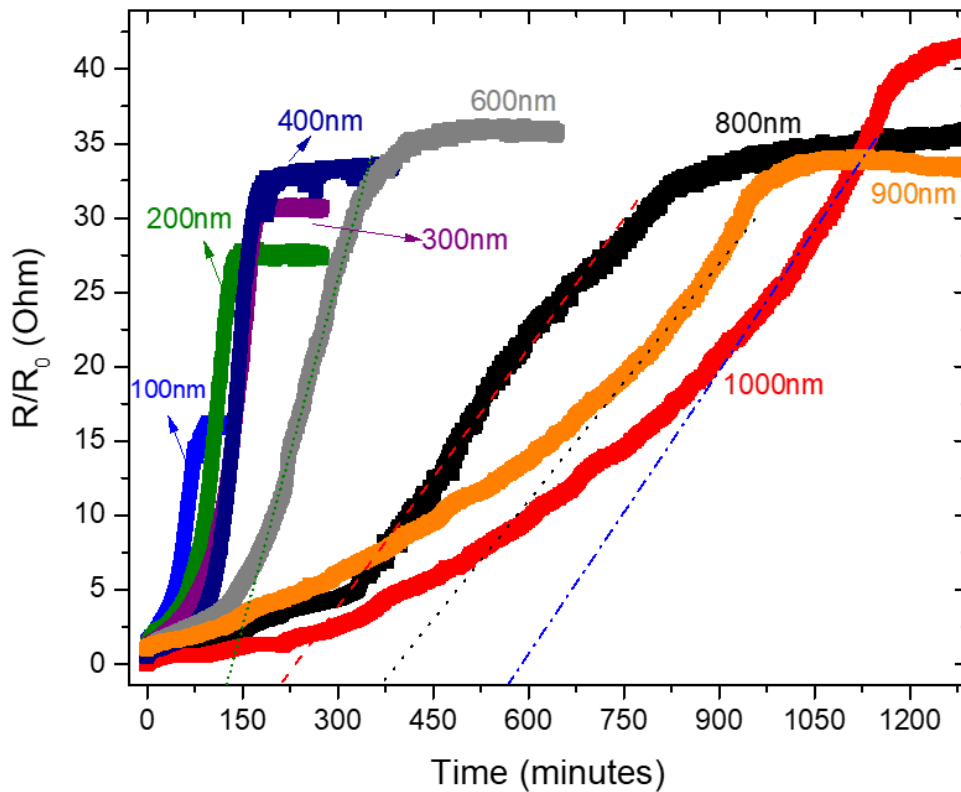
Figure 5-17: Resistance behavior of different Mg thicknesses (100 to 1000 nm) with 20 nm Pd on the surface. Hydrogenated at 200 °C and 20 bar. The time of full hydrogenation is shown with the dashed lines for each thickness.

Thickness (nm)	Time (minutes)
100	29.1 ± 3.0
200	69.1 ± 5.2
300	90.3 ± 4.7
400	108.1 ± 6.2
600	126.3 ± 3.5
800	214.8 ± 6.4
900	372.7 ± 8.5
1000	563.1 ± 10.5
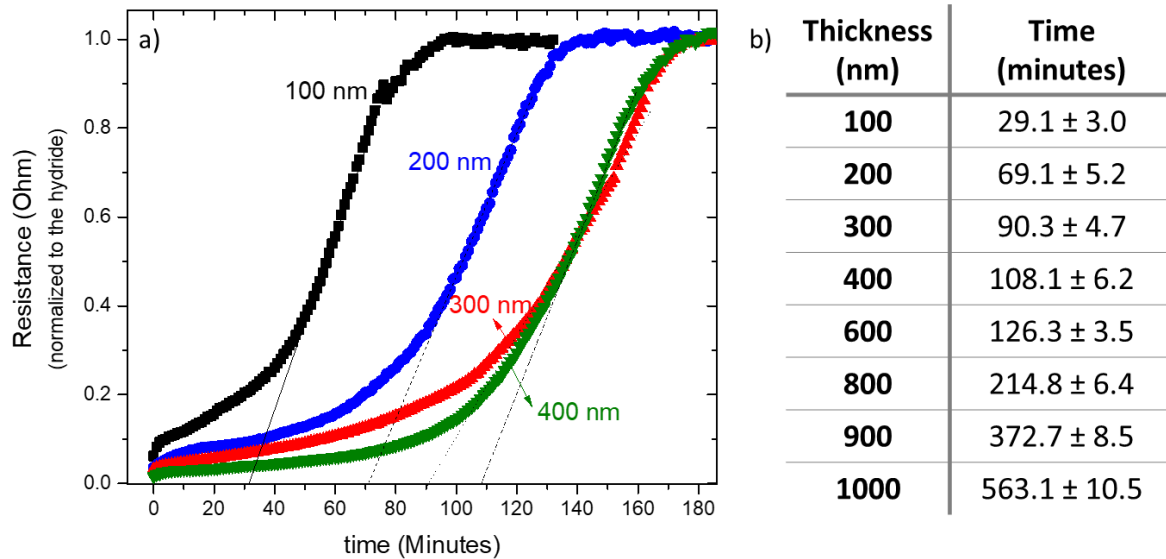
Figure 5-18: Resistance behavior normalized to the hydride value, of smaller Mg thicknesses (100, 200, 300 and 400 nm) with 20 nm Pd on the surface. Hydrogenated at 200 °C and 20 bar. The time of full hydrogenation is characterized by the dashed lines for each thickness.

Multiple samples were measured in order to obtain an average value of the time of full hydrogenation for each thickness. As an example, Figure 5-19 nominally shows the resistance behavior normalized to the final resistance (hydride) of two samples of same thickness (≈ 200 nm). As can be seen, there is no significant difference between the two samples and, most importantly, the two samples appear to have a similar time of full hydrogenation. The remaining small variation is probably due to a small difference in the initial Mg thickness. This is a clear indication that this method can produce precise measurements and reproducible results.
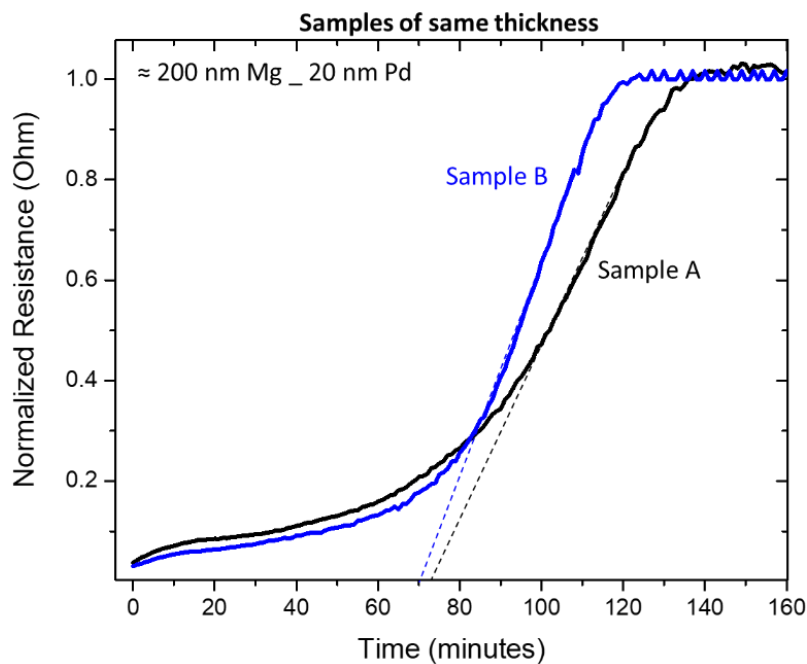
Figure 5-19: Resistance behavior during hydrogenation of two different samples of same thickness (200 nm). Hydrogenated at 200 °C and 20 bar. The time of full hydrogenation is shown to be close to each other.

For comparison with the growth kinetics observed by XRD in the previous chapters, the time of full hydrogenation for different thicknesses was measured at the same conditions 200 °C / 20 bar. Figure 5-20 shows the comparison between the time obtained by XRD measurements and resistance measurements, in both a) linear and b) parabolic scale. It is clearly observed in the parabolic scale in Figure 5-20 (b), that the linear kinetics transform into a parabolic one above a certain critical thickness. The transition to a diffusion-controlled mechanism is clear at about ≈ 600 nm. This shows that at small thicknesses, the atomic jumps of hydrogen across the interface are significantly hindered. Thus, leading to an interface controlled, linear growth regime until a relatively large thickness is reached. After that point, the hydride continues to grow according to a parabolic law.
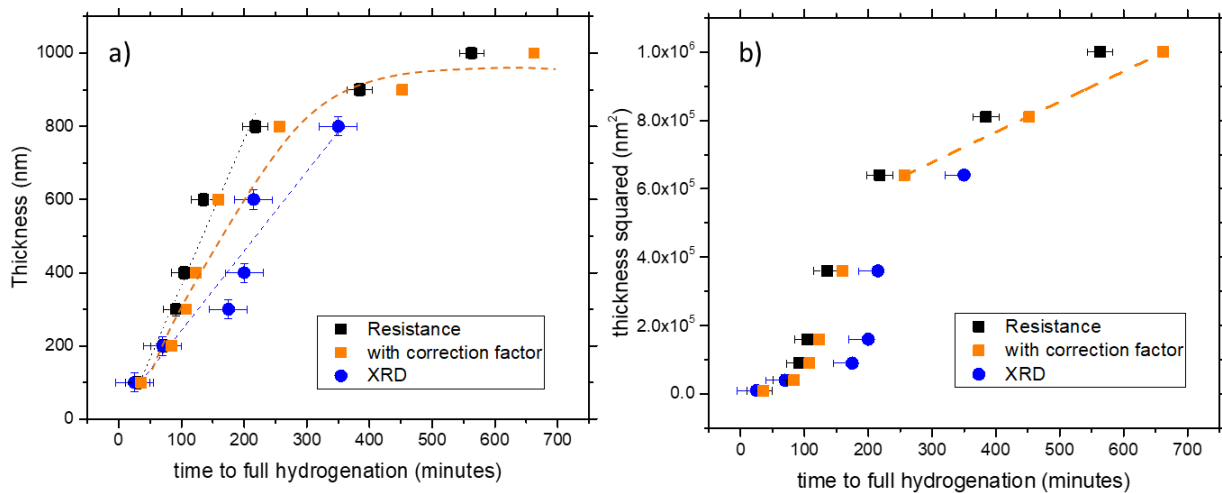
Figure 5-20: Growth kinetics at 200 °C / 20 bar on the a) linear and b) parabolic scale. The time of full hydrogenation is obtained with resistance mismeasurements shown in blue circles and a comparison to the XRD experimental data, discussed in the previous chapter, is shown with the black squares.

Comparing the experimental analysis by XRD ex-situ (blue circles) and the resistance measurements (black squares) in Figure 5-20, a clear deviation is observed. The change in resistance is more sensitive to smaller changes than the XRD measurements. This means, that if a small layer of few nanometers of Mg is still not hydrogenated, this Mg layer cannot be seen by the XRD. Nevertheless, the resistance measurements will reveal the difference. However, this is not the only reason of the variation between the two techniques. As explained later on in more detail, in Figure 5-24, the time of full hydrogenation obtained by the tangent at the inflection point of the graph represents only 85 % of the hydrogenation. For this reason, the additional points (orange squares) in Figure 5-20 represent the resistance measurements with the correction factor to a 100 % hydrogenation time.

Another way to evaluate the data in the case of the resistance measurements, is to create a model that fits the experimental parameters. In general, there are three possible mechanisms that the transport can obey: i) a linear regime ii) a parabolic regime or iii) a transition from linear to parabolic. From the data presented previously in Figure 5-20, it is expected that the real situation of hydrogen transport follows a combination of linear kinetics at the beginning and a parabolic behavior when the

hydride thickness becomes dominant. For the model created to fit the experimental curve, a simple consideration of equation (24) from chapter 2.2.2 is used:

$$\frac{1}{R_{total}} = \frac{b}{L}\left(\frac{d_0 - d_{MgH_2}(t)}{\rho_{Mg}} + \frac{d_{MgH_2}(t)}{\rho_{MgH_2}} + \frac{d_{Pd}(t)}{\rho_{Pd}}\right) \qquad (24)$$

where b and L are the width and length of the sample respectively, d_0 the initial Mg thickness of the sample, ρ the equivalent resistivity for each phase as obtained in the experimental data.

Therefore, a comparison can be obtained when replacing the change in thickness: $d_{MgH_2}(t)$ for each kinetics behavior by:

i)   Linear case: $d_{MgH_2}(t) = \kappa \cdot t$

ii)   Parabolic case: $d_{MgH_2}(t) = \sqrt{Dt}$

iii)   Combination of linear and parabolic. In this case equation (9) is considered where the atomic transport of hydrogen is given in relation to both growth constant and diffusion coefficient:

$$\frac{dx}{dt} \approx \frac{\nu}{\Omega_{sites}} \frac{D}{x + \dfrac{D}{\kappa}} \frac{\Delta\mu}{RT} \qquad (9)$$

Re-arranging the equation and integrating from 0 to a thickness x

$$dx\left(x + \frac{D}{\kappa}\right) \approx D \cdot \frac{\Delta\mu}{RT} \cdot dt \qquad (32)$$

$$\frac{1}{2}x^2 + \frac{D}{\kappa}x \approx Dt \rightarrow x = \sqrt{\frac{D^2}{\kappa^2} + D \cdot \frac{\Delta\mu}{RT} \cdot t} - \frac{D}{\kappa} \qquad (33)$$

Gives at the end: $d_{MgH_2}(t) = \sqrt{\dfrac{D^2}{\kappa^2} + D \cdot \dfrac{\Delta\mu}{RT} \cdot t} - \dfrac{D}{\kappa}$.

For the same reasons explained previously, the part of the Pd contribution is neglected since the conductivity of 20 nm layer is not expected to play a dominant role in this case. The chemical potential is considered to be the same as previously, is adding a factor to the final equation. Furthermore, this equation does not consider the inflection point consequently. A supplementary factor considering similar to a Johnson-Mehl-Avrami equation may be added to describe the stop of the reaction, when the Mg gest more and more consumed:

$$\frac{dx}{dt} \approx \frac{D}{x + \dfrac{D}{\kappa}} \cdot \left(1 - \frac{x}{x_{max}}\right)^{\gamma} \qquad (34)$$

where γ represents a shape factor.

Using equation (34), where the combination of linear to parabolic is used and the inflection point is

considered, a fitting to the experimental data of the different thicknesses can be achieved. Figure 5-21 (a) shows for example the case of a 300 nm sample.

This way, the average diffusion coefficient at 200 °C, obtained from different measurements with different thicknesses is $D_H^{MgH_2}$ = 0.14 ± 0.02 ·10^{-12} cm^2/s.

The model precisely follows the experimental data, and the parameters used in each case are shown in Table 9:

Table 9: Parameters used for fitting the resistance model to the experimental data

PARAMETER	VALUE for 100 nm	VALUE for 200 nm	*VALUE for 300 nm*	VALUE for 400 nm
D (cm²/s)	0.16· 10^{-12}	0.14· 10^{-12}	*0.15· 10^{-12}*	0.11· 10^{-12}
κ (cm/s)	0.05· 10^{-14}	0.08· 10^{-14}	*0.2· 10^{-14}*	1.5· 10^{-14}
ν	0.5	0.5	*0.5*	0.4
x (nm)	100	200	*300*	400
ρ_{Mg} (Ohm)	0.09	0.05	*0.03*	0.02
ρ_{MgH_2} (Ohm)	1	1	*1*	1
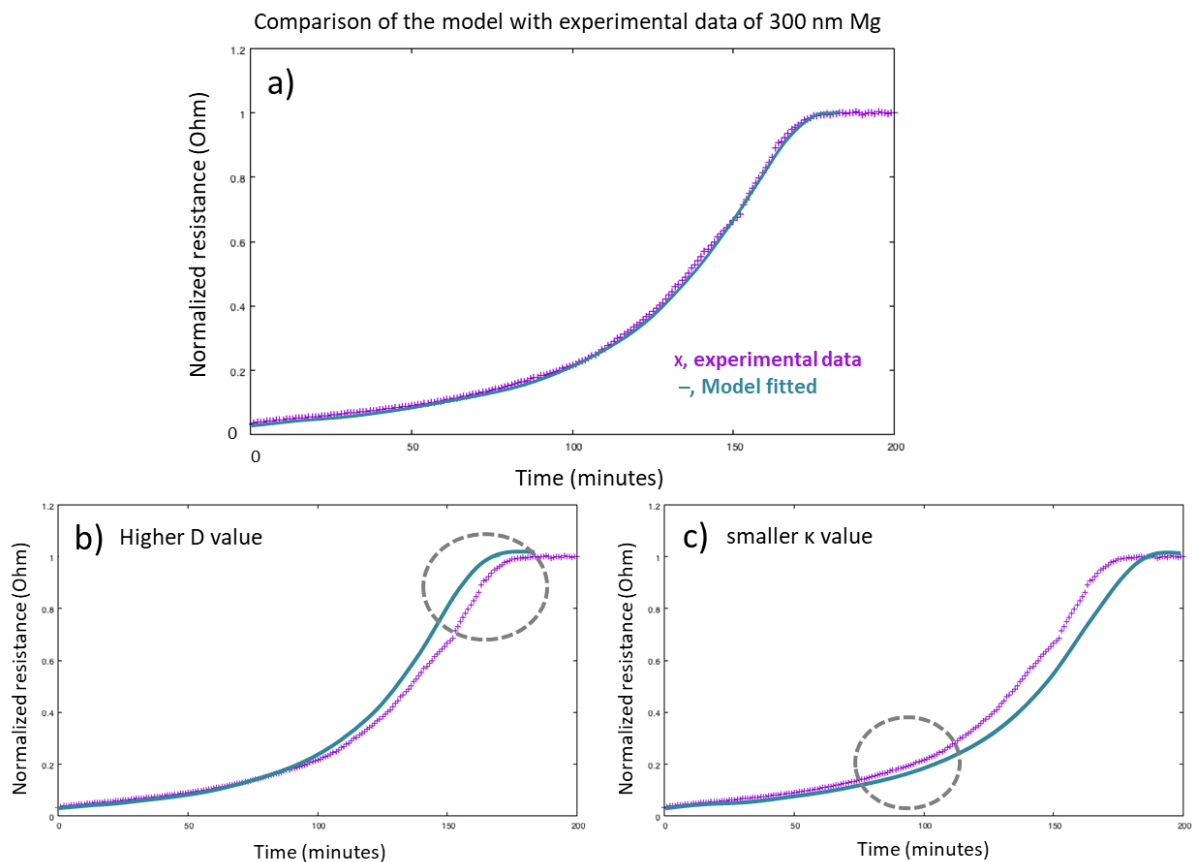
Figure 5-21: a) Modeling of the resistance change over time using the combination of both linear and parabolic law. The effect of b) the diffusion coefficient c) the growth constant is shown and the circles present the area of the graph, which changes drastically when changing each parameter.

The model is also helpful in identifying the effect each parameter has on the experimental behavior. Figure 5-21 (b) shows the effect of a faster diffusion coefficient, whereas Figure 5-21 (c) demonstrates the effect of smaller growth constant. All parameters have been tested and the ones for the best fit are given in Table 9. The graphs of more thicknesses showing the fitting of the model to the experimental data are given in Appendix 2.

A significant observation during this analysis of the data, is the fact that the model does not fit as nicely for larger thicknesses. At 600 nm, it is already difficult to find parameters that fit the model and at 900 nm and 1000 nm, it has been impossible. Looking closer, Figure 5-22 highlights the difference between the initial change in resistance when a thin layer of 100 nm of Mg is measured (see Figure 5-22 (b)) and when a thicker layer of 900 nm is tested (see Figure 5-22 (a)). The emphasized squares on the graphs focus on the initial part of the resistance change, where the sample of 900 nm has almost a straight line increasing. This shows that the initial mechanism in the case of thicker layers is not entirely similar. At the end however, where the parabolic part is shown, the graph follows a similar change. The tendency however is visible in all larger thicknesses. Meanwhile, the change is observed at the linear part, one could assume that the controlling interface is the one changing. Therefore, the experimental results in combination with the model calculations give strong evidence of the existence of a moving planar interface.
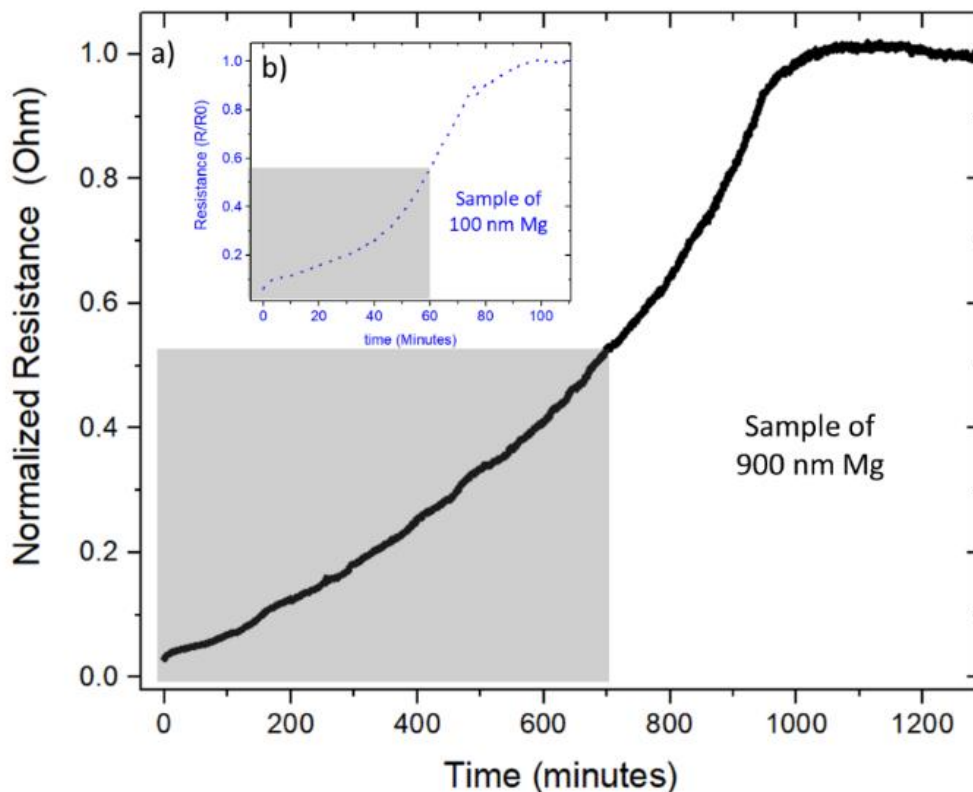
Figure 5-22: Experimental data of the resistance change in a) thick Mg layer of 900 nm and b) thin Mg layer of 100 nm. The gray area highlights the difference at the initial stage between the two. At a higher thickness, a more linear change in resistance is observed and the inflection point is not clearly visible anymore.

Additionally, in a smaller layer the nucleation of the initial hydride layer can play a more important role than in a thicker layer. Previous studies done by S. T. Kelly et al. [KC10] on synchrotron experiments, predict similar behavior of hydrogenation of epitaxial Mg thin films, however, in smaller thicknesses. They report the shift from interface to diffusion limited reaction at thicknesses of 200 nm. This difference most probably comes from the fact that the model is not completely thorough and characterizes the system in a very simple way. The importance of the Mg-Pd layer is clearly shown in previous chapters, which is not considered here during the model. One should also keep in mind that the fiber texture of the thin films may also affect this system slightly. At the second hydrogenation, where the texture is lost, the behavior might be different. This proves that the kinetics is very sensitive on the production method.

It is agreeably shown from the experimental and the model that the system follows a linear to a parabolic transition. Comparing this to the explanation given in chapter 2.2, Figure 5-23 emphasizes the change of the chemical potential a travers the film. A schematic representation of the linear regime that takes place at small thicknesses shows that the slow action is the transport of hydrogen from the Pd layer into the hydride layer. Since this is an interface controlled reaction the linear regime is observed at small thicknesses. In the case of a parabolic regime where the slow action is diffusion controlled the long arrow represents the slow diffusion of hydrogen through the hydride layer. This is more dominant at higher thicknesses and therefore parabolic regime is observed at the experimental high thicknesses as shown in Figure 5-20.
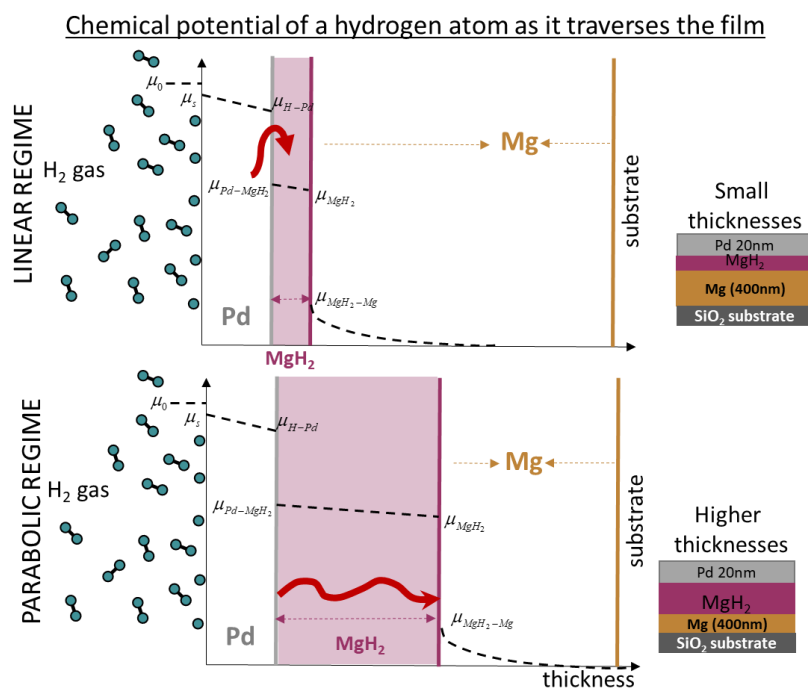
Figure 5-23: Schematic of chemical potential change of a hydrogen atom as it traverses the film. A comparison is given between the linear and the parabolic regime observed for the small and higher thicknesses respectively. The slower action in each case, controlling the hydrogen transport is shown by the thick red arrow.

Using the same model, the thickness of the hydride layer is calculated over time. Figure 5-24 demonstrates the change of the hydride formed over time. As established earlier, the time of full hydrogenation for each measurement is calculated by the tangent to the inflection point. As shown in the case of Figure 5-24, of a sample with an initial thickness of 300 nm Mg, at ≈ 90 min, which is the time used as "time to full hydrogenation" (see Figure 5-18 (b)), only 85 % of the Mg has transformed. Accordingly, an appropriate factor has to be used to correct the evaluation previously shown in Figure 5-20, and will later be used for calculating the diffusion coefficients at different temperatures.
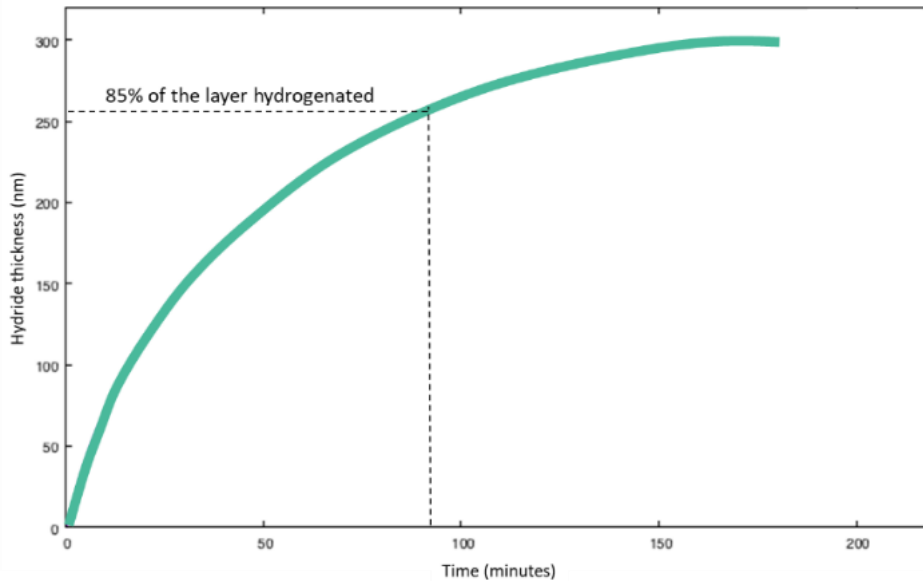
Figure 5-24: Thickness of the hydride formed over time simulated in a sample of initial 300 nm Mg thickness, created using the model of linear to parabolic kinetics.

Using the same principle, similar experiments at different temperatures were performed. This allows determining the temperature dependence of the diffusion coefficient. Figure 5-25 demonstrates the experimental change in resistance at different temperatures. In a) the low temperatures (room temperature and 50 °C) and in b) the higher temperatures (100 – 200 °C). The time of full hydrogenation used for the diffusion coefficients is illustrated by the dashed lines.

Due to similar difficulties, as previously for the higher thicknesses, the model could not be applied to the entire range of different temperatures. Therefore, the typical parabolic law of diffusion is used:

$$x = \sqrt{Dt} \qquad\qquad (17)$$

where x represents the thickness of the layer and t, the time of full hydrogenation (time of 85 % hydrogenation used as the correction factor). For more accuracy, all layers used for the calculation of the diffusion coefficients were also cut by the FIB to obtain an accurate value of the layer thickness. The SEM images of the layers are shown in the Appendix 1.

By plotting the logarithm of the diffusion coefficient versus inverse temperature, the Arrhenius plot and so the calculation of the activation energy E_a becomes possible. As explained in more detail in

chapter 3.1.1, E_a represents the activation energy for hydrogen jumps in magnesium hydride and, therefore, the minimum energy required for the reaction between hydrogen and magnesium to occur. In the case of MgH_2, this value was not established previously by a continuous series of measurements. From Figure 5-26, it is observed that while temperature increases, the diffusion coefficient increases. Adding the value calculated from different thicknesses at 200 °C (green rectangular), it is clear that depending on the model used, the diffusion coefficient still varies. Yet, both values are within one order of magnitude difference, which shows that presumably none of the models is perfect.
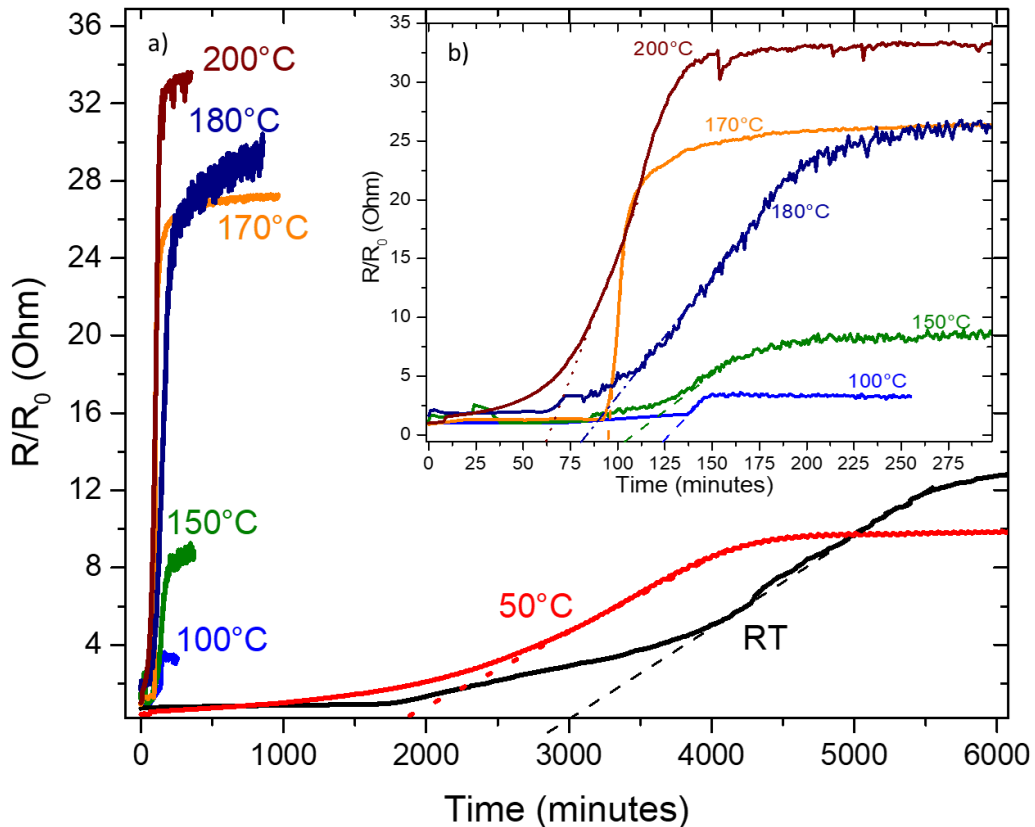
Figure 5-25: Resistance behavior of samples hydrogenated at different temperatures a) room temperature, 50 °C, 100 °C, 150 °C, 170 °C, 180 °C, 200 °C b) only the samples at 100 °C, 150 °C, 170 °C, 180 °C, 200 °C. The respective time of full hydrogenation is marked by dashed lines.

Using equation (19), the activation energy is calculated from the slope of the graph which is equal to slope = -2.02 ± 0.25 cm^2/s with an R^2 = 0.91, showing that the fitted line is close to the experimental data. The activation energy obtained amounts to E_a = 22.56 ± 2.05 kJ/mol and the pre-factor D_0 = 3904.95 cm^2/s obtained from the interception. This value for the activation energy is significantly smaller than the one given by X. Yao et al. [Ya08]. Two explanations are considered at this point, since the data from this work still fit well with other reported individual values: a) in this work the diffusion coefficient is obtained by measuring the growth of the hydride layer thickness and not by measuring directly the diffusion of hydrogen into the hydride phase. A method that can be precise, but limitation in parameters can cause restrictions. b) The preparation of the material in the work of X. Yao et al.

[Ya08] is not given and this might influence the system to some extent. Whereas the thin film deposition allows good purity of the material.

Furthermore, when comparing the activation energy of dehydrogenation to the activation energy of hydrogenation, the latter should be much higher, since it's a process that requires higher temperatures and more energy to take place. A study done by Han et al. showed that the activation energy for the desorption of MgH_2 is equal to 142 kJ/mol. The precision of the measurements described here and the long range of different temperatures evaluated, gives confidence that the obtained activation energy value is within a reasonable range.

In summary, the resistance measurements of this chapter show a precise way to characterize the kinetics growth of the system. The linear growth at the initial stage deviates to a parabolic growth at thicker layers indicating this way that the diffusion of hydrogen through the hydride layer formed closer to the surface becomes slower than the transport of hydrogen through the interfaces. However, clearly something changes for layer of Mg thickness above ≈ 600 nm. The linear fitting at the beginning does not fit as nicely as for the small thicknesses. The exact reason why is not yet clear. The diffusion coefficient of hydrogen into the hydride could experimentally be determined and the average value of the experiments is $D_H^{MgH_2}$ = 6.09 $\cdot 10^{-12}$ cm^2/s at 200 °C, and the activation energy obtained is equal to: E_a = 22.56 ± 2.05 kJ/mol and D_0 = 3904.95 cm^2/s.
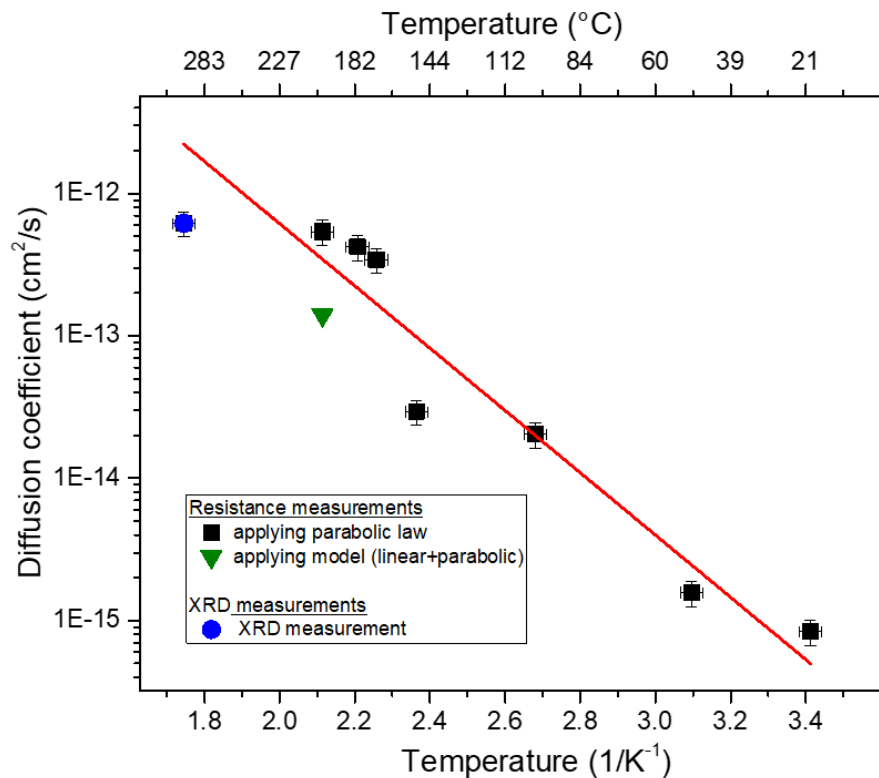
Figure 5-26: Arrhenius linear plot showing the diffusion coefficient over 1/T. Blue circle point obtained by ex-situ XRD measurements, green triangle by applying the model to the resistance measurements at different thicknesses at 200 °C and black squares by applying the parabolic law and using the time of full hydrogenation obtained by the resistance measurements.

5.2.4 Conclusion on hydrogen transport

Following the hydrogenation stage of a sample by TEM, XRD and the measurement of the resistance gives the possibility to quantitatively evaluate the diffusion coefficient of hydrogen in the system at different temperatures. At 200 °C, a shift from linear to parabolic regime is obtained, whereas at 300 °C, a clear parabolic behavior is observed. A model is created to fit the behavior of the resistance change over time during hydrogenation. Considering a linear to parabolic transition, the model is in good agreement to the experimental results up to a specific thickness. At larger thicknesses, a variation in change of diffusion mechanism takes place. A similar variation is also observed for the lower temperatures measurements. A precise explanation of this cannot be given at this time. From the Arrhenius plot obtained experimentally from room temperature to 300 °C, the activation energy and the pre-factor are determined to E_a = 22.56 ± 2.05 kJ/mol and D_0 = 3904.95 cm^2/s respectively. It is important to mention that all this experimental evaluation was done on observations of the first hydrogenation only. The growth kinetics is experimentally characterized by ex-situ XRD measurements and in-situ resistivity changes, and are in a good agreement. Data obtained by the resistance measurements, show minor statistical errors and have demonstrated to be very accurate. Recalling the instability of the Mg/Pd interface over time at high temperatures, it can be concluded that at this stage, during the first hydrogenation at the wide range of temperatures investigated, no negative effect stemming from this intermetallic layer is observed.

5.3 Hydrogen desorption

Until now, samples were experimentally tested only over their first "half cycle" of hydrogenation. From previously discussed results, it is clear that after deposition, all films are columnar with a strong fiber texture and the interface between Mg and Pd is sharp in the as-deposited state. These facts may play a critical role in the process of hydrogen diffusion into (and out of) the system. The columnar structure leads to a diffusion along these elongated grains at the beginning, whereas the equi-axed morphology after hydrogenation will impact the diffusion along the grain boundaries. Furthermore, the sharp interface between Mg-Pd is no longer visible after hydrogenation, meaning that the "catalytic" effect of palladium is no longer fully present in the next cycles. The new Mg-Pd compound will also, most probably, play a role in the diffusion of hydrogen along the layers. These issues were addressed in further dehydrogenation and re-hydrogenation experiments.

For dehydrogenation to take place, one has to reverse the equilibrium of the reaction. To split the hydride into Mg metal and hydrogen, high temperatures and low pressures are required. This has been explained in a previous chapter of this thesis (chapter 3.1.1). Even though dehydrogenation of Mg has been reported to take place at about 300 °C [Do07], as described in chapter 3.1, experimental tests

here were started at 200 °C. This was done in order to investigate whether the nanostructured material investigated here might have a positive effect to lower the temperature of desorption. Therefore, samples were heated up to 200 °C under vacuum (pumping) for a duration double of the hydrogenation time and afterwards characterized by ex-situ XRD, TEM cross sections as well as in-situ resistance measurements.

Resistance measurements during dehydrogenation are presented in Figure 5-27 (a). It can be observed, that dehydrogenation at 200 °C is not complete even after 300 minutes (about twice the time of hydrogenation). The further decrease of resistance seems to be almost negligible at the end and so only a partially dehydrogenated sample is obtained. Considering the EDX spectra obtained in Figure 5-10 that showed the formation of Mg-Pd phases, one may consider that full dehydrogenation was not possible, since part of the Mg already formed Mg-Pd phases.

Re-hydrogenation of the partially dehydrogenated samples was also tested. A typical behavior of such re-partially-hydrogenation is shown in Figure 5-27 (b), where the 2nd hydrogenation is shown in red. Clearly, the trace of the 2nd hydrogenation graph differs significantly from first hydrogenation, showing that the change in morphology after hydrogenation (the loss of the columnar texture) must have an effect on the hydrogenation, since hydrogenation appears to be way faster, with a steep increase from the very first minutes. The model used previously was not compatible to explain this behavior during re-hydrogenation. Further investigation of this effect could not be done at this point, since focus of this work was given at the first hydrogenation. It is however clear that the system behaves differently.
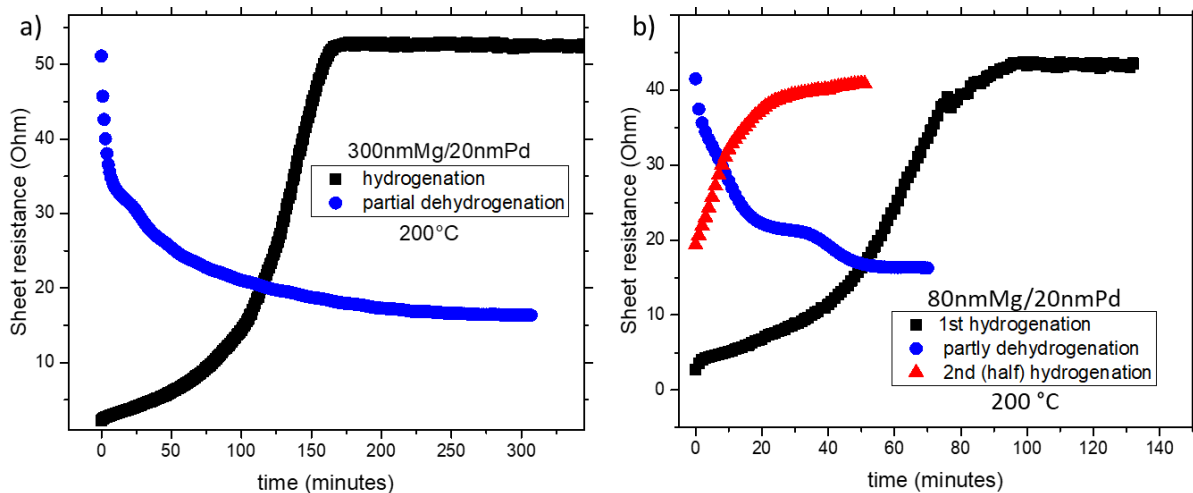
Figure 5-27: Resistance change a) upon hydrogenation (black) at 20 bar and subsequent dehydrogenation (blue) under vacuum, of 300 nm Mg/20 nm Pd layer at 200 °C b) hydrogenation (black), partial dehydrogenation (blue) and re-hydrogenation (red) of a sample of 80 nm Mg/20 nm Pd 200 °C / 20 bar.

Using equation (25) described in chapter 4.3, the amount of hydride remaining in the layer can be estimated using the resistance at each time step.

$$d_{MgH_2}(t) = \frac{\rho_{Mg} \cdot \rho_{MgH_2} \cdot L - w \cdot \rho_{MgH_2} \cdot d_0 \cdot R(t)}{\rho_{Mg} \cdot w \cdot R(t) - w \cdot \rho_{MgH_2} \cdot R(t)} \qquad (25)$$

Figure 5-28 illustrates the evaluated effective thickness change of the hydride layer over time during the dehydrogenation for the two samples shown previously in Figure 5-27. In the evaluation it is considered that the dehydrogenation is also a layer-like reaction. It is demonstrated that the dehydrogenation is far from being complete, since only 3-5 % of dehydrogenation took place. Meaning that in the case of the completely hydrogenated 80 nm Mg sample, only "4 nm" of the hydride were dehydrogenated at 200 °C. Similarly, in 300 nm of Mg, fully hydrogenated, only "9 nm" of the hydride were dehydrogenated at 200 °C.

This also shows the effect of pure Mg on the resistance. The decrease in resistance is remarkable when even less than 10nm of Mg are present in the system. The precision of the resistance measurements to early hydrogenation states is therefore much better than the other techniques used in this work.

Since dehydrogenation is not complete at 200 °C, further tests were completed at higher temperatures. As mentioned in the experimental part (3.4), resistance measurements were not possible at 300 °C since the set-up (especially the golden contact tips – "pogo pin") was not stable at temperatures higher than 200 °C. Therefore, characterization of the dehydrogenated samples at 300 °C were performed by ex-situ TEM cross sections and XRD.
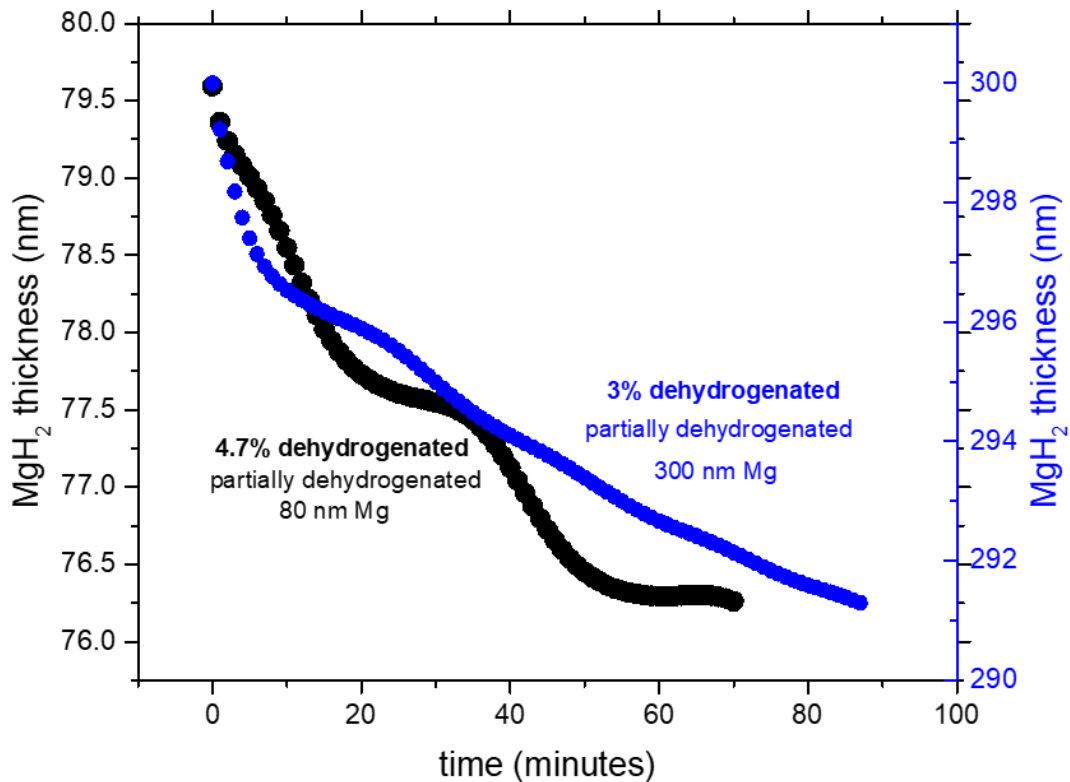
Figure 5-28: Effective "thickness" of hydride in during dehydrogenation of two samples (80 nm and 300 nm) calculated by the resistance change in the layer

Figure 5-29 (a) shows the spectra obtained from four samples: as-deposited, hydrogenated, dehydrogenated and re-hydrogenated. As shown, the strong Mg peak visible at the as-deposited state disappears completely when the sample is hydrogenated. It is also clear that the Mg-Pd phases observed during the first hydrogenation by TEM micrographs in chapter 5.1.3, must have a very small thickness since no peak is visible at the first hydrogenated sample in Figure 5-29 (b). After dehydrogenation the Mg (002) peak appears, though way less pronounced. It is more clearly seen in the magnified intensity scale shown in Figure 5-29 (b), that the films lose their fiber texture since more than one peak now become visible. However, in a much lower intensity than in the as-deposited state. Both Mg peaks (002) and (101) appear after dehydrogenation.

Most importantly however, from these experiments it is possible to identify the nature of the Mg-Pd phases. From Figure 5-29 (b) it is seen that the reaction between Mg and Pd mostly formed Mg_6Pd (orange squares) and Mg_5Pd_2 (green circles). At a 2θ angle of 40 °, it is hard to decide whether any pure Pd phase remained since Pd appears at 40,115 ° and Mg_5Pd at 40,914 °. From the TEM presented hereafter, it is expected that all Pd layers have been transformed into a Mg-Pd phase since no clear Pd layer is observed in the micrographs anymore.

Presence of pure MgH_2 is still visible at the re-hydrogenation, despite the fact that the formation of the Mg-Pd is predominant. This shows that this intermetallic phases (Mg_5Pd and Mg_6Pd) do not block hydrogen diffusion. It is later shown by the TEM micrographs, that these intermetallic phases are formed closely to the surface of the sample and it is possible to remove and re-insert hydrogen through them. Regarding its catalytic activity, nothing was tested at this point in comparison to the pure Pd phase. The fact that it "consumes" Mg, is however, not positive to the use of the system, since the quantity of a hydride is less until all Pd is consumed.

In order to observe a fully dehydrogenated sample, a complete dehydrogenation at 300 °C was performed. Figure 5-30 shows a TEM cross section from such dehydrogenated sample along with the EDX analysis of two different regions. It is clearly seen that the 600nm layer of Mg has transformed to 450 nm of Mg and 150 nm of a mixture between Mg-Pd compounds and pure Mg. The nature of these phases has been identified by the XRD in Figure 5-29 as Mg_5Pd_2 and Mg_6Pd. The Mg_6Pd phase has the highest Mg content of all the intermediate phases in the Mg-Pd phase diagram (see Figure 3-5) and crystalizes with a large face-centered cubic unit cell in the space group F-43m [Ma06]. Its unit cell has a lattice constant of 20.20 Å, in contrast to the Mg and its hydride, which have 3-4 Å lattice spacings. From the EDX however, it is not possible to determine in high precision, whether the phase is Mg_5Pd_2, Mg_6Pd or a mixture of the two plus pure Mg.
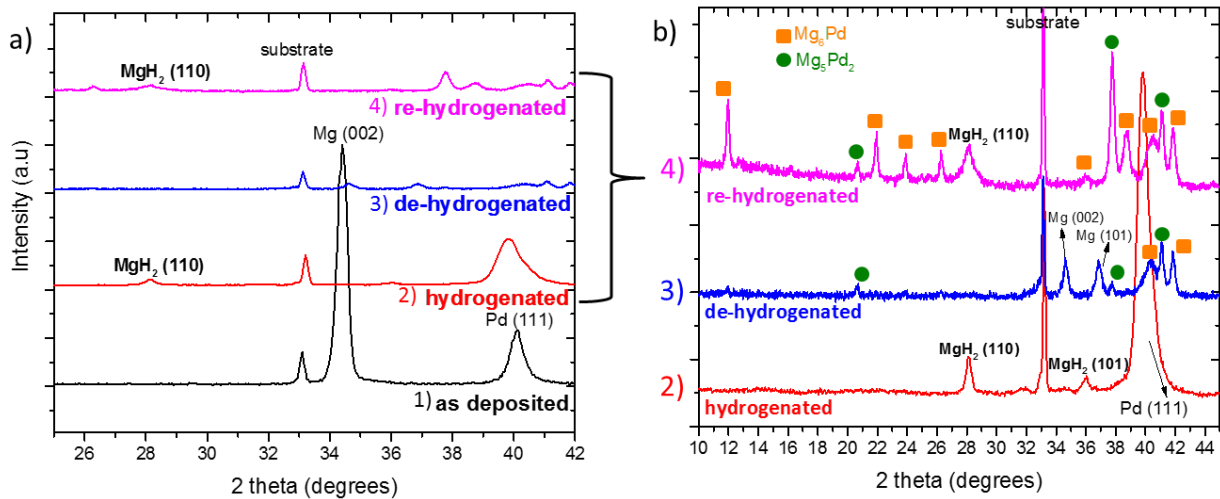
Figure 5-29: a) XRD diffractograms from samples of 400 nm Mg and 20 nm Pd. 1) as-deposited sample, 2) hydrogenated at 300 °C / 20 bar, 3) dehydrogenated at 300 °C, 4) re-hydrogenated at 300 °C / 20 bar. b) Different intensity range of the peaks of the same samples 2), 3) and 4), where the formation of Mg-Pd phases is clearly visible starting from the sample 3) in which dehydrogenation took place.
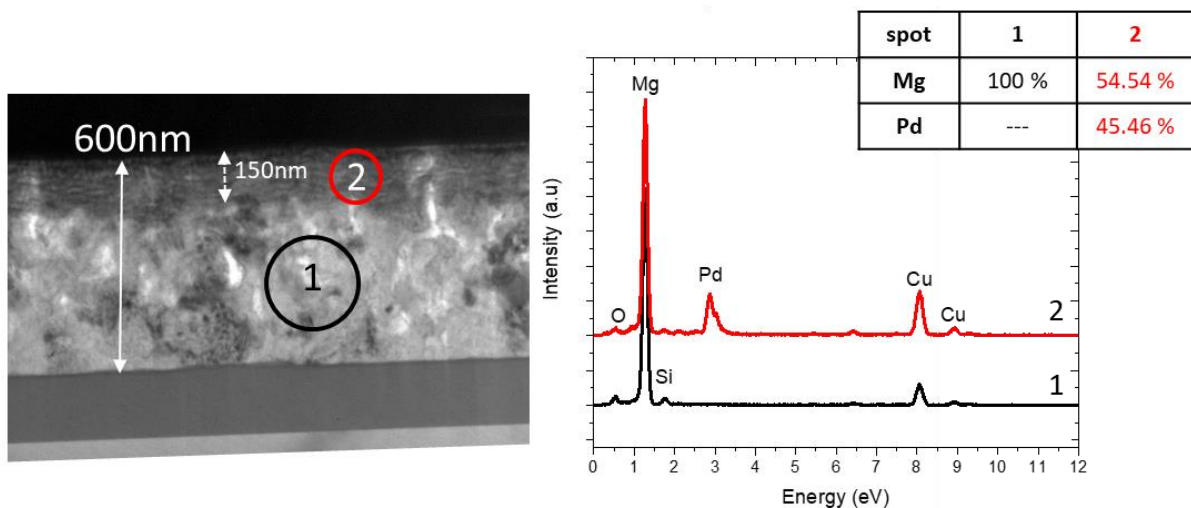
Figure 5-30: TEM micrographs and EDX spectra of a dehydrogenated sample 600 nm of Mg and 20 nm Pd (initially). The quantification of the EDX spectra deliver the Mg and Pd concentrations as stated.

Nevertheless, Table 10 shows the densities of the different compounds and it is clearly shown that the intermetallic Mg_5Pd_2 has a much higher density than all other compounds present in the system. With a value of 4.10 g/cm³ in comparison to ≈ 1.5 - 3 g/cm³ for the other compounds.

When calculating the molar volume of the compounds (V_{molar} = (Molar Mass)/ρ), it is also clear that the volume occupied by one mole of the intermetallic unit is much bigger than the volume of the pure elements. The values in Table 10 are given for standard temperature and pressure.

Considering the size of the sample, the volume of the sputtered layer of Pd (20 nm · 0.5 cm · 3 cm) and the density of the material, the amount of Pd substance in mol can be calculated as:

$$n[Pd] = \frac{m[Pd](g)}{M.M[Pd](g/mol)} = \frac{0.036(mg)}{106.42(g/mol)} = 3.355 \cdot 10^{-7} mol \tag{35}$$

Similarly, the amount of each compound is estimated if all Pd transforms to Mg_6Pd or to Mg_5Pd_2. For example in Mg_6Pd $n[Mg]_{inMg_6Pd} = 6 \cdot n[Pd] = 2.013 \cdot 10^{-6} mol$.

In the particular, the volume that a substance would occupy can be estimated, if all 20 nm of Pd would form this substance. The results of these calculations are displayed in Table 10.

In comparison, Figure 5-31 represents all the crystal structures discussed along with the lattice, their parameters and the volume of the cell.

Table 10: Density of Mg, MgH₂ and Mg-Pd phases. Data obtained by [Cr16a], [Sa72] and [Ma05].

	COMPOUND	DENSITY (g/cm³)	MOLAR MASS (g/mol)	MOLAR VOLUME (cm³/mol)	AMOUNT OF SUBSTANCE (mol)	VOLUME OCCUPIED (cm³)	MASS (g)
1	Mg	1.74	24.30	13.96	--	--	--
2	MgH₂	1.45	26.32	18.15	--	--	--
3	Mg₆Pd	2.95	252.25	85.50	$2.013 \cdot 10^{-6}$	$2.35 \cdot 10^{-8}$	$6.93 \cdot 10^{-8}$
4	Mg₅Pd₂	4.10	334.36	81.55	$1.17 \cdot 10^{-6}$	$1.43 \cdot 10^{-8}$	$5.86 \cdot 10^{-8}$
5	Pd	12.02	106.42	8.85	$3.355 \cdot 10^{-7}$		

Furthermore, white spots spread throughout the layer are clearly visible. These seem to represent pores created within the sample. Supported by literature, these pores are not only caused due to the Mg-Pd phases formed, but mostly due to desorption of hydrogen from the lattice. The formation of porous Mg after dehydrogenation has, indeed, been reported before. Dura et al. measured the hydrogenation and dehydrogenation of thin films of Mg with a Pd layer on the surface using neutron reflectometry [Du11]. It was shown that the Mg films swell in the surface upon hydrogenation and after dehydrogenation the films return to pure Mg, but retain the swelled thicknesses by incorporating voids. The presence of voids has been supported by Mooij et al. [MD13], who reported that the nucleation and growth behavior on hydrogenation and dehydrogenation is asymmetric, because void formation open an alternative transport path to hydrogen. Therefore, the white areas observed in Figure 5-30 can be attributed to such voids that are created upon dehydrogenation. Most likely, they have decisive impact on the second hydrogenation of the system.

In summary, full dehydrogenation of the Pd/Mg films is possible at a temperature of 300 °C. Formation of Mg-Pd alloys and the development of voids inside the material are unavoidable at these conditions. The new phases formed have been identified as Mg_5Pd and Mg_6Pd. The stable new Mg-Pd phases have no negative effect on the re-hydrogenation of the samples, however they consume Mg which can no longer be hydrogenated. These observations demonstrate a severe disadvantage of the Mg system as a hydrogen storage material.

1. Mg
Space Group: P 6 3/m m (#194-1)
a = 3.20920 Å   α = 90.0000°
b = 3.20920 Å   β = 90.0000°
c = 5.20990 Å   γ =120.0000°
V = 46.4680 Å^3

2. MgH₂
Space Group: P 4 2/m n (#136-1)
a = 4.51980 Å   α = 90.0000°
b = 4.51980 Å   β = 90.0000°
c = 3.02500 Å   γ = 90.0000°
V = 61.7965 Å³

3. Mg₆Pd / Mg₈₅Pd₁₄
Space Group: F -4 3 m (#216-1)
a = 20.14500 Å   α = 90.0000°
b = 20.14500 Å   β = 90.0000°
c = 20.14500 Å   γ = 90.0000°
V = 8175.2651 Å^3

4. Mg₅Pd₂
Space Group: P 6 3/m m (#194-1)
a = 8.64400 Å   α = 90.0000°
b = 8.64400 Å   β = 90.0000°
c = 8.16000 Å   γ =120.0000°
V = 528.0199 Å^3

5. Pd
Space Group: F m -3 m (#225-1)
a = 3.89070 Å   α = 90.0000°
b = 3.89070 Å   β = 90.0000°
c = 3.89070 Å   γ = 90.0000°
V = 58.8957 Å^3

Figure 5-31: Crystal structures of Mg, MgH₂, Mg₆Pd, Mg₅Pd₂ and Pd with their lattice parameters and volume of the cell. Data are obtained for each structure from Spring Materials files visualized in VESTA. Yellow, pink and grey represent the Mg, MgH₂ and Pd respectively.

5.4   Conclusion on the Mg/MgH₂ system

Hydride formation in the Mg system has been observed by XRD and TEM. The thermal expansion of Mg is visible and measured in in-situ XRD experiments, while the compressive stresses induced by the hydride are also estimated. The hydride formation starts at about 100 °C. Microscopic imaging of the co-existence of MgH₂ and Mg has been performed using SEM and TEM, showing that during hydro-genation the hydride is directly formed at the interface between the Pd coating and the Mg thin film and grows in a layer-like geometry towards the substrate. Even though electron microscopy perma-nently damages the hydride phase, this experimental technique can, nevertheless, be used to observe the MgH₂ layer growth, since the transition from a columnar grain structure (fiber texture) of the as-deposited Mg thin film to an equi-axed fine grainy structured film indicates the hydride reliably. HRTEM confirms the crystallinity of the formed layers and allows a further validation of the elements present in each layer. The Mg/Pd interface appears to be unstable even during the first hydrogenation.

A comprehensive and reproducible way of following the kinetics of hydride formation is presented and the diffusion coefficients are measured in a wide range of temperatures. Measurements of hydrogena-tion of Pd/Mg layers, as a function of layer thickness and time, were successful. At 200 °C and a maxi-mum thickness of about 600 nm, transport across the Pd/Mg or MgH₂/Mg interface is the limiting

factor. At this point, it is not clear which interface represents the decisive barrier. At larger thicknesses, the linear growth transformed into a parabolic one, where the diffusion of hydrogen through the hydride controls the kinetics. The growth kinetics are experimentally characterized by ex-situ XRD and in-situ measurements of resistivity changes and both are in a good agreement. Data obtained by the resistance measurements, however, show smaller errors and have proven to be more accurate.

The growth constant at 200 °C is measured to be equal to κ= 10^{-12} cm∕s and the diffusion coefficient of H in MgH₂ is $D_H^{MgH_2}$ = 6.18 10^{-13} cm²∕s. At 300 °C, a parabolic regime is observed and the diffusion coefficient amounts to $D_H^{MgH_2}$ = 2.37 · 10^{-12} cm²/s. Successful measurements in a broad range of temperatures gave a value for the activation energy of hydrogen of E_a = 22.6 ± 2 kJ/mol and a pre-factor D_0 = 3904 cm²/s. Figure 5-32 shows a comparison of the results obtained in this work with the sparse literature values of experiments and theoretical work (same as shown in Figure 3-6). The diffusion coefficient is in good agreement with some data reported, in which the growth of the hydride has also been studied at a constant pressure and temperature. The higher diffusion coefficients in comparison to the work of X. Yao et al. [Ya08] may either indicate a principal difficulty with the simulation concept or, probably more interestingly, the decisive influence of grain boundaries in our studies, since the grains during this work appear to be quite small.
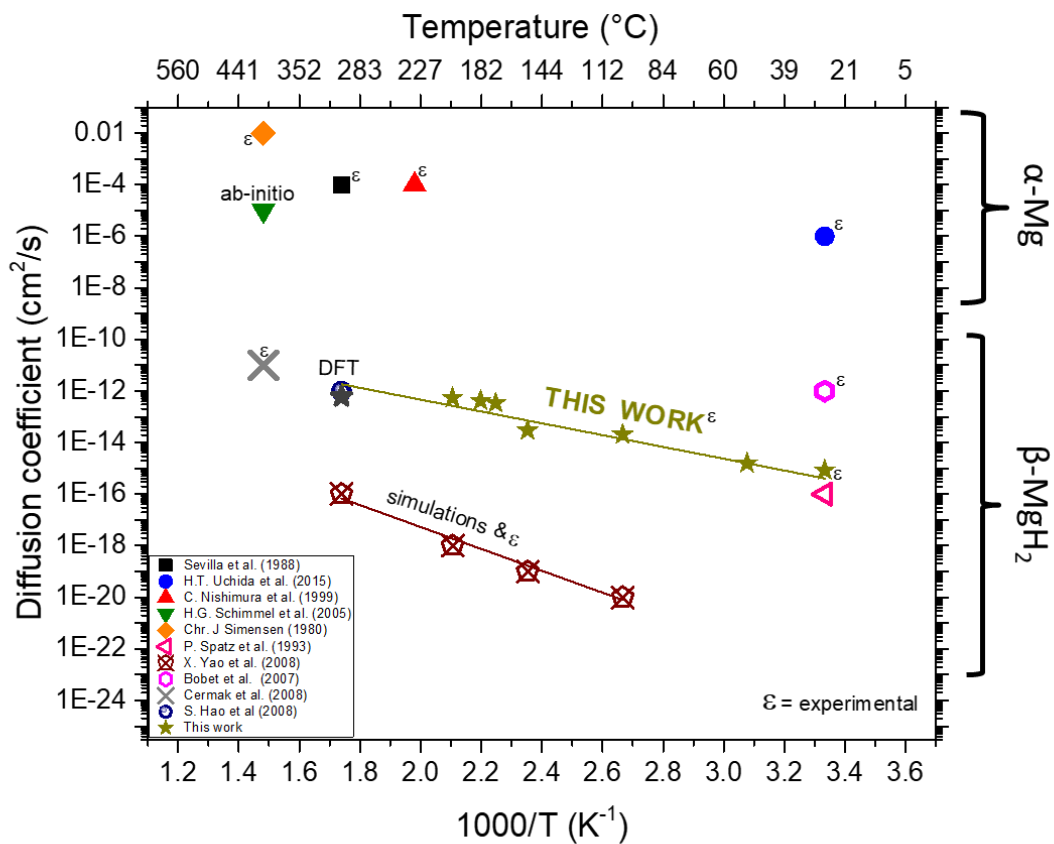
Figure 5-32: Comparison of values on the hydrogen diffusion coefficient of this work with literature (Figure 3-6). Experimental data of this work are shown in stars.

At a temperature of 200 °C, the dehydrogenation of has been possible only to a minimum ≈ 5 % of the layer. The stability of the hydride at this temperature is clear. Complete dehydrogenation of the samples is possible at 300 °C however, with a significant reaction of the Pd layer. The Mg-Pd phases formed are Mg_5Pd and Mg_6Pd and are clearly identified by XRD after dehydrogenation and during re-hydrogenation. The Mg layer has lost its fiber texture over cycling and shows multiple peaks in the XRD after dehydrogenation. Furthermore, during dehydrogenation, voids are created due to the expansion during loading/unloading of hydrogen. These voids have been previously mentioned in literature, but are now clearly visible in TEM micrographs as soon as hydrogen is taken out of the layer.

A comprehensive way to qualitatively follow the kinetics of hydride formation has been presented. A combination of techniques allows a measurement of the diffusion coefficients in a broad range of temperatures and pressures and successfully provides further information on the mechanism of hydrogenation inside the Mg layer.

6   TITANIUM SYSTEM

Titanium, similar to other transition metals, is discussed as a catalyst to accelerate the hydrogenation kinetics of hydrogen storage materials. It is, however, known that H absorption decisively depends on the surface conditions (presence or absence of the natural surface oxide), especially in a material such as Ti, which oxidizes quickly. In this chapter, focus is placed on Ti thin films of controlled thicknesses (50 to 800 nm), that have a natural layer of oxide formed on the surface. These thin films are used as a convenient tool for quantifying the atomic transport. XRD and TEM investigations allow the tracking of the hydrogenation progress inside the film, completed in a similar way as for the Mg system. Hydrogenation of TiO_2/Ti bi-layers is studied at 300 °C for different durations of times (10 s to 600 min) and at varying pressures of pure H_2 atmosphere. A comparison of films with and without TiO_2, the permeation coefficient, as well as a study of the pressure dependence of hydrogenation is discussed in the following sections.

The entire chapter of this work has been published and is available in the Journal of Applied Surface Science [Ha18].

An overview of the samples discussed in this chapter with their experimental characteristics is shown in Table 11:

Table 11: Sample parameters and techniques discussed for the Ti system during this work.

CHAPTER	SAMPLE	THICKNESS (nm)	PRESSURE (bar)	TEMP. (°C)	TIME (min)	TECHNIQUES
6.1/2	TiO_2/Ti	10/ 50 - 800	20	300	7.5 - 125	XRD/TEM
6.3	Pd/Ti Pd/TiO_2/Ti	5/400 5/10/400	1	R.T.	0.1 - 60	XRD
6.4	TiO_2/Ti	10/600	0.05 - 100	300	60	XRD

6.1   The role of surface titanium oxide on hydrogen sorption kinetics

In order to estimate the time needed for full hydrogenation of different Ti thicknesses, the samples were tested in incremental time steps. This allows determining the transition between partially hydrogenated states to the fully hydrogenated state reliably. Figure 6-1 illustrates the XRD diffractogram of 600 nm Ti films of the different stages (a: as-deposited, b: partially and c: fully hydrogenated) of the hydrogenation process. The experimental positions of the intensity maxima of the phases well agree with the literature values indicated by dashed lines. Bragg's peak of α-Ti phase is indicated in black at 2θ = 37.45 ° - 38.14 ° and the one of TiH_2 phase in red at 2θ = 34.47 ° - 35.23 ° / 39.56 °. In the as-deposited state, only the α-Ti (002) peak at 2θ = 37.78 ° is visible due to a significant fiber texture

obtained by the ion beam deposition of the film. An uniaxial texture is the rule in thin film deposition and usually the dense packed planes are aligned parallel to the layer surface [Ga11b]. In the partially hydrogenated Ti film (Figure 6-1 (b), peaks of both the α-Ti$_{(H)}$ solid solution and the δ-TiH$_2$ are seen, while for the fully hydrogenated sample in Fig. 2c, only the δ-TiH$_2$ phase remains visible with TiH$_2$ (111) at 2θ = 34.82 ° and TiH$_2$ (200) at 2θ = 40.42 °. The shift of the α-Ti (002) from 2θ = 38.14 ° to 37.45 ° during partial hydrogenation is explained from the fact that hydrogen introduced interstitially in the matrix causes expansion of the host lattice. Hydrogen solubility of the terminating phase is known to range up to 8.5 at.% [SM87b]. Similarly, the shift of the TiH$_2$ (101) peak position can be explained by the expansion of the lattice parameter, due to the further increase of the hydrogen concentration in the interstitial hydride phase.

In comparison to Mg, which can only form one hydride phase, the MgH$_2$, Ti can form several phases of different stoichiometric composition. This has been discussed previously in Figure 3-7, while from the XRD diffractogram, the shift of the hydride peak is directly observed when more hydrogen is loaded to the system.
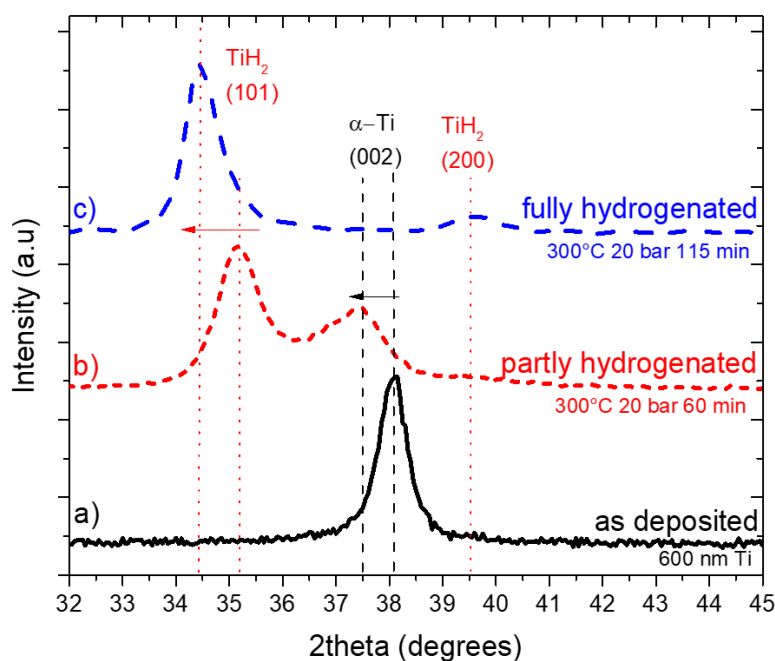
Figure 6-1: XRD diffractogram of (a) as-deposited, (b) partially hydrogenated and (c) fully hydrogenated (at 300 °C / 20 bar) 600 nm Ti film with TiO$_2$ surface oxide naturally created.

The reaction between Ti and hydrogen during the "intercalation" and the formation of the hydride phase was studied by in-situ XRD measurements. This work was performed in collaboration with Dr. Zoltán Bálogh-Michels at the Center of X-ray Analytics EMPA in Switzerland. A mixture of H$_2$:N$_2$ with different compositions as well as different temperatures were used. Thin films of 600 nm thickness of Ti were analyzed with a mixture of 50:50 and 15:85 H$_2$:N$_2$. Figure 6-2 (a) shows the diffractograms in the angular range 2θ = 35 – 39 °, where the Ti peak shifts to lower angles due to the intercalation of

hydrogen into Ti. Later this peak disappears and the corresponding TiH peaks grow. During the inter-calation stage, the peak width of the Ti (002) remains constant, but the position shifts continuously with time. This indicates an efficient redistribution of the H-atoms. During the phase transition, the position of the Ti peak remains stable, as shown in Figure 6-2 (b), but the area of the Ti peak decreases, while that of the TiH phase grows both almost linearly in time as indicated in the graph of Figure 6-2 (c). This linearity might indicate a linear growth controlled by the surface layer. At this point however, there is not enough evidence to decide whether the absorption or the formation of the TiH is the rate-controlling process. The time of full hydrogenation observed here is 110 minutes, at which the Ti peak disappears.
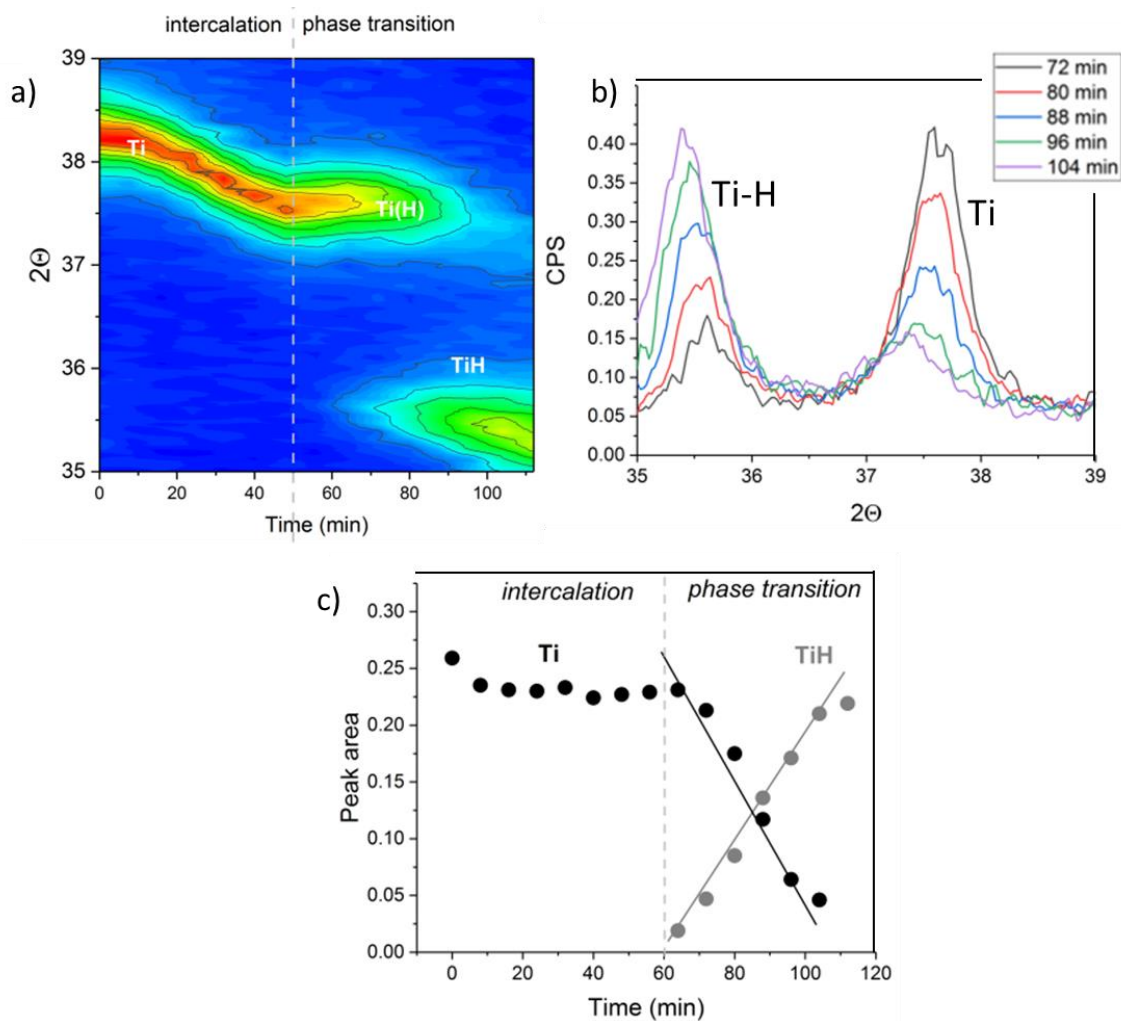
Figure 6-2: a) Evolution of the XRD diffractogram upon hydrogenation b) Quantitative diffractogram, intensity versus scattering angle and c) peak areas clarifying the kinetics.

In order to quantify the absorption kinetics of Ti thin films more accurately, the minimum time to achieve a fully hydrogenated state (as shown in Figure 6-1 (c)) was determined in ex-situ experiments as a function of the layer thickness. The results for hydrogenation of Ti films with the natural surface oxide at 300 °C and 20 bar H_2 atmosphere are presented in Figure 6-3. At the studied temperature and pressure, a linear relation of the hydrogenation depth versus time is identified in Figure 6-3 (a) with a

slope of (5.83 ± 0.24) nm/min. This implies that the phase transformation is controlled by a fixed kinetics barrier, rather than the varying diffusion length within the forming hydride.
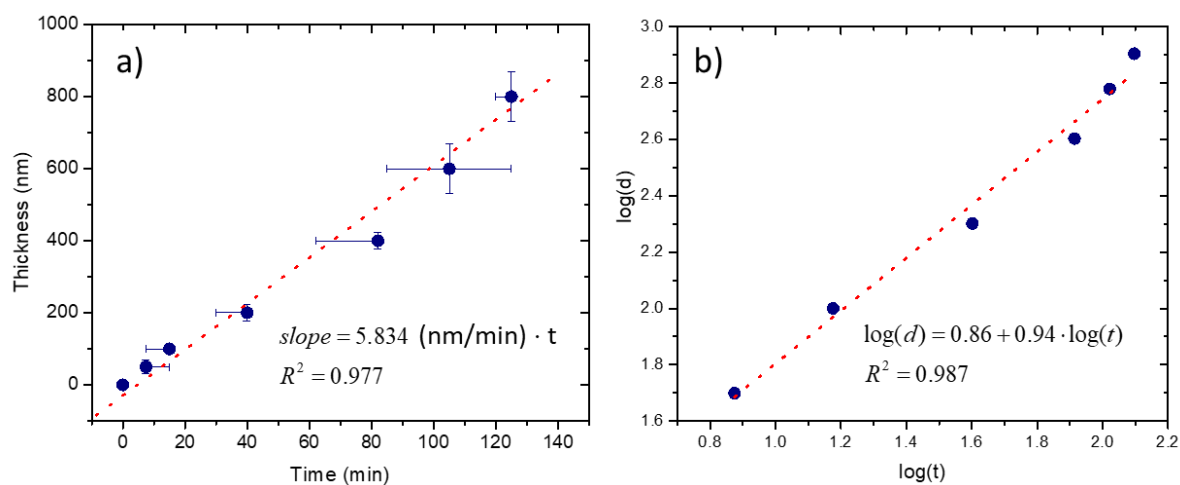
Figure 6-3: a) Ti thickness of (TiO$_2$)10 nm/(Ti)x nm versus time of full hydrogenation at 300 °C / 20 bar. b) Double logarithmic plot points out the proportionality between thickness and hydrogenation time.

As an additional verification, the double logarithmic plot of the thickness versus time clearly identifies the kinetics exponent of x = 94 ≈ 1 as shown in Figure 6-3 (b). The error bars on the x-axis are determined from samples that were found to be partially hydrogenated when tested for slightly less time. The error bars in the y-axis represent the possible variation in the thickness that might occur from the different position of the substrates with respect to the target during sputter deposition.

In order to clarify the microstructural evolution during the hydrogenation, TEM micrographs were taken at different stages. Figure 6-4 presents cross sections of the three stages in correspondence to the XRD diffractograms of Figure 6-1. Figure 6-4 (a) shows the as-deposited α-Ti state, Figure 6-4 (b) partially hydrogenated stage and Figure 6-4 (c) the fully hydrogenated state. The characteristic diffraction patterns of the two phases are presented in Figure 6-4 (d-f). Expected reflection positions are indicated by semi-circles on the right hand side. The interface between the metal and the hydride phase is indicated by a dashed line. Its exact position was localized by micro-diffraction at different positions. Furthermore, the Ti layer is covered by the natural oxide layer, which can be seen in all micrographs. In the enlarged view of Figure 6-4 (a), taken at the as-deposited state, the average thickness of the natural oxide formed at room temperature amounts to ≈ 9.8 nm. Based on the diffraction pattern in Figure 6-4 (f), it is identified as rutile TiO$_2$ [R.95].

Remarkably, Figure 6-4 (b) demonstrates that the hydride layer nucleates heterogeneously at the backside interface close to the substrate, and only afterwards does it grow towards the layer surface from where the hydrogen is loaded. At first sight, this peculiar behavior, especially demonstrates the faster diffusion of H in Ti thin films once the TiO$_2$ barrier at the surface has been broken, which leads to a practically homogenous hydrogen distribution within the Ti layer.

The presence of TiO_2 has only been observed in this work by TEM micrographs. In the XRD, no evidence of the presence of an oxide could be found, despite many attempts. The TiO_2 rutile peaks should appear at 2θ =27.44, 2θ = 36.086 and 2θ = 41.226 for (110), (101) and (111) orientations respectively. A possible explanation for this might be the fact, that the very thin layer is furthermore randomly oriented polycrystalline as also proven by the SADP in the TEM. This would give rise to particularly low intensities. By contrast, the sputtered film of 10 nm of Pd is visible in the XRD, since the layer has a texture and Pd has a rather large scattering factor that contributes to the peak intensity of the material in the XRD.

By comparing Figure 6-3 with Figure 2-5, in which a linear kinetics law has been described, clear evidence is derived that the hydrogenation here follows a linear growth law, too. Adapted to such linear kinetics regime and a layer like reaction as discussed in chapter 2.2.1 , the appropriate description of the growth rate of the hydride is given by equation (30), previously shown for the hydrogen transport in Mg at 200 °C:

$$\frac{d\Delta x}{dt} = \kappa \frac{\Delta \mu_H}{RT} \tag{30}$$

In order to calculate the driving force as the difference of the chemical potentials to both sides of the controlling barrier, presumably the oxide layer, the following needs to be considered:
$\Delta \mu_H = \mu_H - \mu_{Me-H}$ with $\mu_H = \mu^0 + \frac{RT}{2} \ln \frac{p_{H_2}}{p^0} + \frac{\partial \mu^0}{\partial T}(T - T^0)$. In the exact same way as described for the Mg

page in chapter 5.2, the chemical potential of hydrogen is established by the applied gas pressure. The same formula may be used to determine the hydrogen chemical potential μ_{Me-H} of the terminal solution in equilibrium to the hydride phase, if the appropriate equilibrium pressures are inserted. The equilibrium pressure of hydride formation at 300 °C, p_{eq} = 0.01 bar, can be read from published PCT-curves of the Ti-H system shown in Figure 3-8 before. (The constant μ_0 and its derivative drop out when calculating the difference). The so calculated driving force amounts to $\Delta \mu_H$ = 180.18 kJ/mol at 300 °C and 20 bar hydrogen pressure. For an illustration of the thermodynamic situation, Figure 2-2 shows the change of the chemical potential across the interface. The value of the driving force in the case of Ti is significantly larger than in the case of Mg.

From the experimental data in Figure 6-3 and the evaluated slope, the respective transport coefficient of Ti coated with the natural surface oxide amounts to κ = 2.57 ±0.11 ·10^{-10} cm/s.

Figure 6-4: TEM bright field images of Ti thin film cross sections of a) and a') as-deposited, b) partially hydrogenated, c) fully hydrogenated (at 300 °C / 20 bar) with corresponding diffraction patterns of selected areas: d) α-Ti e) TiH$_2$ and f) rutile TiO$_2$ phases [Ha18].

Additional characterization was done to clarify the time of full hydrogenation at a lower temperature than 300 °C. Figure 6-5 shows the XRD characterization of these samples. 400nm Ti thin films were hydrogenated at temperatures between 250 °C and 300 °C. At temperatures lower than 280 °C, the hydrogenation of the samples was not possible within a reasonable time. A peak shift of the Ti peak is observed for temperatures 250 – 270 °C, indicating the initial interstitial hydrogenation, but full hydrogenation of samples at lower temperatures was too slow to be considered for measurement.
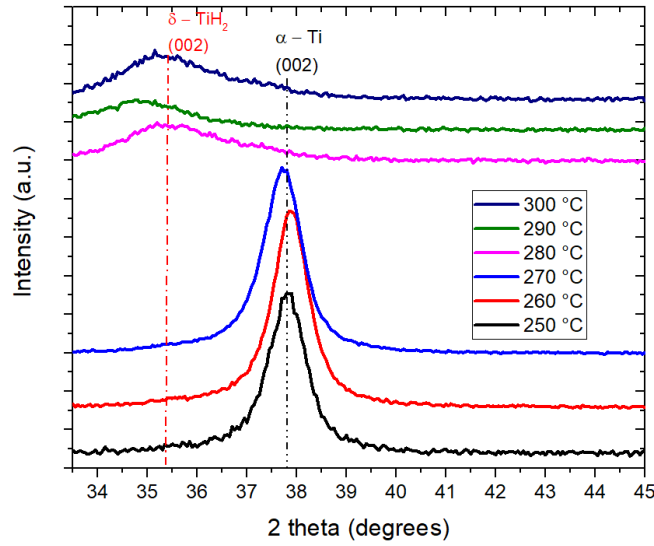
Figure 6-5: XDR diffractograms of 400 nm Ti thin films on Si substrates hydrogenated at 20 bar for 120 min.

6.2   Permeability coefficient

From the experiments described so far, the role of the surface oxide shows to be dominant. The amount of hydrogen diffusing through this oxide over time is therefore of great importance. The critical parameter is known as the permeability and from the above-mentioned experiments, it is possible to determine the permeation coefficient of the oxide layer.

From the experimental data in Figure 6-3 and the evaluated slope, the respective linear growth coefficient of Ti, coated with the natural surface oxide, amounts to $\kappa = 2.57 \pm 0.11 \cdot 10^{-10}$ cm/s. Provided the diffusion through the oxide layer of constant thickness represents the controlling kinetics barrier, the determined growth coefficient may be further interpreted in the following way: The growth of the hydride phase in TiH$_2$ stoichiometry requires a flux of hydrogen of:

$$j_H = 2\rho_{Ti}\frac{d\Delta x}{dt} \xrightarrow{equation(9)} 2\rho_{Ti}\kappa\frac{\Delta\mu}{RT} \tag{36}$$

On the other hand, the diffusional flux through the oxide is given by:

$$j_H = M\frac{\Delta\mu}{w_{TiO_2}} = \frac{c_H^{TiO_2}(1-v_H^{TiO_2})}{RT}D_H^{TiO_2}\frac{\Delta\mu}{w_{TiO_2}} \tag{37}$$

if the appropriate expression for the mobility M of an interstitial solution is used. (Here and in the following, atomic fractions are expressed by the symbol v, while the symbol *c* is used for concentrations per volume.) The hydrogen content in the oxide is not exactly known, but it is certainly expected to be lower than in the Ti metal, so that reliably $1 - v_H^{TiO_2} \approx 1$. Combining equations (36) and (37), the permeation coefficient of the oxide layer can be derived as the application-relevant material property that can be determined here:

$$p_H := c_H^{TiO_2} D_H^{TiO_2} = 2\rho_{Ti} w_{TiO_2} \kappa \qquad (38)$$

With the measured thickness of the oxide layer in the TEM micrographs, w_{TiO2} = 9.8 ± 0.2 nm and the density of Ti, ρ_{Ti} = 5.66 · 10^{22} cm^{-3}, the permeation coefficient is quantified to: p_H = 2.9 ·10^7 ± 0.5 cm^{-1}·s^{-1} at 300 °C.

If the surface reaction or the transfer across the TiO$_2$/Ti interface controlled the reaction, the stated value would still represent a reliable lower limit to the permeability of the oxide. Even if the hydrogen concentration is assumed unrealistically high, e.g. as that of the metal atoms in rutile (5·10^{22} cm^{-3}) the hydrogen diffusivity in the oxide would still amount to $D_H^{TiO_2}$ ≥ 10^{-15} cm^2/s. Thus in view of the presented experiments, the lower ones of the data points reported in literature for the oxides in Figure 3-9 (triangles) appear somewhat doubtful.

6.3   Ti thin films coated with Pd
Influence of the surface oxide layer (25 °C/1 bar)

A linear kinetics, meaning a constant reaction rate, could only be explained by: i) a slow splitting of hydrogen molecules, ii) slow insertion of H atoms into the oxide, iii) slow transport through the oxide layer of constant thickness or iv) slow transfer from the oxide into the Ti layer. In order to verify whether the splitting of H$_2$ molecules into atomic hydrogen at the TiO$_2$ surface may represent the rate limiting process of the phase transformation, a comparison is done between Ti thin films with their natural oxide on top and samples that were additionally coated with Pd. As previously mentioned, Pd offers a catalytic effect to the splitting of H$_2$ molecules. Furthermore, it prevents further oxidation of Ti reliably. So, without breaking the vacuum, Ti layers of 400 nm in thickness were additionally coated with a thin Pd layer of 5 nm. This way, the formation of the surface oxide is avoided and transport through the Pd/Ti bilayer is investigated. For direct comparison, samples of Pd/TiO$_2$/Ti layers were also prepared, that again require a transport through the oxide layer, but allow fast splitting of the hydrogen molecules.

Figure 6-6 (a) shows the XRD characterization of the as-deposited state of the Pd/Ti bilayers, while Figure 6-6 (b) presents the fully hydrogenated state. Remarkably, the latter is already obtained at room temperature and at the lower pressure of 1 bar. Clearly, only a TiH$_2$ peak is visible. The required time

for full phase transformation is estimated to be less ≈ 10 seconds. This is much faster than the reaction in the triple layer Pd/ TiO₂/Ti that is shown in Figure 6-6 (c). In this case, at room temperature, no hydrogenation appears at all. Even after 60 min of exposure at 1 bar, the XRD spectrum looks exactly as the as-deposited state. It is therefore obvious, that in presence of a surface oxide, a drastically de-celerated kinetics, require much higher activation temperatures to transform Ti to TiH_2. For full hydro-genation, in the time scale of hours, about 300 °C is necessary. Furthermore, the experiment identifies the transport of H through the TiO_2 or its interfaces as the rate-limiting step, as hydrogen in atomic form is already offered efficiently by the coating with Pd.
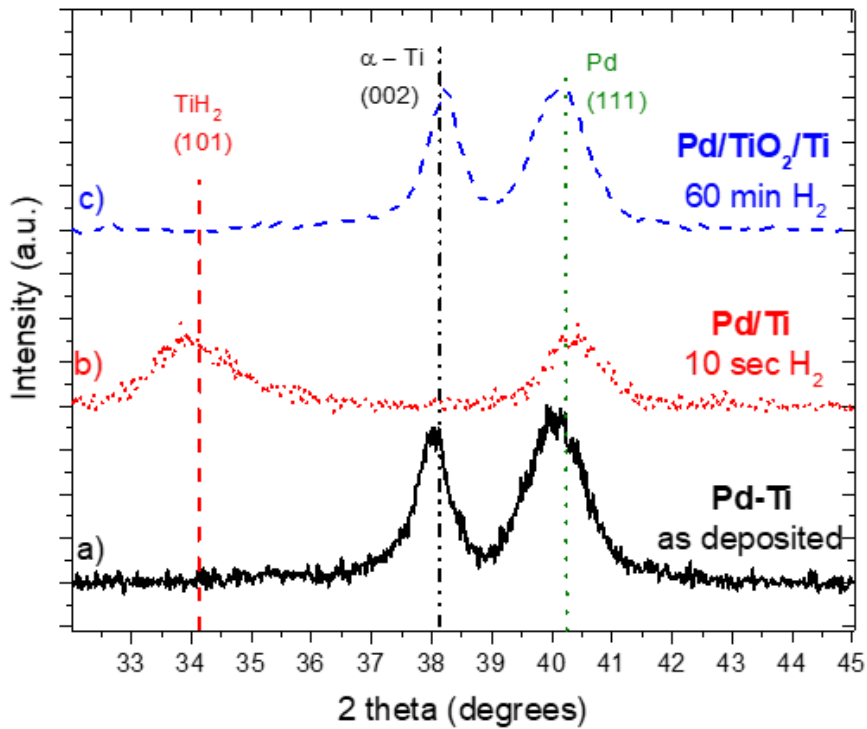
Figure 6-6: XRD diffractograms of as-deposited Pd-Ti (A), fully hydrogenated Pd-Ti (B) and not hydrogenated at all (at 18 °C and 1 bar hydrogen atmosphere) Pd-TiO₂-Ti thin film (C). Expected peak positions of the α-Ti (black dashed line), TiH₂ (red dotted line) and Pd(green dotted line) phase are marked.

Furthermore, the observed fast reaction in the Pd/Ti sample allows deriving a reliable lower limit to the diffusion coefficient of hydrogen in the hydride. Assuming a layer geometry, the hydrogen flux through an already formed hydride of thickness Δx and thus, the further growth of the hydride layer is expressed as:

$$\frac{d\Delta x}{dt} = \frac{\Omega_{Ti}}{2} j_H = \Omega_{Ti} \frac{1-v_H}{v_H} D_H^{TiH_2} \frac{\Delta c_H}{\Delta x} = D_H^{TiH_2} \frac{1}{v_H(1-v_H)} \frac{\Delta v_H}{\Delta x} \tag{39}$$

in which Δc_H and Δv_H denote the compositional width of the TiH_2 phase field in the phase diagram in concentration per volume and in atomic fraction, respectively. Integration of the latter equation leads to:

$$D_H^{TiH_2} = \left(\frac{(1-v_H)v_H}{\Delta v_H} \right) \left(\frac{x^2}{2t} \right) \tag{40}$$

Regarding the actual phase boundaries of TiH$_2$ in the phase diagram [SM87c] (v$_H$ ≈ 0.6, Δv$_H$ = 0.15) [LIJ], quantifying with x = 400 nm and t = 10 s, the minimum diffusion coefficient is determined to D_H^{Ti} ≥ 1.6 · 10^{-10} cm^2/s at room temperature, which well confirms recent literature data of Qin et al. shown in Figure 3-9. It is therefore implicit, that the hydride can be nucleated at the surface if no TiO$_2$ is present.

6.4 Pressure dependency

During the experiments, an unexpected observation was made while hydrogenating the samples at different pressures and therefore a deeper study was of interest. With regard to equations (12) and (17), the driving force Δμ$_H$ is an important factor in both kinetics regimes (linear or parabolic). Δμ$_H$ is shown in equation (31) to depend on the pressure and more precisely, according to the equation, it should increase with the gas pressure. Therefore, the hydrogenation is expected to be naturally affected by a variation of the hydrogen pressure.

The focus was therefore, placed on observing the pressure dependence. A considerable pressure range could be studied, which allowed quantitative experimental data analysis. By keeping temperature and annealing time constant, but varying the pressure of the gas atmosphere, the hydrogenation rate of the surface oxidized samples has been measured. For this, the temperature and annealing time have been chosen to 300 °C and 60 min respectively, so that a partially hydrogenated state is always established, which can be quantified by comparing the relative peak intensities in the diffractograms. In Figure 6-7, the measured fraction of the hydride intensity is plot in linear (b) and logarithmic (a) scale. In Figure 6-7 (a), a clear plateau of constant rate for pressures higher than 1 bar is observed, while Figure 6-7 (b) shows the increase at rather low pressures more clearly. Therefore, it can be seen that the reaction rate reaches a saturation at which a further increase of the chemical potential of hydrogen and thus increase of the driving force does not accelerate the hydrogenation anymore.
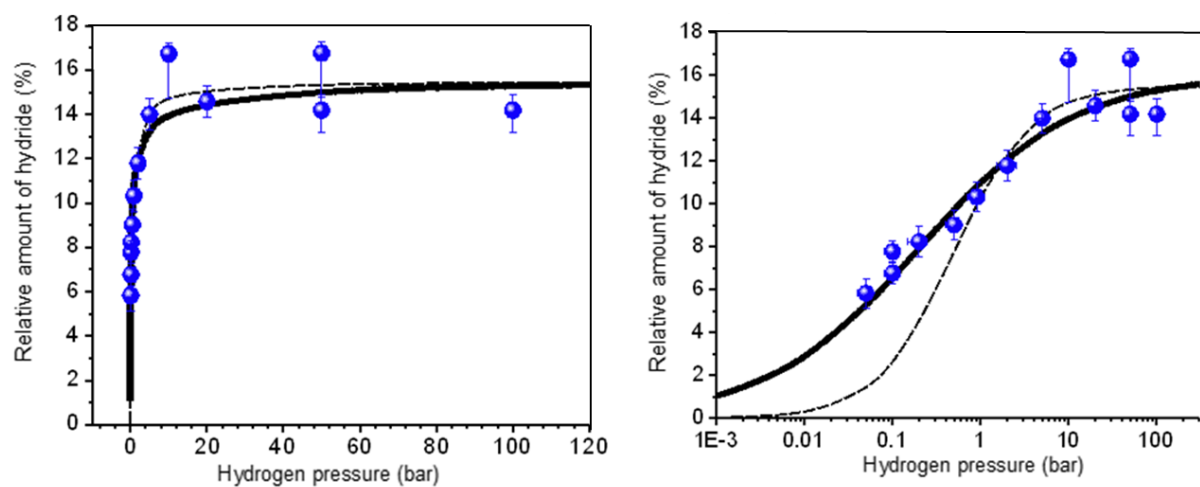
Figure 6-7: Ratio of peak intensities (TiH$_2$/TiH$_2$+α-Ti) as a function of pressure, determined from XRD diffractograms of partially hydrogenated samples of 600 nm Ti films, at 300 °C/60 min, a) logarithmic and b) linear time scale.

In order to interpret this at first sight unexpected behavior, a basic potential landscape may be considered for the hydrogen atoms as sketched in Figure 6-8. Although, details of the molecule splitting and the transition between physisorption and chemisorption were neglected. The scheme is sufficient to understand the experimental observation when combining kinetics and thermodynamic arguments. Important in this case is the different height of the two activation barriers that hydrogen atoms have to overcome. On the one hand, between the ideal gas and the chemisorption sites at the TiO_2 surface (Q^{ads} - small) and on the other hand, between these surface sites and the Ti bulk (kinetics barrier - large). For this consideration, it does not matter whether the large barrier stems from jumps across one of the interfaces or, in view of the experiments mentioned before more probably, from the slow diffusion through the oxide layer. Here, it is only important that thermodynamic equilibrium between the gas phase and the chemisorption sites is assumed. Rate kinetics arguments however, still hold when discussing the transition from the adsorption to the metal bulk sites.

To cast this into formal expressions, Langmuir's adsorption model is considered. Langmuir demonstrated experimentally, that a given surface, in this case that of the oxide, has a certain number of equivalent sites to which species (hydrogen) can "stick" (either by chemisorption or physisorption).
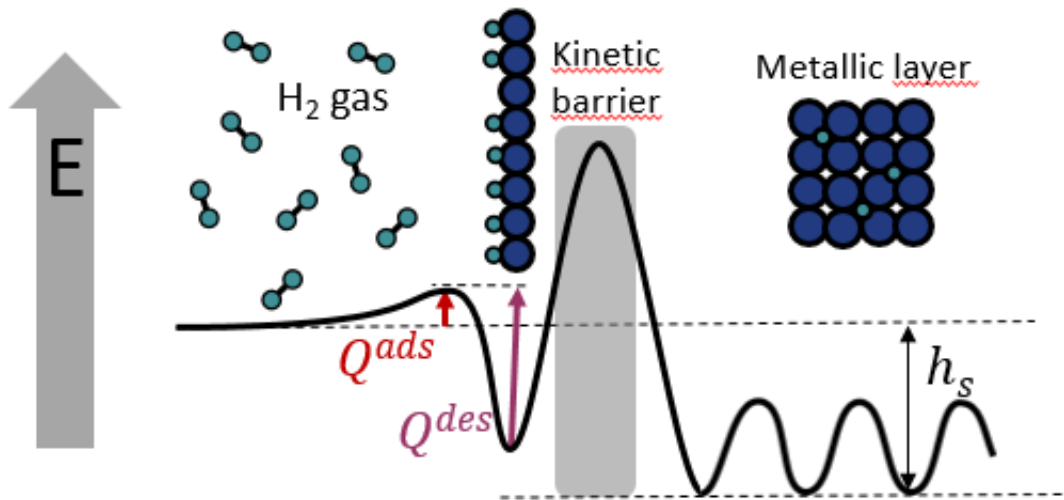
Figure 6-8: Schematic representation of the potential landscape.

Based on the assumptions that a) the surface of the oxide is a perfectly flat plane, b) it's completely immobile for hydrogen to diffuse in, c) all sites are equivalent, d) each site can hold at most one hydrogen atom and e) there are no interactions between hydrogen and the sites, the rate equations for the surface coverage and the flux from the surface into the layer volume can be derived:

$$\frac{d\Theta}{dt} = \frac{2S}{\rho_A} \cdot \frac{p}{\sqrt{2\pi mkT}} (1-\Theta)^2 \exp\left(-\frac{2Q^{ads}}{RT}\right) - \nu_0\Theta^2 \exp(-\frac{2Q^{des}}{kT}) - \frac{j_H(\Theta)}{\rho_A} \tag{41}$$

$$j_H = \rho_A\Gamma_0\Theta(1-\nu_H)\exp(\frac{h^{ads}}{RT}) - \rho_A\Gamma_0\nu_H(1-\Theta)\exp(h^S) \tag{42}$$

in which S, p, m, ρ_A, v_0, Γ_0 and v_H denote a sticking coefficient (unit-free, S ≤ 1), pressure and mass of the H_2 molecules, areal density of adsorption sides for single H atoms, an attempt frequency similar to Debye frequency, the average frequency of diffusional jumps and the atomic fraction of hydrogen on the volume interstices, respectively. The activation energies in the exponents are defined in the sketch (Figure 6-8), which also fixes the adsorption enthalpy $h^{ads} = Q^{des} - Q^{abs}$, while the solution enthalpy h^s is defined in the figure according to its usual meaning too. In the order of their appearance, the three terms on the right hand side of equation (41) describe the impingement and successful splitting of H_2 molecules, re-desorption of H_2 into the gas phase and the drain of hydrogen atoms into the bulk. The squares in the surface coverage and the factors 2 before the activation energies reflect the fact that a hydrogen molecule needs to split into two H atoms. The two terms on the right hand side of equation (42) describe the balance between ingoing and outgoing hydrogen jumps. In both, the frequency of successful site exchanges needs to be proportional to the number of the available hydrogen atoms on the initial side and the available vacant sites at the final side.

In the considered situation, assuming the drain flux into the volume much smaller than the re-desorption rate, neglecting the last term on the right hand side of equation (42), it is found that the steady state of coverage is:

$$\text{R}T \ln\left(\frac{\Theta}{1-\Theta}\right) = \frac{\text{R}T}{2}\ln\left(\frac{2S}{\rho_{Av_0}\sqrt{2\pi mkT}}\right) + h^{ads} + \frac{\text{R}T}{2}\ln p := \text{R}T \ln\sqrt{\frac{p}{p^*}} \tag{43}$$

With p*, introduced in the last equation as the partial hydrogen pressure in equilibrium to a half-covered surface. This parameter is a convenient abbreviation that absorbs most of the variables of the former expressions, but it also has a clear physical meaning. Due to the non-equilibrium situation, which is evidenced by the observed linear reaction kinetics, the second term at the right hand side of equation (42) is negligible. Furthermore, the atomic fraction n_H is fixed by the two phase equilibrium between the terminal solution and the hydride phase. So, it can be expected that the drain flux and thus the hydrogenation rate being simply proportional to the surface coverage. Rearranging equation (43), it is found:

$$j_H \propto \Theta = \frac{\sqrt{p}}{\sqrt{p^*} + \sqrt{p}} \tag{44}$$

which naturally leads to saturation at high pressures as required for a physically correct description, since the coverage is bound by the maximum value of one. Equation (44) is expected to describe the variation of the hydrogenation rate with the pressure. This is, indeed, confirmed by the solid lines presented in Figure 6-7 (b). They were calculated by equation (44) with p* = 0.21 ± 0.03 bar as the optimum fit parameter. Exceeding this characteristic pressure does not significantly accelerate the hydrogenation anymore. For comparison, the dashed lines represent a function similar to equation (44) but with the square root dependence on pressure replaced by a direct proportionality. In this case, the

slope at low pressures is clearly inconsistent with the measured data. Such linear dependence would be indicative for a dissociation-controlled reaction, which the presented experiment therefore rules out. Obviously, the proposed interpretation by a permeation-controlled reaction is more appropriate here.

6.5   Conclusion on the Ti/TiH$_2$/TiO$_2$ system

Hydrogenation of Ti coated by a natural surface oxide has been studied quantitatively at technically significant pressures of several bar. To measure the kinetics of the reaction, the critical time to fully transform thin Ti films into the hydride TiH$_2$ has been determined by XRD, confirmed by cross section TEM micrographs and evaluated as a function of the layer thickness. The following facts can be summarized and have already been published by Hadjixenophontos et al. [Ha18]:

Sputter-deposited Ti thin films naturally oxidize at the surface to rutile TiO$_2$ to a thickness of 9.8 nm on average, in ambient atmosphere and at room temperature. Thin films of Ti, covered with the natural oxide, at 300 °C show a reasonable hydrogenation rate for pressures ranging from 0.05 to 100 bar. The hydrogenation kinetics at 20 bar is linear in time, indicating a barrier controlled reaction. The hydride grows in a layer-like geometry, being nucleated remote from the surface. The linear growth coefficient amounts to κ = 2.57·10^{-10} cm/s and the lower diffusion limit of H in Ti is equal to D_H^{Ti} ≥ 1.6·10^{-10} cm^2/s at 300 °C. Under the reasonable assumption that the slow diffusion through the oxide layer is rate limiting, the permeation coefficient of hydrogen in TiO$_2$ amounts to $p_H^{TiO_2}$ = 2.85·10^7 cm^{-1}·s^{-1}. Pd/Ti bi-layers preventing oxide formation and Pd/TiO$_2$/Ti triple layers were compared in terms of their hydrogenation reaction. While the not-oxidized system hydrogenates immediately, even at room temperature, the triple layer containing the oxide barrier again needs a temperature of 300 °C to present reasonable hydrogenation rates. This direct comparison demonstrates on the one hand the high impact of the kinetics barrier that is introduced by the oxide. On the other hand, it also shows that it is not the splitting of the H$_2$ molecules at the oxide surface, but the transport of hydrogen atoms through the oxide that provides the decisive rate-controlling factor. Lastly, with the oxide on the surface, the hydrogenation rate first increases with the pressure, but reaches a saturation level at about 1 bar from which no further acceleration is obtained even with increasing pressure. This behavior is quantitatively understood by the full occupation of available surface sites on the oxide. At 300 °C, the critical pressure at which half of the surface sites become occupied by hydrogen amounts to *p** = 0.21 bar.

7   MAGNESIUM HYDRIDE AS A BATTERY ELECTRODE

During this work, a close collaboration with a partner of the ECOSTORE ITN project was created with the purpose of studying the structural changes in MgH_2 thin film electrodes during lithiation. Samples were prepared by Ana Lacoste in France (LPSC Grenoble), cycled in a liquid battery cell by Dr. Nicola Berti in ICMPE - CNRS Paris and sent to the University of Stuttgart for further structural investigations. The results of these studies will be briefly presented hereafter.

Finding alternative electrodes for Li-ion batteries with high energy density and better lifetime is an indispensable need caused by the increase of electronic devices in modern society. Metal hydrides have the capability to react with Li at low potentials and low temperatures (R.T.) and furthermore, appear to have capacities of thousands of mAh/g, making them promising candidates as negative electrodes in Li-ion batteries. Among the hydrides, MgH_2 attracts great interest. However, its irreversibility is still a critical issue that hinders application. As a conversion reaction electrode, its volume expansion is unavoidable, although this seems not to be the primary problem. Previous reports on powder metal hydrides [SCL16] attribute the poor reversibility to the loss of electronic contact, to the low conductivity inside the electrode and to the cracks formed due to volume changes during cycling. These aspects are, however, hard to accurately determine in powder geometry. Thin films provide a well-defined structure that allows investigating the effect of lithiation on the electrode more precisely.

XRD and TEM analyses were carried out in order to study the conversion reaction path and the electrode morphology in the first discharge/charge cycle. Focus is placed on the first cycle in order to see step by step what happens inside the electrode when Li is inserted.

7.1   Electrochemical tests

Magnesium hydride films with a thickness of 1 μm were deposited on copper foils by radio frequency sputtering with continuous microwave radiation in order to enhance ionization. The thin films have been studied as positive electrodes in Li-ion half-cells. Galvanostatic cycling tests made by Dr. Nicola Berti have shown that the electrochemical reactivity of MgH_2 thin films strongly depends on its surface, since Mg oxides form very fast [Ni18]. Indeed, thin films covered with a 13 nm-thick layer of aluminum (Al) undergo a conversion reaction with lithium during the first discharge, whereas uncovered thin films have limited reactivity, due to the oxide formed on the surface. Nicola Berti et al. [Be17], showed that uncovered MgH_2 electrodes need an activation process before the conversion reaction takes place, suggesting the presence of a passivation layer on the surface of the electrode. The deposition of Al-protective layer hinders MgO formation and facilitates the reaction of MgH_2 with Li. Furthermore, Al is shown to have no electrochemical reactivity with Li, even though AlLi or Al_2Li_3 can be formed even

at room temperatures. Aluminum is also an element that oxides quickly in air, however, its oxide allows movement of Li and therefore it causes no problems to the cyclability of the cell [Ni18]. Successful cyclability of the cells however, shows that Al allows Li ions to diffuse through the thin layer into the hydride without further complications.

In a chrono-potentiometry experiment (CP), such as done for the samples investigated in this case, the sample is exposed to a constant current flowing between the working (hydride) and the counter elec-trode (Li metal). The recorded potential response is obtained as a function of time, as illustrated in Figure 7-1. When an anodic current is applied, the potential increases, whereas for cathodic currents the potential will decrease. The current flowing in the cell is controlled during the measurements by the measured potential between the working and a reference (Li metal) electrode and is stopped when a voltage of 0.1 V is reached. This limit has been chosen since previous experimental investigations revealed that at potentials lower than 0.1 V, Mg alloying reactions with Li are dominant [Ou08]. In order to study the hydride conversion reaction, this alloying reaction was avoided by fixing the cut-off potential at 0.1 V. Once this voltage is reached, the current is reversed up to a maximum voltage of 2.7 V in this case. Depending on the sign of the current (negative-cathodic or positive-anodic) charge or discharge of the battery cell takes place. To make it more clear, when applying a negative current, lithium is flowing towards the anode (hydride) and lithiation takes place, meaning the formation of pure Mg and LiH is taking place. (One should keep in mind that this terminology changes when studying cathode materials).
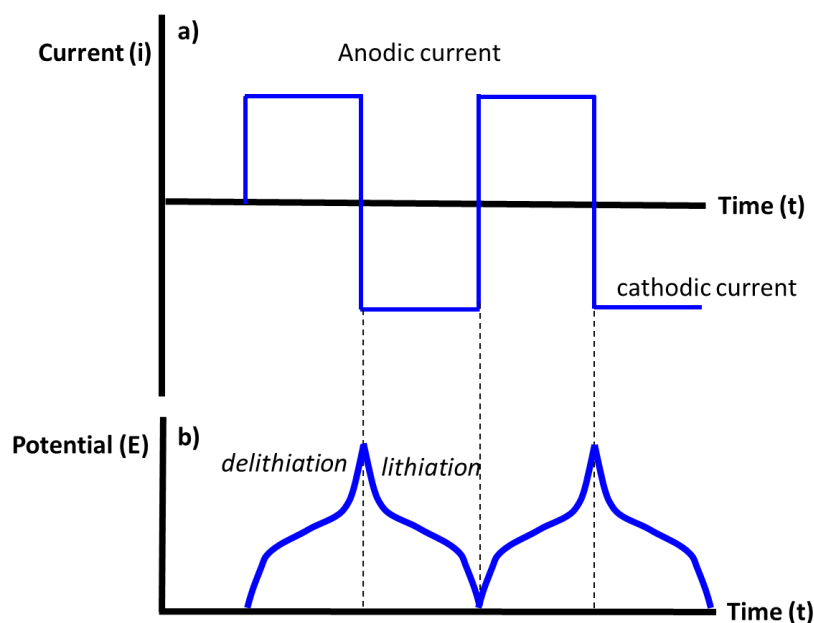
Figure 7-1: a) Current and b) Potential variation during a galvanostatic measurement as a function of time (t)

In cycling, it is important to specify the speed at which lithium flows between the electrodes. The speed depends on the applied current. The higher the current, the faster the cycle will finish. In the case of chrono-potentiometry, it is an established practice to state the speed in a C-rate. This is defined as, 1

divided by the time needed for a complete charge or discharge (not a full cycle). For example, if the sample is charged with 1C, it means that it takes 1 hour to fully charge the sample.

The first galvanostatic cycle was performed at a regimen of $C/50$. Six electrodes were prepared and stopped at different stages of the electrochemical reaction as shown in Figure 7-2.

The electrochemical tests were performed by Dr. Nicola Berti in CNRS Paris in a Swagelok cell, in which a 9 mm square was cut and placed as a working electrode. Pure Li was used as counter and reference electrodes. The electrodes were separated by two Whatman fiber glass filters wetted with liquid electrolyte 1.0 M $LiPF_6$ (in 1:1wt.% DMC:EC). All thin film electrodes were washed in dimethyl carbonate (DMC), which is a component of the liquid electrolyte used and were dried in vacuum. All cells were dismounted in the glovebox and were sent in protective atmosphere to the University of Stuttgart for cross section preparation by FIB and TEM investigations.
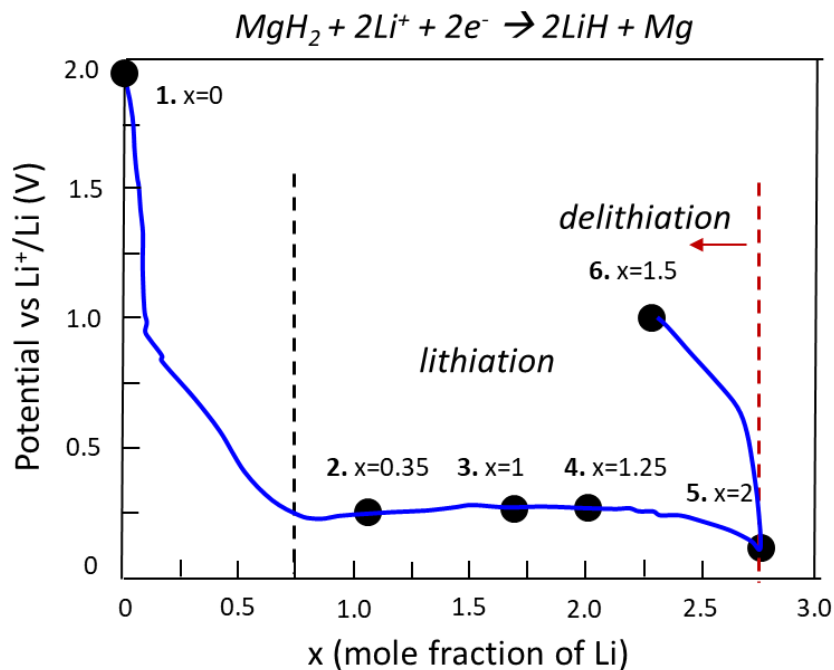
Figure 7-2: Evolution of potential (V) as a function of x (material fraction of Li). The black circles represent the points at which electrochemical charging has been stopped and samples have been recovered for futher investigation. Δx represents the molar fraction of Li stored by the MgH_2 conversion reaction. Dashed lines mark the beginning and the end of the conversion reaction.

Focus during this work was not placed on the capacity of the cell nor its cyclability, but on the microstructure changes that take place during the first cycle. What is important here, is that the capacity fades 50 % after the first cycle. Therefore, investigations on the microstructure changes are essential in understanding and improving the cell. Electron microscopy was done in the frame of this PhD project and the results of this chapter have been submitted for a publication in the Journal of Power Sources (POWER-D-18-02245- [Ni18]).

7.2   Microstructure investigations during first cycle

The six electrodes investigated during this part were prepared by stopping the electrochemical reaction at different stages of charge/discharge. The quantity of stored Li (value of x) has been evaluated by subtracting the contribution of the initial slope illustrated in Figure 7-2, assigned to the solid-electrolyte interface (SEI) formation. Obtaining x = 0 for the as-deposited electrode, x = 0.35 marking the beginning of the conversion, x = 1 for observing the half reaction, x = 2 the full conversion and x = 1.5 showing the partial delithiation after the first charge. Samples 2 to 5 concern the charge state of the reaction and sample 6 the discharge.

Subsequently, each electrode has been investigated by XRD in the department in Paris and the obtained diffractograms are displayed in Figure 7-3. From the XRD diffractograms, a complete conversion of MgH_2 to Mg is observed. After delithiation, the partial reformation of the hydride is also seen at the sample 6. The active phase in the as-deposited thin film (sample 1) is β-MgH_2. On discharge (samples 2, 3 and 4), the intensity of the diffraction peaks of MgH_2 decreases, while those of Mg grow with lithium loading. When the thin film is fully lithiated (sample 5), only the peaks of hexagonal Mg are visible, confirming the complete conversion of the hydride. Afterwards, electrode is partially delithiated during the charge, thus both MgH_2 and Mg diffraction peaks are detected again in the last pattern (sample 6). LiH formed during the conversion reaction could not be detected by XRD, likely because of its low scattering factor. Furthermore, from the XRD characterization of the samples it is clear that the conversion reaction does not make the material amorphous, but it stays crystalline over cycling.
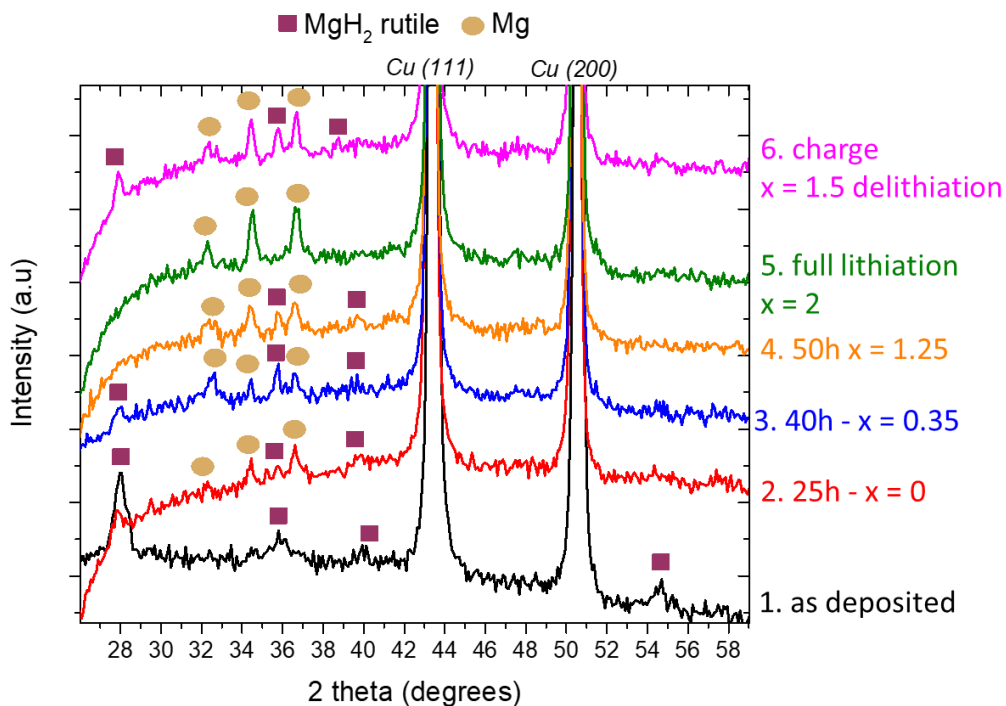
Figure 7-3: XRD patterns obtained at different steps of discharge/charge: a (x=0).

XRD provides information about the formation and crystal structure of crystalline phases into the thin film electrode. However, in order to study their spatial distribution and therefore better understand irreversibility phenomena, other characterization techniques are necessary. For this reason, the same six thin film electrodes were also investigated by TEM. Lamellas were cut from the thin films by FIB and the cross sections were observed by transmission electron microscopy.

The evolution of the thin film microstructure at different steps of the lithiation sweep is displayed in Figure 7-4, which presents the bright field images of each electrode. At the beginning of the lithiation (x = 0.35), white low-diffracting areas appear at specific locations on the surface of the MgH_2 layer. These areas are attributed to LiH formation, further explained in more detail in Figure 7-5. The reaction between MgH_2 and Li has been noticed to start from the surface of the film at selected nucleation sites as shown in sample 2 and then proceeding to the bottom of the layer. While increasing the Li content (x = 1 and 1.25), the conversion reaction progresses as an irregular front from the top to the bottom of the thin film until the electrode is fully lithiated (x = 2).
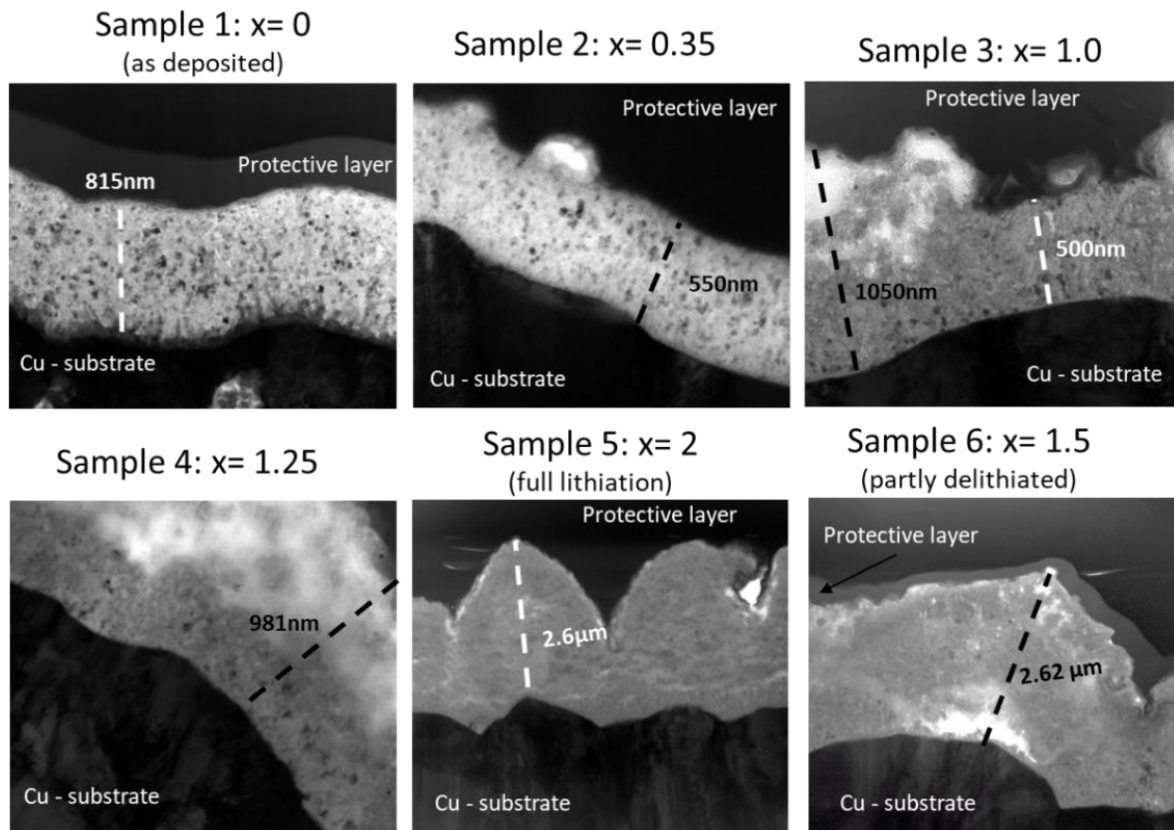
Figure 7-4: Cross section of the six electrodes stopped at different lithiation stage. 1) as-deposited with no lithium present (x=0) 2) beginning of lithiation with x=0.35 lithium 3) further lithiation to x=1 4) further lithiation of x=1.25 with a higher expansion of the layer 5) full lithiation 6) delithiation with x=1.5 lithium left present in the cell.

It is worth noticing that the thin film morphology significantly differs between the as-deposited and the fully lithiated film. The thickness of the lithiated film is much more irregular and its average thickness is much larger compared to the as-deposited film. Film expansion can be related to volume excess

that appears with the conversion reaction. The molar volume of Mg and its hydride given in Table 10, is 13.96 m^3/mol and 18.15 m^3/mol respectively. The film expansion estimated from the micrographs in Figure 7-4 shows to be 130 %, since the initial thickness of 1 µm becomes 2.6 µm at the end of charge. This significant expansion can also be attributed to the fact that the film is fixed on the substrate and can only expand in c direction perpendicular to the substrate. An important observation from these micrographs is also, that no cracks between the film and the substrate are observed during the first cycle.

The presence of LiH in the lithiated parts has been confirmed by selective area electron diffraction patterns (SAED) and EDX. Figure 7-5 shows as an example the analysis performed on the 4th sample with x = 1.25. From indexing the SAED diffraction patterns of the brighter areas closer to the surface of the film, the presence of MgO and LiOH phases is confirmed instead of Mg and LiH respectively. Both materials (LiH and Mg) are sensitive to oxidation and this is unavoidable, due to transfer of the sample, from the FIB to the microscope in air. The continuous rings of the pattern indicate the nano-crystallinity of the LiH, since the beam was focused on a small area. In contrast, at the bottom of the thin film, closer to the substrate, only Mg and MgO are detected everywhere. EDX of both areas (bright and dark) shown in Figure 7-5 a) and d) confirm that Mg is found primarily in dark areas closer to the substrate. Lithium is one of the elements that EDX cannot detect, however lack of Mg may indicate the presence of Li.
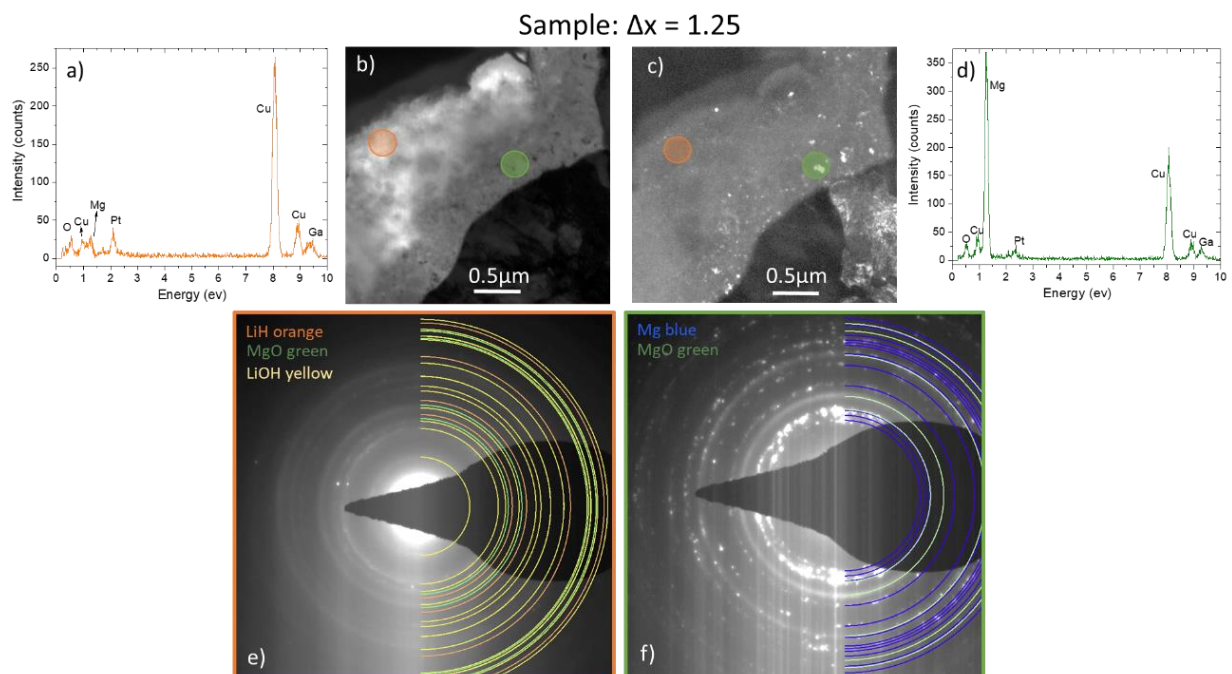
Figure 7-5: EDX analysis of a) the bright white areas (LiH part) and d) of the dark areas (MgH$_2$) part. TEM micro-graphs b) bright field and c) dark field of electrode x = 1.25 (sample 4) with SAED performed on the e) lithiated part (orange) and f) MgH$_2$ (green) part [Ni18].

For further confirmation, Figure 7-6 shows a similar analysis that was done on the fully lithiated sample (x=2), showing the coexistence of LiOH and MgO, which is again evidence of presence of LiH and Mg.

This confirms the full lithiation of the cell, meaning that the conversion reaction of MgH_2 to Mg and LiH over the first cycle is complete as is also shown by the XRD in Figure 7-3.
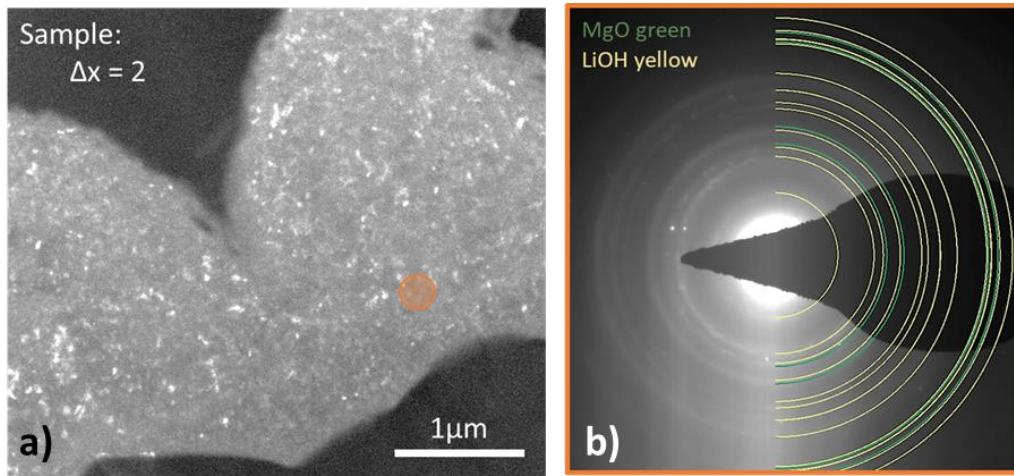
Figure 7-6: a) TEM Dark field image of the fully lithiated sample 5 b) SAED analysis performed in the selected region. The presence of LiOH is visible in the SADP representing the oxidation of LiH [Ni18].

A comparison between partially lithiated (sample 4) and partially delithiated (sample 6) states is shown in Figure 7-7, where different morphologies are observed. The white LiH phase appears only close to the surface of the thin film after discharge (lithiation) (Figure a)), whereas on re-charging (delithiation), it appears at several locations along the cross section (Figure b)). After the charging process (delithiation), the film is only partially recovered back to MgH_2, since the electrochemical measurement was interrupted when the quantity of recovered Li amounted to only 0.5 (i.e., x = 1.5). It is worth noticing, that the electrode in the delithiated state has shrunk with the extraction of lithium in comparison with the fully lithiated sample, due to the partial reformation of MgH_2. However, it is more remarkable that no voids or detachment from the Cu current collector are observed.
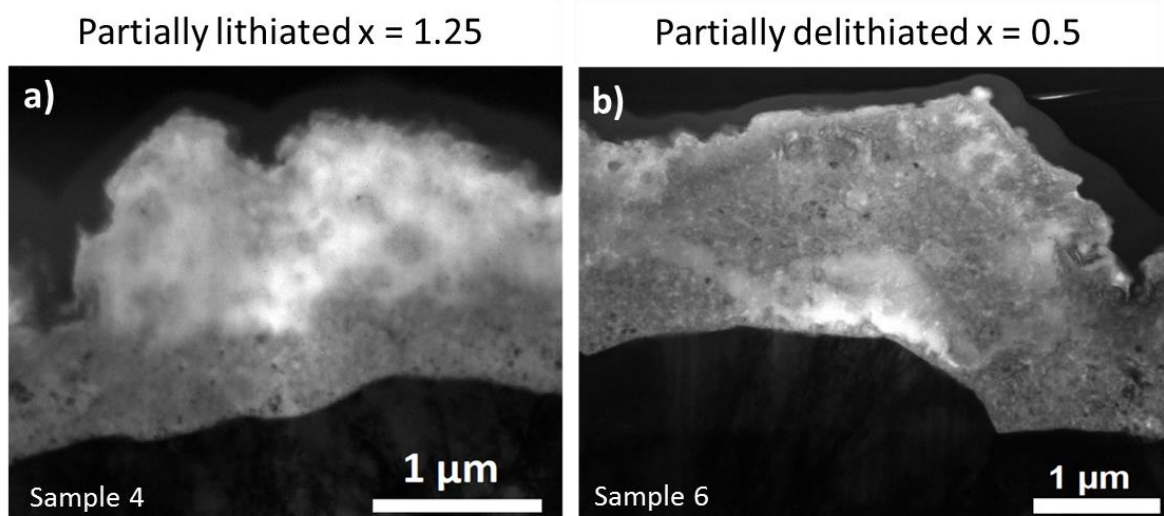
Figure 7-7: Comparison between TEM bright field images of the cross section of a) the partially lithiated and b) partially delithiated samples showing the shrinkage over extraction of lithium [Ni18].

Surprised from the latter observation, a sample cycled for 30 cycles was also investigated at the fully delithiated state. Now, the volume expansion of the film is enormous in comparison to the first cycle expansions. Even, SEM images were enough to show the change in the cell, demonstrated in Figure 7-8. Obviously, there is indeed the tendency to form voids. However, they are not relevant over the first cycles.
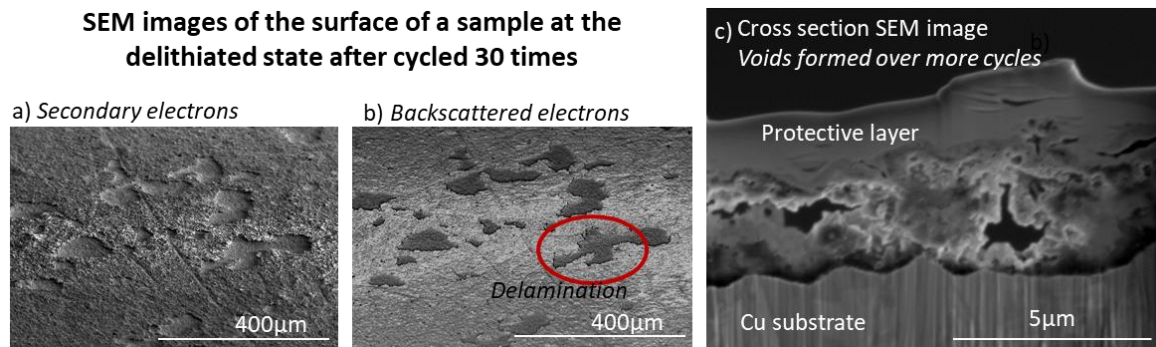
Figure 7-8: Sample cycled for 30 cycles at the same scan rate, showing the voids formed during the later cycles. a) Secondary electron image b) backscattered electron image c) cross section image using secondary electrons showing the voids formed in the sample during cycling.

7.3   Conclusion on MgH$_2$ as battery electrode

MgH$_2$ thin films have been investigated as electrode material for Li-ion battery applications. As-deposited pure hydride electrodes cannot be lithiated in a reproducible way due to the formation of passivating oxides. To prevent this issue, thin films were protected with an Al layer on the surface. Likely, Al is not electrochemically reactive with Li and it avoids formation of MgO, allowing the full conversion of MgH$_2$ to Mg and LiH. The conversion reaction has reported to exhibit a poor reversibility even in the first cycle [Ni18], [Ou08]. Further investigation has been carried out with the purpose of understanding the capacity fading.

The main issues that could cause irreversibility are: side reactions, such as Mg-Li alloying interfering with the conversion reaction, cracks and voids due to the volume changes during lithiation/delithiation, poor electric conductivity because of the formation of insulating LiH at the end of the discharge and/or poor mass transport during cycling.

Here, it could be shown that the conversion reaction reveals no cracks, voids or detachment of the thin film from the current collector during the first charge. XRD and TEM migrographs allow the observation of full lithiation of the cells and identify the regions where LiH is first formed. As expected, the lithiation starts from the surface and continues towards the substrate. An expansion of the film is observed, which at first is not dominant, since it also appears to shrink back over the first delithiation. Showing this way, that the volume changes are not the main issues related to the poor reversibility of the first cycle of this conversion reaction of MgH$_2$. After cycling over 30 cycles, voids are formed. However,

these are most probably caused by other factors than volume expansion, most likely related to mass transport. In order to overcome this issue, future studies should focus on understanding the solid state mass transport of hydrogen microstructures upon electrochemical cycling for improving the reversibility of metal hydrides as conversion electrodes in Li ion batteries.

8 CONCLUSIONS

It would be hard to imagine a world without cell phones, cars, planes, with no fridges, lights even without smaller things like clocks, remote controllers, cameras, flashlights, hair dryers. All technologies have been born out of a need or a purpose for something better. The desire of development is part of our humanity and this continuous technological evolution of our society increased the demand of energy supply. Nature offers considerable resources such as water, trees, rare earth minerals, fossil fuels etc., that seem to be abundant. However, exploiting these resources can bring many dangers upon humanity. As the stone age did not end because the earth had run out of stones, but new technologies were discovered, so should our modern society not wait until the last resources vanished, before turning to something more sustainable.

Moving into a sustainable and clean energy economy is a necessity for our future. Significant effort has been focused on using hydrogen as a fuel. Finding the best possible safe conditions for large volumes of hydrogen has been however, a challenge. Instead of using gas tanks, storage in form of hydrides is a promising concept to bond hydrogen with other elements in a solid state, either in ionic (negative H^- or positive H^+ ions), covalent or metallic form. The reversibility of these compounds by simply tuning the pressure and temperature makes them attractive for future applications.

One of the most considerable elemental materials is magnesium (Mg) and its hydride (MgH_2). Due to several attractive properties of this metal, noteworthy studies have been motivated on improving this material. Despite many advantages, formation of this hydride creates an exothermic reaction with an enthalpy of $\Delta H_0 =$ -75 kJ/mol of H_2 and an entropy of $\Delta S_0 = -$ 133 J/mol of H_2. The high stability of this hydride raises consequently problems in reversibility. The decomposition temperature is at ≈ 300 °C, which is a too high temperature for desired function.

Alloying with transition metals (changing the composition) and nanostructuring are few of the methods reported to improve significantly the properties of hydrides, including MgH_2. So far however, the decomposition temperature has not yet been decreased considerably. The use of palladium (Pd) as a catalyst in the MgH_2 formation has been shown during this work to be necessary. Due to its high cost however, alternative transition metals could be used and titanium is one of the good candidates since it is not miscible with Mg.

This work has been focused on investigating hydrogen transport in thin films of magnesium (Mg) and titanium (Ti), separately. Thin films of a defined micro-structure and geometry allow a precise investigation of the changes. Furthermore, MgH_2 is a semi-conductor with a band gap of about 4 eV and consequently low electrical conductivity, which is a property used for studying the material in thin films and nanostructures.

A comprehensive way to quantitatively characterize the kinetics of hydride formation in metallic thin films has been shown in this work. A methodology allowing the control of a wide range of pressures and temperatures has been developed successfully. X-day diffraction (XRD), electron microscopy (SEM/FIB/TEM) and resistance measurements are used to obtain a precise evaluation of the diffusion coefficients and give further information on the mechanism of hydrogenation inside the metals (Mg and Ti). The combination of these techniques could be used to investigate other systems as well, since it allows a broad variety of observations at different experimental conditions.

The results of this work, experimentally advocate that the diffusion of hydrogen through the MgH_2 and the TiO_2 are the dominant kinetics barrier of hydrogenation in the respective materials. Modeling of the resistance change upon hydrogenation, the kinetics of the system follows a transition from linear to parabolic. The model fits nicely to small thicknesses. However, the thicker the layer becomes, the more difficult it becomes to fit to the linear part of the model. It is concluded that the mechanism of diffusion is sensitive to the production method of the samples. A central difference between the Mg system and Ti thin films is the fact, that Mg hydride is formed closer to the surface of the thin film and grows towards the substrate creating a blocking barrier. By contrast, in the case of Ti, the hydride is formed from the substrate towards the surface.

The main conclusions for both systems may be summarized in the following way:

Regarding the use of Mg as a hydrogen storage system, investigations on the limitations of the system have been clarified during this work. Mg layers with a thin Pd (5 – 40 nm) coating have been investigated. The main conclusions are:

o   Hydride formation in Mg starts at about 100 °C and is measurable by XRD. A thermal expansion of Mg is first observed, which stops, due to compressive stresses once the hydride starts to form.

o   The ion and electron beam for cross section view preparation damages the hydride phase, but the microstructure transformation between Mg and MgH_2 is nevertheless clearly visible. Even though electron microscopy irreversibly damages the hydride phase, it is still useful to follow the hydrogenation kinetics and the layer growth. The selective area diffraction patterns allow the confirmation of phases. The presence of MgO is dominant since the sample is quickly oxidized in air.

o   Co-existence of MgH_2 and Mg has been observed using SEM and TEM. A visual observation of the different morphologies is obtained. The transition from a columnar grain structure with a fiber texture in the as-deposited Mg thin film to an equi-axed fine grainy structure indicates the hydride formation unambiguously.

o   During hydrogenation, the hydride is immediately formed at the interface between the Pd catalyst coating and the Mg thin film and grows in a layer-like reaction towards the substrate creating a

blocking layer for further hydrogen loading.

o   Change in resistance during hydrogen loading of Mg allows for a more precise observation of the time lag of the hydrogenation. Modelling the resistance shows, that the system initially follows a linear kinetics. A transition into a parabolic regimen is observed once the thickness of the hydride becomes dominant.

o   Modelling of the resistance behavior allows evaluation of the thickness growth over time. The thickness of the hydride at the inflection point of the resistance change amounts to 85 % of the initial metal thickness.

o   A quantitative evaluation of the diffusion coefficient of hydrogen in the Mg system, in a broad range of temperature (room temperature to 300 °C), has been successful. So, an experimental Arrhenius plot was obtained from room temperature to 300 °C for the first time. The activation energy and the pre-factor are determined to E_a = 22.6 ± 2 kJ/mol and D_0 = 3904 cm^2/s, respectively.

o   The diffusion coefficient, calculated using a model describing a combination from linear to para-bolic transition (in the resistance measurements), is in good agreement to the diffusion coefficient measured at 300 °C using the ex-situ XRD measurements.

o   The Mg/Pd interface appears to be unstable during even the first hydrogenation, when hydro-genation takes place at temperatures higher than 50 °C. The miscibility of the two elements rep-resents a drawback to good cyclability. The new phases formed have been identified as Mg_5Pd and Mg_6Pd. The thickness of the Mg-Pd layer is shown to expand over the cycle life of the layer, since the molar volume of the intermetallic phases is significantly larger than that of the initial Pd coating. The stability of the new Mg-Pd phases has no negative effect on the first re-hydrogena-tion of the samples, however it consumes Mg, which cannot be hydrogenated furthermore.

o   Dehydrogenation of the samples is possible only at a temperature of 300 °C and above, at which the formation of Mg-Pd alloys and the development of voids inside the material is unavoidable.

While magnesium hydride has been shown to play an attractive role in hydrogen storage applications and its detailed investigation was the scope of this work, additional tests of MgH$_2$ as an electrode ma-terial in Li-ion batteries have revealed promising results. Batteries play a dominant role in the evolution of energy storage. Their improvement for more energy, safer and better cyclability gives a great moti-vation to scientific studies.

This part of the work was part of a collaboration with the ICMPE, CNRS in Paris. Focus was placed on the changes in the microstructure of MgH$_2$ thin film electrodes in half cells with liquid electrolyte.

•   MgH$_2$ has been shown to effectively lithiate when no MgO is formed on the surface of the elec-trode. A thin layer of Al deposition before exposure in air allows a better stability of the hydride and does not block the lithiation of the hydride.

- The conversion reaction exhibits no cracks, voids or detachment of the thin film from the current collector in the first cycle, but pores are formed in later cycles, presumably by unbalanced atomic material.

- TEM micrographs demonstrate that the lithiation starts from the surface and continues towards the substrate. An expansion of the film is observed, that does not degrade the electrodes, since it shrank over the first delithiation, showing that the volume changes are not the main issues related to the poor reversibility of the first cycle of this conversion reaction of MgH_2.

Regarding the use of the Ti system in hydrogen storage applications, the main conclusions this work are:

- Sputter-deposited Ti thin films in ambient atmosphere and at room temperature naturally oxidize to rutile TiO_2 at the surface to an average thickness of 9.8 nm.

- Thin films of Ti covered with the natural oxide show at 300 °C a reasonable hydrogenation rate for pressures ranging from 0.05 to 100 bar. The hydrogenation kinetics at 20 bar is linear in time, indicating a barrier controlled reaction. The hydride grows in a layer-like geometry being nucleated remote from the surface. The linear growth coefficient amounts to $\kappa = 2.57 \cdot 10^{-10}$ cm/s. The permeation coefficient ($c_H D_H$) of hydrogen through TiO_2 amounts to $p_H^{TiO_2} = 2.85 \cdot 10^7$ cm^{-1}·s^{-1}.

- Pd/Ti bilayers preventing oxide formation and Pd/TiO_2/Ti triple layers were compared in terms of their hydrogenation reaction. While the non-oxidized system hydrogenates immediately, even at room temperature, the triple layer again needs a temperature of 300 °C to present reasonable hydrogenation rates. This direct comparison demonstrates the high impact of the kinetics barrier that is introduced by the oxide on the one hand. On the other hand, it also shows that it is not the splitting of the H_2 molecules at the oxide surface, but the transport of hydrogen atoms through the oxide that provides the decisive rate-controlling factor.

- The minimum diffusion coefficient of hydrogen into titanium at room temperature amounts to: $D_H^{Ti} \geq 1.6 \cdot 10^{-10}$ cm^2/s.

- The hydrogenation rate first increases with the pressure, but reaches a saturation level at about 1 bar from which no further acceleration is obtained, even with increasing the pressure. This behavior is quantitatively understood by the full occupation of available surface sites. At 300 °C the critical pressure at which half of the surface sites become occupied by hydrogen amounts to $p^* = 0.21$ bar.

Before considering a potential use of these systems for hydrogen storage, major improvement must be achieved. Simply replacing Pd with Ti will not improve the system if it is exposed to air, since TiO_2 is a stable compound that slows down the diffusion of hydrogen in the system. Having a tri-layer of

Mg/Ti/Pd could eventually be a solution, since Mg and Ti are not miscible and the Pd will prevent the oxidation of Ti. However, Ti-Pd compounds can also be formed depending on the temperatures used. Literature is available on this sandwiched tri-layer, however, investigations have only been done in smaller layer thicknesses of 10 - 20 nm.

The tri-layer system could also improve the dehydrogenation for both systems. Dehydrogenation of Ti was not investigated during this work, due to the fact that temperatures higher than 500 °C are required for decomposition of TiH_2. At these temperatures, the formation of Ti-Silicates with the substrate is unavoidable. Finding a suitable substrate is not as easy as one may think, since MgO and AlO_2 have also shown to be unstable in contact to Ti at these temperatures. In a case of a tri-layer system, silicates will not be formed and the dehydrogenation of TiH_2 could also be investigated.

Knowing the mechanism of diffusion as well as the diffusion coefficients can help improve the materials for future use. Knowing the activation energy of diffusion, the permeation coefficients and the role of experimental conditions, such as pressure and temperature, is important for evaluating whether a material is suitable for application. This thesis shows a reliable way for studying hydrides. Similar investigations may be applied on other hydrides to obtain more accurate knowledge of the mechanism of hydrogen transport.

One should use all the tools available for advancing the future into a more sustainable economy. Fossil fuels as part of our energy consumption are the biggest source of the atmospheric CO_2 damaging our planet. Moving into something more green, sustainable and clean is a necessity for our future and hopefully the nature of discovery is, that it is not possible to anticipate what will be found. Imagining a future where new developments and dreamlike innovations come true is just at the horizon.

9 REFERENCES

[ALJ99]   A. Zaluska; L. Zaluski; J.O. Strom–Olsen: Nanocrystalline magnesium for hydrogen storage. In Journal of Alloys and Compounds, 1999, 288; pp. 217–225.

[AMM14]   Abdessameud, S.; Mezbahul-Islam, M.; Medraj, M.: Thermodynamic modeling of hydrogen storage capacity in Mg-Na alloys. In TheScientificWorldJournal, 2014, 2014; p. 190320.

[AOB15]   Aymard, L.; Oumellal, Y.; Bonnet, J.-P.: Metal hydrides. An innovative and challenging conversion reaction anode for lithium-ion batteries. In Beilstein journal of nanotechnology, 2015, 6; pp. 1821–1839.

[ASI82]   Arita, M.; Shimizu, K.; Ichinose, Y.: Thermodynamics of the Ti-H system. In Metallurgical Transactions A, 1982, 13; pp. 1329–1336.

[Ba16]   Bakulin, A. V. et al.: Hydrogen diffusion in doped and undoped α-Ti. An ab-initio investigation. In International Journal of Hydrogen Energy, 2016, 41; pp. 9108–9116.

[Be17]   Berti, N. et al.: Enhanced reversibility of the electrochemical Li conversion reaction with MgH 2 –TiH 2 nanocomposites. In International Journal of Hydrogen Energy, 2017, 42; pp. 22615–22621.

[Br12]   Brutti, S. et al.: Magnesium hydride as a high capacity negative electrode for lithium ion batteries. In Journal of Materials Chemistry, 2012, 22; p. 14531.

[Ca16]   Calizzi, M. et al.: Gas-phase synthesis of Mg-Ti nanoparticles for solid-state hydrogen storage. In Phys Chem Chem Phys, 2016, 18; pp. 141–148.

[CGW10]   Croston, D. L.; Grant, D. M.; Walker, G. S.: The catalytic effect of titanium oxide based additives on the dehydrogenation and hydrogenation of milled MgH2. In Journal of Alloys and Compounds, 2010, 492; pp. 251–258.

[Ch97]   Chen, C. et al.: Measurement of oxide film growth on Mg and Al surfaces over extended periods using XPS. In Surface Science, 1997, 382; L652-L657.

[Cr16a]   Crivello, J.-C. et al.: Review of magnesium hydride-based materials. Development and optimisation. In Applied Physics A, 2016, 122; p. 5077.

[Cr16b]   Crivello, J.-C. et al.: Mg-based compounds for hydrogen and energy storage. In Applied Physics A, 2016, 122; p. 122.

[Da09]   David Moser et al.: Structure and stability of high pressure synthesized Mg-TM hydrides (TM= Ti, Zr, Hf, V, Nb and Ta) as possible new hydrogen rich hydrides for hydrogen storage. In Journal of Materials Chemistry, 2009, 19; pp. 8150–8161.

[Da83]   Dantzer, P.: High temperature thermodynamics of H2 and D2 in titanium, and in dilute titanium oxygen solid solutions. In Journal of Physics and Chemistry of Solids, 1983, 44; pp. 913–923.

[Do06]   Dornheim, M. et al.: Tailoring Hydrogen Storage Materials Towards Application. In Advanced Engineering Materials, 2006, 8; pp. 377–385.

[Do07]   Dornheim, M. et al.: Hydrogen storage in magnesium-based hydrides and hydride composites. In Scripta Materialia, 2007, 56; pp. 841–846.

[Do17]   Dominik, M. et al.: Titanium oxide thin films obtained with physical and chemical vapour deposition methods for optical biosensing purposes. In Biosensors & bioelectronics, 2017, 93; pp. 102–109.

[Du11]   Dura, J. A. et al.: Porous Mg formation upon dehydrogenation of MgH 2 thin films. In Journal of Applied Physics, 2011, 109; p. 93501.

[Du12]   Du Y, P. N. G. et al.: Hydrogen reactivity on highly-hydroxylated TiO2(110) surfaces prepared via carboxylic acid adsorption and photolysis. In Phys Chem Chem Phys, 2012.

[Ei09]   Eisler, M. N.: "A Modern 'Philosopher's Stone'". Techno-Analogy and the Bacon Cell. In Technology and Culture, 2009, 50; pp. 345–365.

[Ei11]   Eijt, S.W.H. et al.: Layer-resolved study of the Mg to MgH2 transformation in Mg–Ti films with short-range chemical order. In Journal of Alloys and Compounds, 2011, 509; S567-S571.

[Fa62]   Farber, E.: The Development of Metal Hydride Chemistry. In Chymia, 1962, 8; pp. 165–180.

[Fl13]   Floriano, R. et al.: Nanostructured MgH2 obtained by cold rolling combined with short-time high-energy ball milling. In Materials Research, 2013, 16; pp. 158–163.

[FMO02]   Fournier, V.; Marcus, P.; Olefjord, I.: Oxidation of magnesium. In Surface and Interface Analysis, 2002, 34; pp. 494–497.

[fu]   fuel-cell portal: Hydrogen refuelling stations worldwide. www.h2stations.org.

[Fu05]   Fukai, Y.: The metal-hydrogen system. Basic bulk properties. Springer, Berlin, New York, 2005.

[Ga11a]   Gao, W. et al.: Thermodynamics approach to the hydrogen diffusion and phase transformation in titanium particles. In Journal of Alloys and Compounds, 2011, 509; pp. 2523–2529.

[Ga11b]   Gautam, Y. K. et al.: Hydrogenation of Pd-capped Mg thin films prepared by DC magnetron sputtering. In Applied Surface Science, 2011, 257; pp. 6291–6295.

[GAÖ13]   Gharavi, A. G.; Akyıldız, H.; Öztürk, T.: Thickness effects in hydrogen sorption of Mg/Pd thin films. In Journal of Alloys and Compounds, 2013, 580; S175-S178.

[GKC13]   Gautam, Y. K.; Kumar, M.; Chandra, R.: Hydrogen absorption and desorption properties of Pd/Mg/Pd tri-layers prepared by magnetron sputtering. In Surface and Coatings Technology, 2013, 237; pp. 450–455.

[Ha17]   Hadjixenophontos, E. et al.: Imaging the hydrogenation of Mg thin films. In International Journal of Hydrogen Energy, 2017, 42; pp. 22411–22416.

[Ha18]   Hadjixenophontos, E. et al.: The role of surface oxides on hydrogen sorption kinetics in titanium thin films. In Applied Surface Science, 2018.

[Ho70]   Holleck; Gerhard L.: Diffusion and solubility of hydrogen in palladium and palladium--silver alloys. In Diffusion and solubility of H in Pd and Pd-Ag alloys, 1970, 74; pp. 503–511.

[HP17]   Hamm M; Pundt A: FEM simulation supported evaluation of a hydrogen grain boundary diffusion coefficient in MgH2. In International Journal of Hydrogen Energy, 2017, 42; pp. 22530–22537.

[Hu13]   Huot, J. et al.: Mechanochemical synthesis of hydrogen storage materials. In Progress in Materials Science, 2013, 58; pp. 30–75.

[Hy]   Hydrogen mobility Europe: http://h2me.eu/about/hydrogen-refuelling-infrastructure/s.

[ICP11]   Islam, M. M.; Calatayud, M.; Pacchioni, G.: Hydrogen Adsorption and Diffusion on the Anatase TiO 2 (101) Surface. A First-Principles Investigation. In The Journal of Physical Chemistry C, 2011, 115; pp. 6809–6814.

[Ik13]   Ikeda, S. et al.: Anode properties of magnesium hydride catalyzed with niobium oxide for an all solid-state lithium-ion battery. In Chemical communications (Cambridge, England), 2013, 49; pp. 7174–7176.

[IO05]   Ingason, A. S.; Olafsson, S.: Thermodynamics of hydrogen uptake in Mg films studied by resistance measurements. In Journal of Alloys and Compounds, 2005, 404-406; pp. 469–472.

[J.78]   J.I Langford and A.J.C Wilson: Seherrer after Sixty Years: A Survey and Some New Results in the Determination of Crystallite Size. In Journal of Applied crystallography, 1978, 11; pp. 102–113.

[Je03]   Jeremy Rifkin: The Hydrogen Economy. After Oil, Clean Energy From a Fuel-Cell-Driven Global Hydrogen Web.

[Jo10]   Johansson, M. et al.: Hydrogen adsorption on palladium and palladium hydride at 1bar. In Surface Science, 2010, 604; pp. 718–729.

[Ju14]   Jung, H. et al.: Effects of Ti interlayers on microstructures and hydrogen storage capacity in Mg/Pd multilayer thin films. In Journal of Alloys and Compounds, 2014, 601; pp. 63–66.

[KBW04]   Kunat, M.; Burghaus, U.; Wöll, C.: The adsorption of hydrogen on the rutile TiO 2 (110) surface. In Phys. Chem. Chem. Phys., 2004, 6; pp. 4203–4207.

[KC10]   Kelly, S. T.; Clemens, B. M.: Moving interface hydride formation in multilayered metal thin films. In Journal of Applied Physics, 2010, 108; p. 13521.

[KZ70]   Korn, C.; Zamir, D.: NMR study of hydrogen diffusion in the three different phases of the titanium-hydrogen system. In Journal of Physics and Chemistry of Solids, 1970, 31; pp. 489–502.

[L.09]   L.B. Freund and S. Suresh: Thin film Materials. Stress, Defect Fromation and Surface evo-
           lusion, 2009.

[Le53]   Levinger, B. W.: Lattice Parameter of Beta Titanium at Room Temperature. In JOM,
           1953, 5; p. 195.

[Li08]   Li, S.-C. et al.: Intrinsic diffusion of hydrogen on rutile TiO2(110). In Journal of the Ameri-
           can Chemical Society, 2008, 130; pp. 9080–9088.

[LIJ]   Louis Schlapbach; Ian Anderson; Jean Paul Burger: Hydrogen in Metlas. In Materials Sci-
           ence and technology; pp. 272–326.

[LR04]   Lehmhus, D.; Rausch, G.: Tailoring Titanium Hydride Decomposition Kinetics by Anneal-
           ing in Various Atmospheres. In Advanced Engineering Materials, 2004, 6; pp. 313–330.

[Ma05]   Makongo, J. et al.: A case study of complex metallic alloy phases. Structure and disorder
           phenomena of Mg-Pd compounds. In Philosophical Magazine, 2005, 86; pp. 427–433.

[Ma06]   Makongo, J. P. A. et al.: A case study of complex metallic alloy phases. Structure and dis-
           order phenomena of Mg–Pd compounds. In Philosophical Magazine, 2006, 86; pp. 427–
           433.

[Ma09a]   Matsuo, M. et al.: Complex hydrides with (BH(4))(-) and (NH(2))(-) anions as new lithium
           fast-ion conductors. In Journal of the American Chemical Society, 2009, 131; pp. 16389–
           16391.

[Ma09b]   Maekawa, H. et al.: Halide-stabilized LiBH4, a room-temperature lithium fast-ion con-
           ductor. In Journal of the American Chemical Society, 2009, 131; pp. 894–895.

[Ma11]   Martin Dornheim: Thermodynamics of Metal Hydrides: Tailoring Reaction Enthalpies of
           Hydrogen Storage Materials. Thermodynamics - Interaction Studies - Solids, Liquids and
           Gases, Dr. Juan Carlos Moreno. In InTech, 2011, ISBN 978-953-307-563-1; pp. 891–918.

[Ma15]   Ma, M. et al.: Phase transformations of titanium hydride in thermal desorption process
           with different heating rates. In International Journal of Hydrogen Energy, 2015, 40; pp.
           8926–8934.

[MD13]   Mooij, L.; Dam, B.: Nucleation and growth mechanisms of nano magnesium hydride
           from the hydrogen sorption kinetics. In Physical chemistry chemical physics PCCP, 2013,
           15; pp. 11501–11510.

[MO11]   Matsuo, M.; Orimo, S.-i.: Lithium Fast-Ionic Conduction in Complex Hydrides. Review
           and Prospects. In Advanced Energy Materials, 2011, 1; pp. 161–172.

[Mo14]   Mohammad Daryani: Effects of Ti-basded catalysts on hyrogen desoprtion kinetics of
           nanostructured magnesium hydride. In International Journal of Hydrogen Energy, 2014.

[Ni18]   Nicola Berti et al.: Thin films as model system for understanding the electrochemical re-
           action mechanisms in conversion reaction of MgH2 with lithium. submission number:
           POWER-S-18-02987. In Journal of Power Sources, 2018.

[NV15]   Nayak, V.; Verma, U. P.: Phase transition and optoelectronic properties of MgH 2. In
           Phase Transitions, 2015, 89; pp. 437–447.

[Og10]   Oguchi, H. et al.: Lithium-ion conduction in complex hydrides LiAlH4 and Li3AlH6. In Journal of Applied Physics, 2010, 107; p. 96104.

[Ok07]   Okamoto, H.: Mg-Si (Magnesium-Silicon). In Journal of Phase Equilibria and Diffusion, 2007, 28; pp. 229–230.

[Ok10]   Okamoto, H.: Mg-Pd (Magnesium-Palladium). In Journal of Phase Equilibria and Diffusion, 2010, 31; pp. 407–408.

[Ou08]   Oumellal, Y. et al.: Metal hydrides for lithium-ion batteries. In Nature materials, 2008, 7; pp. 916–921.

[Ou09]   Oumellal, Y. et al.: 2LiH+M (M=Mg, Ti). New concept of negative electrode for rechargeable lithium-ion batteries. In Journal of Power Sources, 2009, 192; pp. 698–702.

[Ou14]   Oumellal, Y. et al.: Bottom-up preparation of MgH$_2$ nanoparticles with enhanced cycle life stability during electrochemical conversion in Li-ion batteries. In Nanoscale, 2014, 6; pp. 14459–14466.

[P.93]   P. Spatz et al.: Diffusion of H in Mg and the nucleation and Growth of MgH2 in thin films. In Zeitschrfift fur Physikalische Chemie, 1993; pp. 393–397.

[Ph91]   Philibert, J.: Atom movements - diffusion and mass transport in solids. In les editions de physique, 1991.

[PM82]   P.Millenbach; M.Givon: The electrochemical formation of TiH2. In Journal of the less common metals, 1982, 87; pp. 179–184.

[Po16a]   Poletaev, D. O. et al.: Hydrogen solubility in hcp titanium with the account of vacancy complexes and hydrides. A DFT study. In Computational Materials Science, 2016, 114; pp. 199–208.

[Po16b]   Poletaev, D. O. et al.: Hydrogen solubility in hcp titanium with the account of vacancy complexes and hydrides. A DFT study. In Computational Materials Science, 2016, 114; pp. 199–208.

[Po91]   Pound, B. G.: Hydrogen Ingress in Titanium. In CORROSION, 1991, 47; pp. 99–104.

[PPY95]   Pyun, S.-I.; Park, J.-W.; Yoon, Y.-G.: Hydrogen permeation through PECVD (plasma-enhanced chemical vapor deposition) TiO2 film on Pd by the time lag method. In Journal of Alloys and Compounds, 1995, 231; pp. 315–320.

[QZS13]   Qin, Z.; Zeng, Y.; Shoesmith, D. W.: Modeling hydrogen permeation through a thin titanium oxide film and palladium. In Thin Solid Films, 2013, 534; pp. 673–679.

[R.62]   R.WOOD: The Lattice Constants of High Purity Alpha Titanium. In Proceedings of the Physical Society, 1962, 80.

[R.95]   R. Jeffrey Swope, Joseph R. Smyth: H in rutile-type compounds: I. Single-crystal neutron and X-ray diffraction study of H in rutile. In American mineralogisi, 1995, 80; pp. 448–453.

[Sa07]   Saita, I. et al.: Hydrogen storage property of MgH2 synthesized by hydriding chemical vapor deposition. In Journal of Alloys and Compounds, 2007, 446-447; pp. 80–83.

[Sa72]   Sampson, S.: Complex cubic A6B compounds. II. The crystal structure of Mg6Pd. In Acta Crystallographica Section B Structural Crystallography and Crystal Chemistry, 1972, 28; pp. 936–945.

[Sc98]   Schmitz, G. et al.: Diffusion of hydrogen through metallic multilayers. In Physical Review B, 1998, 58; pp. 7333–7339.

[SCL16]   Sartori, S.; Cuevas, F.; Latroche, M.: Metal hydrides used as negative electrode materials for Li-ion batteries. In Applied Physics A, 2016, 122; p. 916.

[Se04]   Setoyama, D. et al.: Characteristics of titanium–hydrogen solid solution. In Journal of Alloys and Compounds, 2004, 385; pp. 156–159.

[SF65]   Simons, J. W.; Flanagan, T. B.: Diffusion of Hydrogen in the α-Phase of the Palladium-Hydrogen System. In The Journal of Physical Chemistry, 1965, 69; pp. 3581–3587.

[Sh00]   Shushi Suzuki et al.: Hydrogen Adatoms on TiO2110-1 3 1 Characterized by Scanning Tunneling Microscopy. In PHYSICAL REVIEW LETTERS, 2000, 84; p. 2156.

[Sh07]   Shih, Y.-H. et al.: Effect of nano-titanium hydride on formation of multi-nanoporous TiO 2 film on Ti. In Applied Surface Science, 2007, 253; pp. 3678–3682.

[SLH07a]   Sakintuna, B.; Lamari-Darkrim, F.; Hirscher, M.: Metal hydride materials for solid hydrogen storage. A review. In International Journal of Hydrogen Energy, 2007, 32; pp. 1121–1140.

[SLH07b]   Sakintuna, B.; Lamari-Darkrim, F.; Hirscher, M.: Metal hydride materials for solid hydrogen storage. A review☆. In International Journal of Hydrogen Energy, 2007, 32; pp. 1121–1140.

[Sm58]   Smits, F. M.: Measurement of Sheet Resistivities with the Four-Point Probe. In Bell System Technical Journal, 1958, 37; pp. 711–718.

[SM87a]   San-Martin, A.; Manchester, F. D.: The H–Mg (Hydrogen-Magnesium) system. In Journal of Phase Equilibria, 1987, 8; pp. 431–437.

[SM87b]   San-Martin, A.; Manchester, F. D.: The H–Ti (Hydrogen-Titanium) system. In Bulletin of Alloy Phase Diagrams, 1987, 8; pp. 30–42.

[SM87c]   San-Martin, A.; Manchester, F. D.: The H–Ti (Hydrogen-Titanium) system. In Bulletin of Alloy Phase Diagrams, 1987, 8; pp. 30–42.

[SR10]   Sen, I.; Ramamurty, U.: Elastic modulus of Ti–6Al–4V–xB alloys with B up to 0.55wt.%. In Scripta Materialia, 2010, 62; pp. 37–40.

[SSR17]   Surrey, A.; Schultz, L.; Rellinghaus, B.: Electron beam induced dehydrogenation of MgH2 studied by VEELS. In Advanced Structural and Chemical Imaging, 2017, 2; p. 526.

[St10]   Steven Barcelo: Hydrogen storage property of sandwiched magnesium hydride nanoparticle thin film. In Journal of hydrogen energy, 2010, 35; pp. 9232–9235.

[SZ01]   Schlapbach, L.; Züttel, A.: Hydrogen-storage materials for mobile applications. In Nature, 2001, 414; pp. 353–358.

[Ta12]   Tao, J. et al.: Diffusion and Reaction of Hydrogen on Rutile TiO 2 (011)-2×1. The Role of Surface Structure. In The Journal of Physical Chemistry C, 2012, 116; pp. 20438–20446.

[THP17]   Teichmann, N.; Hamm, M.; Pundt, A.: Fast lateral hydrogen diffusion in magnesium-hydride films on sapphire substrates studied by electrochemical hydrogenography. In International Journal of Hydrogen Energy, 2017.

[TSE17]   Tomán, J. J.; Schmitz, G.; Erdélyi, Z.: Linear-parabolic transition in reactive diffusion – A concept of kinetic modelling. In Computational Materials Science, 2017, 138; pp. 183–191.

[Uc15]   Uchida, H. T. et al.: Absorption kinetics and hydride formation in magnesium films. Effect of driving force revisited. In Acta Materialia, 2015, 85; pp. 279–289.

[Ve08]   Vermeulen, P. et al.: In situ electrochemical XRD study of (de)hydrogenation of Mg_yTi_{100-y} thin films. In Journal of Materials Chemistry, 2008, 18; p. 3680.

[Wa10]   Wang, K. et al.: Thermodynamic description of the Ti–H system. In Calphad, 2010, 34; pp. 317–323.

[Wa96]   Wang, W.-E.: Thermodynamic evaluation of the titanium-hydrogen system. In Journal of Alloys and Compounds, 1996, 238; pp. 6–12.

[WP11]   Wagner, S.; Pundt, A.: Combined impact of microstructure and mechanical stress on the electrical resistivity of PdH_c thin films. In Acta Materialia, 2011, 59; pp. 1862–1870.

[Y.07]   Y. Bouhadda, A. Rabehi and S. Bezzari-Tahar-Chaouche: First-principle calculation of $MgH2$ and LiH for hydrogen storage. In Revue des Energies Renouvelables, 2007, 10; pp. 545–550.

[Ya08]   Yao, X. et al.: Hydrogen diffusion and effect of grain size on hydrogenation kinetics in magnesium hydrides. In Journal of Materials Research, 2008, 23; pp. 336–340.

[Yi08]   Yin, X.-L. et al.: Diffusion versus desorption. Complex behavior of H atoms on an oxide surface. In Chemphyschem a European journal of chemical physics and physical chemistry, 2008, 9; pp. 253–256.

[Yu03]   Yu, G. C.: A comparison between proton and hydrogen chemical diffusion coefficients of titanium oxide films. In physica status solidi (a), 2003, 198; pp. 302–311.

[Za11]   Zaïdi, W. et al.: Carboxymethylcellulose and carboxymethylcellulose-formate as binders in $MgH2$–carbon composites negative electrode for lithium-ion batteries. In Journal of Power Sources, 2011, 196; pp. 2854–2857.

[Ze15]   Zeng, L. et al.: Metal hydride-based materials towards high performance negative electrodes for all-solid-state lithium-ion batteries. In Chemical communications (Cambridge, England), 2015, 51; pp. 9773–9776.

[ZFS15]   Zhou, C.; Fang, Z. Z.; Sun, P.: An experimental survey of additives for improving dehydrogenation properties of magnesium hydride. In Journal of Power Sources, 2015, 278; pp. 38–42.

[Zh15]   Zhang, Y. et al.: Synergistic effects of TiH2 and Pd on hydrogen desorption performances of MgH2. In International Journal of Hydrogen Energy, 2015, 40; pp. 16338–16346.

[Zl13]   Zlotea, C. et al.: Tunable synthesis of (Mg–Ni)-based hydrides nanoconfined in templated carbon studied by in situ synchrotron diffraction. In Nano Energy, 2013, 2; pp. 12–20.

[Zü03]   Züttel, A.: Materials for hydrogen storage. In Materialstoday, 2003.

10 APPENDIX

1. Thickness verification by FIB cross sections

During the experiments, it is important to identify the exact value of the thickness of the sputtered layers in order to be as accurate as possible, since this allows smaller errors for the calculation of the diffusion coefficient and the activation energy. For this reason, most samples have been cut by the FIB and imaging by the SEM allowed a confirmation of the thickness.

Multiple samples were cut in the same way and Figure 10-1 shows, as an example, two thicknesses. Sample a) was sputtered for 100 nm, but the actual value is shown to be at ≈ 135 nm instead. Sample b) was sputtered for 500 nm and the real value shown here is at about ≈ 450 nm. This shows that in each sputter run depending on the position of the substrate on the sample holder a small difference from the expected value is observed.

Figure 10-1: Examples of samples cross section for verification of the thickness.

2. Fitted model to resistance experiments

The model described in chapter 5.2.3 was used to fit all the experimental data obtained at different thicknesses and different temperatures. Since only the example of 300 nm was previously presented, here all thicknesses are given with the fitted model.

It is clear that the higher the thickness of the layer and the lower the temperature, the less compatible the model is to the experimental observation, which indicates that the model still miss some important feature, which could however not be resolved yet.
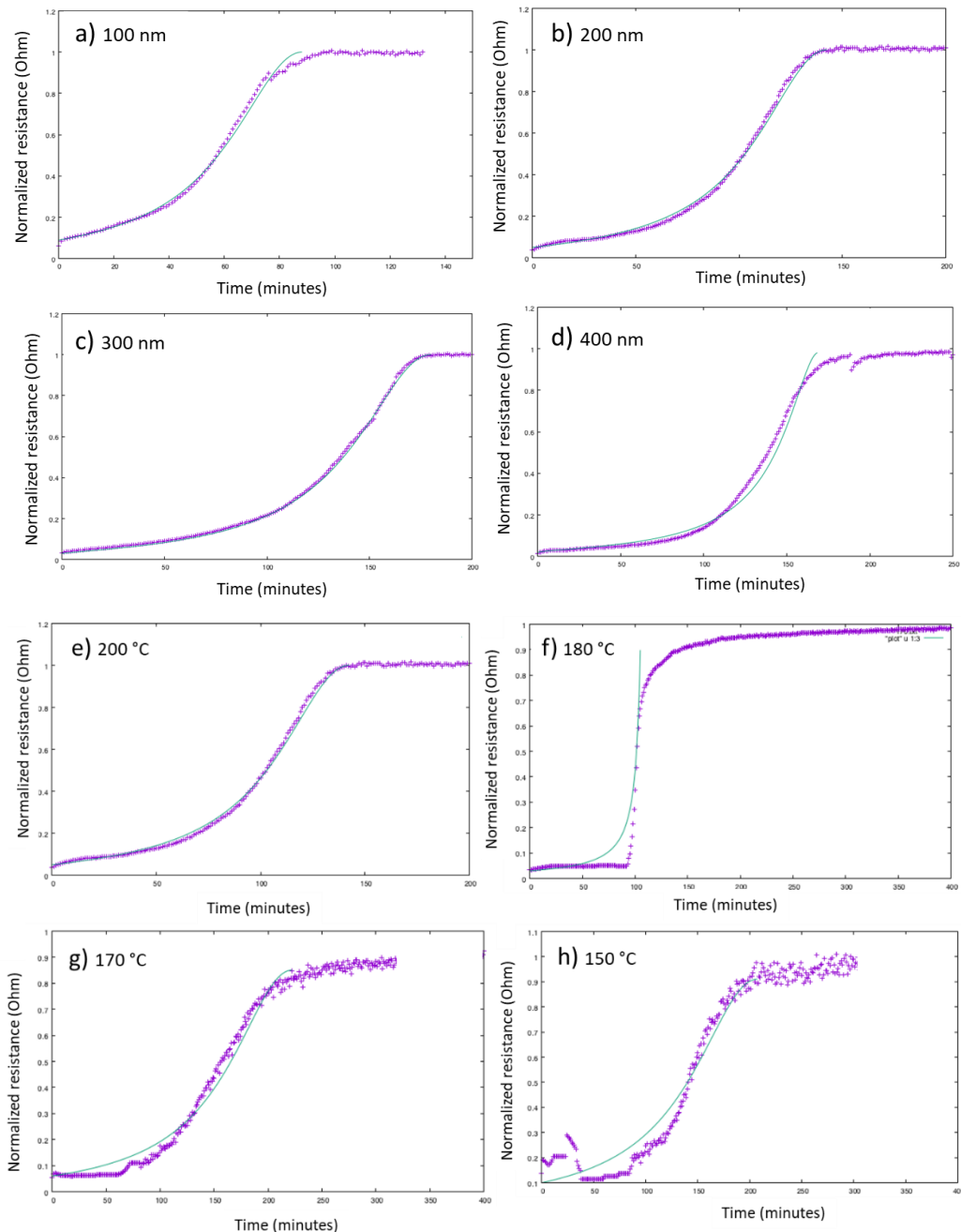
Figure 10-2: Graphs fitted to the model of resistance change upon hydrogen loading. a-d) shows the fit for small thicknesses e-h) demonstrates the fit at different temperatures.

List of figures

Liability agreement

I hereby certify that the dissertation entitled:

 "Hydrogen transport in thin films: Mg-MgH$_2$ and Ti-TiH$_2$"

is entirely my own work except where otherwise indicated. Passages and ideas from other sources have been clearly indicated.

Ich versichere, dass ich die vorliegende Arbeit mit dem Titel:

"Wasserstofftransport in dünnen Filmen: Mg-MgH$_2$ and Ti-TiH$_2$"

selbständig verfasst und keine anderen als die angegebenen Quellen und Hilfsmittel benutzt habe; aus fremden Quellen entnommene Passagen und Gedanken sind als solche kenntlich gemacht.

_____   _____
  Ort, Datum

                                                           Efi Hadjixenophontos

Acknowledgments

Curiosity is the driving force for a scientist. Today, science has become more than just mind work, but also a teamwork, social skills development and organization. I had the great opportunity to spend my last 4 years and develop myself and my scientific work with many wonderful people that supported me and guided me along the way.

I'm mostly grateful to Prof. Dr. Dr. Guido Schmitz for his exceptional and outstanding care throughout my time in the group. His scientific assistance and his constant encouragement with various problems has impressed me and motivated me throughout this work.

Of course, this work would not have been possible without the funding from the European Union's Seventh Framework Program funding, under grant agreement n°607040, Marie Curie ITN. My special thanks go to Klaus Taube and Sigrid Wulff for their great organization along this project.

Most obliged, I am to my office-mate Dr. Patrick Stender. His advice, guidance, support, moral and scientific, kept me positive in many difficult situations. Of course, without him, many of the tools used during this work would not have existed! Thank you Patrick, for all your support and guidance.

I'm very grateful to Prof. S. Orimo and Dr. T. Sato for their welcoming in Japan and their support in our experimental cooperation. It has been a great pleasure to spend time in their facilities and one of my most fruitful experiences for me abroad. Special thanks also goes to Dr. M. Hirscher from Max Planck institute, for his support along our publication, as well as Dr. Zoltán Bálogh-Michels at the Center of X-ray Analytics EMPA in Switzerland for his help with some in-situ XRD experiments.

Many thanks go to our technician Peter Engelhardt, who has been fast in helping me find what I need for my set-ups. His help was indispensable! My sincere gratitude goes to our secretary Jacqueline Dunn. Her patience with all the paper work, as well as her friendship has reinforced me during this journey. I'm very thankful, to my French friend Dr. Manuel Roussel, who had guided me scientifically at the beginning of this project and has been very much missed since he stepped out of the group. Appreciated is also the help of the newest member of our group Dr. Gábor Csiszár for his support since he arrived in the group. Most grateful I am to Robert Lawitzki and Yug Joshi. Their support and help in sharing responsibilities in the lab is very much appreciated.

I would like to thank my students, bachelors and masters who gave me the chance to supervise them for their thesis. An experience that gave me the chance to not only evolve as a scientist, but as a person as well. Among them most important, Lukas Michalek for all his work on Ti, as well as Andreas Weigel and Kun Zhang, who chose to spend a lot of their afternoons helping me in the lab. Their help has been essential to me.

List of publications

In the scope of this thesis (May 2014 – June 2018):

1	**"Imaging the hydrogenation of Mg thin films"** <u>Efi Hadjixenophontos</u>, Manuel Roussel, Toyoto Sato, Andreas Weigel, Patrick Stender, Shin-ichi Orimo, Guido Schmitz, International Journal Hydrogen Storage (2017) HE-D-16-03453
2	**"Ion transport and phase transformation in thin film intercalation electrodes"** Fabian Wunde, Susann Nowak, Juliane Mürter, <u>Efi Hadjixenophontos</u>, Frank Berkemeier, Guido Schmitz - International Journal of Materials Research (2017) doi.org/10.3139/146.111549
3	**"Hydrogen sorption kinetics in MgH$_2$ and TiH$_2$ thin films"**, <u>Efi Hadjixenophontos</u>, Lukas Michalek, Andreas Weigel, Guido Schmitz – Defect and Diffusion, ISSN: 1662-9507, Vol. 383, pp 127-132
4	**"Grain boundary transport in sputter-deposited nanometric thin films of lithium manganese oxide",** Juliane Mürter, Susann Nowak, <u>Efi Hadjixenophontos</u>, YugJoshi, Guido Schmitz - Nano Energy 43 (2018) 340–350
5	**"Influence of the surface oxide layer on hydrogen sorption kinetics in titanium thin films"** <u>Efi Hadjixenophontos</u>, Lukas Michalek, Manuel Roussel, Michael Hirscher Guiro Schmitz – Applied Surface Science 441 (2018) 324–330
6	**"Modulation of the Optical Properties of Lithium Manganese Oxide via Li-Ion De/Intercalation"** Y. Joshi, <u>E. Hadjixenophontos</u>, S. Nowak, R. Lawitzki, Prof. G. Schmitz – Adv. Optical Mater. 2018, 1701362
7	**"Thin films as model system for understanding the electrochemical reaction mechanisms in conversion reaction of MgH$_2$ with lithium"** N. Berti, <u>E. Hadjixenophontos</u>, F. Cuevas, J. Zhang, A. Lacoste, P. Dubot, G. Schmitz, M. Latroche - submitted to Journal of Power Sources: POWER-D-18-02245

Curriculum vitae

Researcher in Materials Science

EFI HADJIXENOPHONTOS

ehadjixenophontos@gmail.com

Tel: 00 49 1575 4071 865
Nationality: CYPRIOT
Residence: Stuttgart, Germany
Drivers license

LANGUAGES
Greek: native
English: fluent
French: fluent
German: basic
Spanish: intermediate

AWARDS (6) from conferences

- **Poster awards: (5)**
1. Diffusion in Materials (DIMAT) 2017 Haifa, **Israel**
2. Deutsche Physikalische Gesellschaft e.V. (DPG), 2017 Dresden, **Germany**
3. Hydrides as Energy Materials (HyDEM) 2016 Aarhus, **Denmark**
4. International Symposium Hydrogen & Energy (ISH&E) 2016 Sendai, **Japan** 5. German-Japanese International Symposium on Nanostructures (OZ-2015) Kyoto, **Japan**

- **Presentation awards: (1)**
6. European Materials Research Society E-MRS Fall, 2017 Warsaw, **Poland**

INTERESTS
1. Scuba diver (NAUI)
2. Photography
3. Hiking

Lived in...
1. Stuttgart, GERMANY *(today...since 2014)*
2. Bordeaux, FRANCE *(1,5 months)*
3. Sendai, JAPAN *(1,5 months)*
4. Cordoba, SPAIN *(6 months)*
5. Montreal, CANADA *(6 months)*
6. Amiens, FRANCE *(6 months)*
7. Warsaw, POLAND *(6 months)*
8. Toulouse, FRANCE *(6 months + 1 year)*
9. Montpellier, FRANCE *(4 years)*
10. Nicosia, CYPRUS *(until high school)*

Personal statement

Enthusiastic materials scientist, with experience in materials for hydrogen and electrochemical (batteries) energy storage. Worked intensively on thin films (PVD) and diffusion processes. Skilled in electron microscopy techniques and capable in electrochemical characterization methods. Good management skills that brought out successful work during supervision of students for their thesis. Involved in teaching and training of students in lab equipment. Great communication skills that created a wide network of collaborations over the international conferences and projects attended. Excited about working in an international environment.

EDUCATION

2018 - **PhD in Materials Science,** University of Stuttgart – *Marie Curie ITN ECOSTORE* (N° 607040) http://ecostore.hzg.de/
Hydrogen transport in thin films: Mg-MgH$_2$ and Ti-TiH$_2$-TiO$_2$ systems
<u>workshops</u>: on various scientific techniques and personal skills development

2012 – **M.Sc. Materials for Energy Storage and Conversion** (MESC), UPJV – Amiens, France, Paul Sabatier - Toulouse, France, WUT - Warsaw, Poland, University of Cordoba - Cordoba, Spain – *ERASMUS MUNDUS joined degree*

2010 – **B.Sc. Physical Chemistry,** University of Montpellier II, France

2007 – **Certificate of French Language,** University of Montpellier III, France

2006 – **Abitur – High school diploma at Pancyprian Gymnasium,** Cyprus equivalent to 4 A-Levels specializing in Science

WORK EXPERIENCE

2012 – 2013 (10 months) CIRIMAT Research Center/University Paul Sabatier
Lab Assistant – <u>Supervisors</u>: Emmanuel Flahaut, Patrice Simon
Nanostructured carbon and ionogels for solid state electrochemical capacitors

2012 (6 months) University of Quebec a Montreal
M.Sc. Thesis – <u>Supervisors</u>: Daniel Belanger, Thierry Brousse
Hybrid electrochemical capacitors using ionic liquid and C-modified electrodes

2008 (3 months) University of Cyprus, Department of Chemistry
Lab Assistant – <u>Supervisors</u>: Savvas Savva
Carbonyl – coupling reactions using titanium

2005 (3 months) ARTOS Association – Nicosia Cyprus
Teaching Assistant - <u>Supervisors</u>: Nikos Ioannou
RoboLAB computer programming for children (6-14 years old)

LABORATORY TECHNIQUES

- Electron microscopy
  TEM (Philips CM200)
  FIB/SEM dual beam (FEI-SCIOS)
- Thin film deposition *(PVD)*
- Atom Probe Tomography *(APT)*
- Magnetron sputtering
- Ion beam sputtering
- X-ray Diffraction *XRD (Siemens 5000, D8Linse)*
- Electrochemical characterization for batteries
- BET, Raman,
- DSC, TGA, SPS, NMR...

TEACHING EXPERIENCE

1. Supervising students for their thesis: (2015 – 2018)
- *15 bachelor students*
  (from Germany and China)
- *9 master students*
  (from Germany, Turkey and Korea)

2. Exercise classes (master's level) *Alloy Design* (2017)

3. Transmission Electron Microscopy (TEM) laboratory classes (2014 – 2018)
- Diffraction/Direct mode of Al, Sn (polycrystalline) and Si (monocrystalline)
- Identification of unknown crystalline samples

4. French teacher: Levels DELF, A1, A2, B1, GCE (2010-2014)

General topics of research supervised
(24 students thesis):
- Solid state batteries with LIPON (thin film) and $LiBH_4$ (powder) electrolytes in Li-ion batteries
- NMC, MgH_2, Ti_2S and TiH_2 electrodes in both liquid and solid state electrolytes
- Hydrogenation of Ti Nanostructures
- Deposition of $LiBH_4$ and $Mg(BH_4)_2$ thin films as solid state electrolytes
- Atomic transport along SiO_2-Si/Al interfaces, artificial triple junctions
- Cu/Ge and Ge/Cu formation of intermetallics
- Nanoanalysis of TiH_2 by Atom Probe Tomography

COLLABORATIONS

- Dr. Fermin Cuevas – ICMPE CNRS, Paris, France **(2015)**
  electrochemical investigations in MgH_2 as a battery electrode

- Dr. Sato, Orimo Laboratory – Institute for Materials Research, Tohoku University, Sendai, Japan **(2015)**
  on insitu-XRD in Mg during hydrogen loading

- Dr. Christian JORDY – SAFT Batteries, Bordeaux, France **(2016)**
  electrochemical investigations in MgH_2 thin films

- Dr. Elham Sharifikolouei – MPI for Medical Research, Prof. Dr. J.Spatz group, Stuttgart, Germany **(2017)**
  on Dual phase nanocrystalline-amorphous stainless FIB/TEM on steel fibers

- Dr. Ivan Saldan – Ivan Franko National University of Lviv, Ukraine **(2017-2018)**
  DAAD Project on experimental synthesize of nanoparticles and thin films of $MgBH_4$

- Dr. Igor Vladymyrskyi – National Technical University of Ukraine **(2018)**
  FIB/TEM on Phase transformation of Pt/Tb-Ag-Mn/Fe layers

- Tobias Joachim Menold – Laser Material Processing (CR/APJ2) BOSCH, Stuttgart, Germany **(2018)**
  FIB/TEM on monocrystalline Si for dislocations and stacking folds

CONFERENCES (13) – Talks (8) and poster (9) presentations

- Deutsche Physikalische Gesellschaft e.V. (DPG), Germany (**2016** Regensburg, **2017** Dresden, **2018** Berlin)
- International Symposium Hydrogen and Energy (ISH&E), Sendai, Japan (**2016**), ISH&E Lausanne, Switzerland (**2018**) – *invited speaker*
- European Materials Research Society (E-MRS Fall), Warsaw, Poland (**2015, 2017**)
- Diffusion in Materials (DIMAT), Haifa, Israel (**2017**)

- International Symposium on Metal-Hydrogen Systems (MH**2014**), Manchester, UK and (MH**2016**), Interlaken, Switzerland
- Hydrides as Energy Materials (HyDEM), Denmark (**2016**)
- German-Japanese International Symposium on Nanostructures OZ-**2015**, Kyoto, Japan
- Atom Probe Tomography and microscopy (APT&M) **2014** Stuttgart, Germany *(organization member)*

SCHOLARSHIPS (4)	WORKSHOPS AND ONLINE CLASSES (attended)		SOFTWARE
1. CROUS (B.Sc.) Scholarship for Academic excellence, over 4 years ≈ *14,000euros* 2. Erasmus Mundus Master (M.Sc.), over 2 years – *10,000euros* 3. Marie curie PhD Fellowship ITN (PhD), over 3 years – *114,000euros* 4. COST Grand summer school (during MH2014 conference), over 1 week – *940euros*	• Grant proposal writing (2 days) • Management and development (1 week) • Public speech (3 days)	• Nanotechnology (2 days) • Energy and Environment (1 week)	• Origin • EC-Lab • Avizo – FEI • Code ++Blocks (basic) • Microsoft office

List of publications (7) available upon request